ADVANCED IMAGING VIA MULTIPLEXED SENSING AND COMPRESSIVE SENSING

BY

XIANBIAO SHU

DISSERTATION

Submitted in partial fulfillment of the requirements
for the degree of Doctor of Philosophy in Electrical and Computer Engineering
in the Graduate College of the
University of Illinois at Urbana-Champaign, 2013

Urbana, Illinois

Doctoral Committee:

Professor Narendra Ahuja, Chair
Professor Mark Allan Hasegawa-Johnson
Professor Thomas S. Huang
Dr. Fatih M. Porikli, Mitsubishi Electric Research Lab

ABSTRACT

This dissertation works on advanced imaging systems using multiplexed sensing and compressive sensing (CS). Conventional cameras (e.g., pin-hole and lens cameras) follow the one-object-point-to-one-image-point or one-to-one (OTO) mapping model. Multipled sensing and compressive sensing attempt to improve conventional OTO cameras by exploring other object-to-image mapping models, such as one-to-multiple (OTM) divergent mapping, multiple-to-one (MTO) convergent mapping and multiple-to-multiple (MTM) random mapping, and respectively achieve two different advanced imaging functions. On one hand, multiplexed sensing attempts to acquire multi-modality information from the outside scene by multi-channel sensing and fuses a more informative image. On the other hand, compressive sensing, also called compressive sampling, aims at acquiring a signal/image at a lower sampling rate (below the Nyquist rate) by exploiting (1) the MTM random sampling and (2) the prior knowledge that a signal/image is sparse or correlated in some domain.

The first design is a multiplexed imaging system that accesses and manipulates the lens aperture for many computational imaging applications. Multiplexed imaging often involves manipulating the incoming light beam on the aperture, which is located inside the lens housing and thus is challenging to access or modulate. In this system, a novel approach is proposed to provide an external aperture that enables dynamic control of its transmission, position and orientation. Specifically, a rear-attached relay system (lens) is mounted behind the imaging lens to reposition the aperture plane outside the imaging lens. The physical implementation of the multiplexed imaging system is presented to show (1) the effectiveness of providing access to the aperture and (2) the advantages of aperture manipulation in computational imaging applications.

The second design is a hybrid compressive sensing camera for image ac-

quisition. First, this hybrid compressive sensing camera further reduces the sampling rate of compressive sensing by combining the traditional MTM random sampling with MTO low-resolution sampling. In addition, we propose a new L1-norm based total-variation measure TVL1, which enforces the sparsity and the directional continuity in the partial gradient domain. Theoretical and experimental results show that this new TVL1 achieves higher recovery accuracy than the previous TV measure TVL1L2 in decoding images from compressive measurements.

The third design is a three-dimensional compressive sensing (3DCS) camera for video acquisition. Despite the remarkable progress in the compressive sensing theory, little headway has been made in the compressive imaging (CI) camera and the required sampling rate for acquiring an image or video is still high. We propose a three-dimensional compressive sensing (3DCS) approach, which decodes a video from incomplete random samples by exploiting its 3D piecewise smoothness and temporal low-rank property. Experimental results show that 3DCS can reduce the required sampling rate for video acquisition to a practical level (i.e., 10%). In addition, an efficient decoding algorithm is developed for this 3DCS with guaranteed convergence. Finally, a promising physical implementation of the 3DCS camera using circulant sampling (or random convolution) is presented and a new random lens is presented to simplify the traditional random convolution implementation, i.e., four-dimensional correlator in Fourier optics. This random lens has much higher light-gathering power and higher imaging quality than other simple implementations, such as coded aperture, random pinhole array and random mirror array.

In addition to sparsity and total variation, low-rankness is another new and encouraging measure in compressive sensing. However, robust low-rank recovery from compressive measurements is a time-consuming process and even its state-of-the-art (robust principal component analysis or RPCA) has a cubic complexity. The fourth design is an efficient low-rank recovery approach, called robust orthonormal subspace learning (ROSL). Compared with RPCA using nuclear norm, ROSL presents a novel rank measure that imposes the group sparsity under orthonormal subspace, which enables it to recover a low-rank matrix by fast sparse coding. Theoretical bounds are given to prove that minimizing this rank measure has the same global minimum as the nuclear norm minimization. In addition, an efficient algorithm

(alternating direction method and block coordinate descent) is developed for ROSL and a random sampling algorithm is introduced to further accelerate ROSL such that ROSL+ has linear complexity of the matrix size. Extensive evaluations demonstrate that ROSL and ROSL+ achieve the state-of-art efficiency in low-rank recovery without compromising the accuracy.

The fifth design is a non-local compressive sensing (NLCS) camera for image acquisition. While 3DCS achieves a low required sampling rate for video acquisition, image CS still requires a high sampling rate. Motivated by the non-local mean approaches in image restoration, a non-local compressive sensing (NLCS) recovery method is proposed, which further reduces the sampling rate by exploiting the non-local patch correlation and the local piecewise smoothness in natural images. Two non-local sparsity measures, i.e., non-local wavelet sparsity and non-local joint sparsity, are proposed to obtain patch correlation in NLCS. In addition, an efficient iterative algorithm is developed to solve the NLCS recovery problem, which is shown to have stable convergence behavior in experiments. The experimental results show that our NLCS significantly improves the state-of-the-art image CS and that non-local joint sparsity is better than non-local wavelet sparsity in terms of recovery accuracy.

To my parents and my wife, for their love and support

ACKNOWLEDGMENTS

First, I would like to express my sincere gratitude to my advisor Prof. Narendra Ahuja for his continuous support and inspirational guidance during my Ph.D. study. Never will I forget the encouraging words he spoke to me at the beginning of my Ph.D. study, e.g., "Good ideas take time. Keep thinking about it and some day it will come natually." During the last five and one-half years, I have been inspired by his immense knowledge and vision, his rigorous and curious attitude to research, his dedication and commitment to his work and his genial and humble personality. What I have learned from Prof. Narendra Ahuja has inspired me to complete this dissertation and will also benefit me in my future life.

I also would like to express my thanks to Prof. Thomas S. Huang and Prof. Mark Hasegawa-Johnson, for their support and suggestions in my qualifying, preliminary and final exams. I really admire their rigorous logical thinking and insightful comments. I feel very lucky to work with Dr. Fatih M. Porikli at Mitsubishi Electric Research Lab. From him, I have learned not only precious reseach insights and skill, but also his diligent and passionate working style. I am also thankful to Prof. Yi Ma and Prof. Yoram Bresler for their valuable discussions, which helped me understand my research area better.

I owe my sincere gratitude to other collaborators and those who provided help to my dissertation, including Chunyu Gao, Qingxiong Yang, Jianchao Yang, Zihan Zhou, Prof. Wotao Yin from Rice University and Prof. Junfeng Yang from Nanjing University. In addition, I also would like to thank all my colleagues at Computer Vision and Robotics Lab (CVRL) in Beckman Institute, including John Hart, Bernard Ghanem, Sanketh Shetty, Emre Akbas, Esther Resendiz, Myra Nam, Hsien Ting Cheng, Avinash Kumar, Abhishek Singh and Jia-bin Huang. I learned a lot from the countless discussions with them and enjoyed the wonderful time at CVRL.

Last but not least, I would like to give special thanks to my wife, Xi Chen, for her continuous love and support during my Ph.D. study. This dissertation would not be possible without her companionship and support. Finally, I want to express my special gratitude and thanks to my parents for their unconditional support and care throughout my life. Life would not be so beautiful without their love.

TABLE OF CONTENTS

CHAPTER 1

MULTIPLEXED IMAGING BY APERTURE ACCESS AND MANIPULATION

1.1 Introduction

1.1.1 Multiplexed Imaging by Aperture Manipulation

Many multiplexed imaging applications require capabilities beyond those offered by normal cameras, e.g., larger field-of-view (FOV), resolution, dynamic range, depth of field (DOF) or frame rate. A variety of methods proposed to achieve this need involve accessing and controlling the lens aperture (Figure 1.1(b)). Manipulating the shape, size, structure, position and orientation of the aperture makes it possible to modify the viewing axis, control the amount of incoming light, and encode the depth information. For instance, coded aperture imaging mounts a mirror array [1] or coding patterns [2, 3, 4] at the aperture to obtain one or multiple images that encode the scene depth. A mirror array is employed to partition the aperture into several sub-apertures, through which multiple images of the same scene are captured for high speed imaging [5] and high dynamic range (HDR) imaging [6]. Light field photography varies the aperture position by filters or lens arrays to acquire images from different viewpoints [7, 8, 2, 9]. Omni-directional imaging [10, 11] controls the orientation of the aperture to capture panoramic images using a planar or convex mirror. Lensless imaging [12] modulates the direction and amount of the incoming light by employing a set of parallel transmittance patterns at the aperture. Accordingly, multimodality information of the outside world can be acquired by talking images at different statuses of aperture. All these multiplexed imaging methods involve the interception and processing of the incoming light, e.g., by placing filters, beam splitters or mirror arrays in the aperture plane.

Although some the advanced imaging functions above, e.g., HDR imaging,

panoramic imaging can be realized by using other methods, the aperture-manipulating method has several unique advantages. For instance, compared to conventional HDR imaging using a transmission-variant mask [13, 14, 15] or a beam-splitter, the aperture-splitting method [6] has two advantages: (1) it makes the most use of incoming light, almost without blocking any, and (2) the percentages of the incoming light received by different cameras can be flexibly controlled. Aperture manipulation can yield a panoramic image by rotating a camera about its optical center (entrance aperture) [16] in a static scene, or by pointing multiple cameras at different visual directions from a common optical center [10] in the dynamic scene.

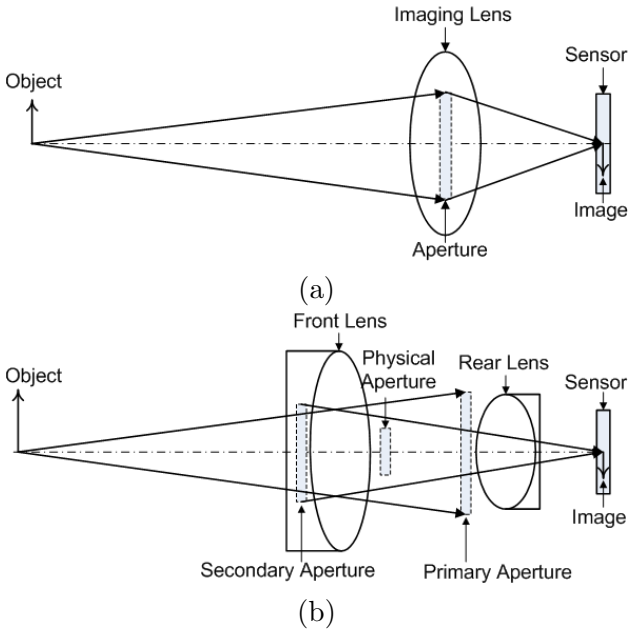

Figure 1.1: (a) A conventional imaging lens showing the (b) physical aperture, primary aperture, and secondary aperture.

It is not easy to access the aperture of a conventional imaging lens, since it is located within the lens housing. A typical imaging lens consists of a front lens group, a rear lens group and a physical aperture, called aperture stop or simply aperture (Figure 1.1(b)). The virtual image of the physical aperture in the front lens is defined as the primary aperture (or entrance pupil) and its virtual image in the rear lens is defined as the secondary aperture. These three apertures are optically equivalent. The aperture determines which rays can pass through the lens to reach the sensor, and plays a central role

in controlling image brightness, image quality and visual direction. Since the physical aperture is typically located inside the lens and the other two apertures are virtual, none of which is easily accessible, opening or closing the physical aperture is the only external aperture control available

1.1.2 Optical Relay System and Afocal System

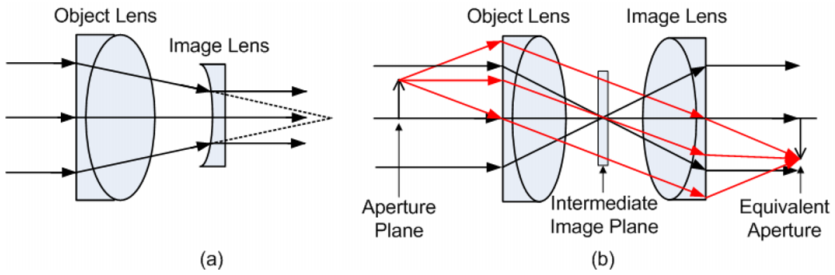

Figure 1.2: (a) A Galilean afocal system consists of a positive object lens and a negative image lens. (b) A Keplerian afocal system (or mounted achromatic pair) employs two positive lenses as the object and image lenses. In both systems, the back focal points of the object lens and the image lens are located at the same position.

Before continuing, a brief review of the optical relay system is provided. An optical relay system is a group of lenses that relocates an image or aperture from one plane to another. The most widely used realization of a relay lens is a pair of mounted achromatic lenses or its optimized versions. By placing an aperture at the focus point of its frontal lens (Figure 1.2(b)), the achromatic pair forms an equivalent aperture at the focus point of its rear lens. Ordinarily, a relay system is used to invert an image or increase the distance between the primary aperture and the image plane [17]. In this chapter, we employ the relay system to reposition the aperture out of the imaging lens. A basic design requirement of the relay lens is that it does not alter the optical parameters (e.g. focus distance and image size).

Afocal optics is a special relay system with focal points located at infinity [17]. A pencil of parallel rays passing through an afocal system remains parallel. There are two kinds of afocal systems, Galilean and Keplerian, which are widely used in telescopes. As shown in Figures 1.2(a) and (b), both afocal systems can preserve the parallelism of incident parallel rays as they

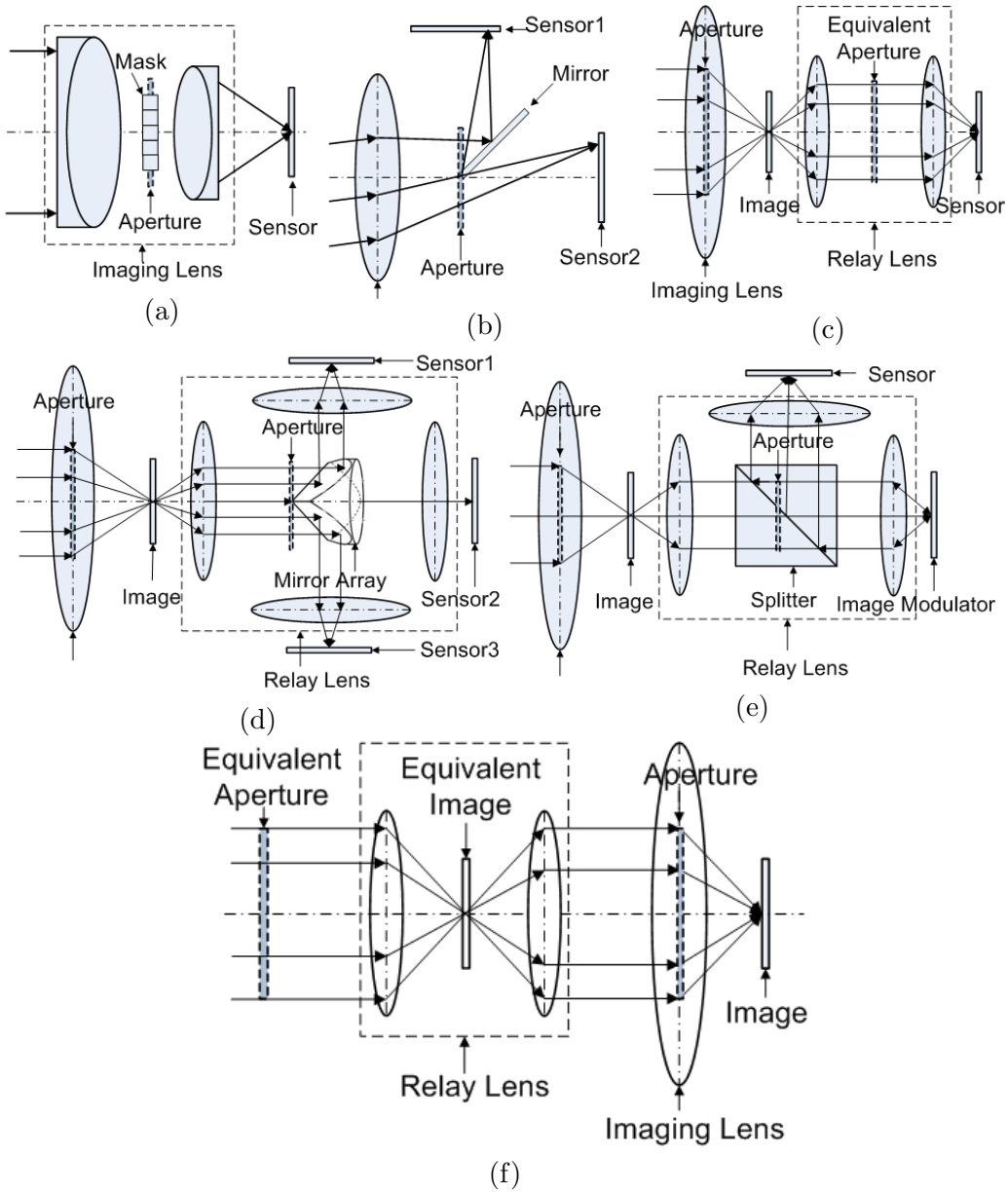

Figure 1.3: (a) Modified lens for placing a mask on the aperture. (b) Custom imaging lens with its aperture outside lens housing. (c) Rear-attached small-aperture relay lens and two of its applications: (d) aperture splitting by mounting a mirror array on the equivalent aperture plane and (e) image modulation by placing a modulator on the intermediate image plane. (f) Fore-attached relay lens.

pass through them. The major difference between these two systems is that the Keplerian system is capable of repositioning the aperture plane from one side to another, making the aperture externally accessible (Figure 1.2(b)). Besides, the Keplerian system forms an intermediate image plane between its two lenses, which is useful for image modulation.

1.1.3 Previous Methods of Accessing Aperture

Conventionally, accessing the aperture of an imaging lens requires either machining the lens housing, customizing the lens with an external aperture, or combining the lens with some relay system.

1. **Modified or Customized Lenses**. Veeraraghavan et al. [2] and Liang et al. [3] cut the lens barrel to place a coded mask at the aperture located inside the imaging lens (Figure 1.3(a)). However, this method is impractical and infeasible when inserting a large-size aperture filter. Harvey et al. [5] and Aggarwal et al. [6] employ custom imaging lenses (Figure 1.3(b)) with the aperture outside the lens housing, but custom lenses are very expensive.

2. **Previous CIS Using Rear-Attached Separate Relay Systems (RSRS).** As shown in Figure 1.3(c), RSRS repositions the aperture from inside the imaging lens to inside the relay system [18, 1]. This compounding imaging system with RSRS is named as CIS_RSRS. CIS_RSRS is widely applied to aperture manipulation (Figure 1.3(d)) and image modulation (Figure 1.3(e)). For aperture manipulation, the aperture splitter is placed behind one achromatic lens to partition the parallel rays into multiple beams, and correspondingly multiple achromatic lenses are required for forming images on sensors. CIS_RSRS has two disadvantages, both of which accrue from the fact that the accessible aperture stands inside the relay system. First, mounting and calibrating these achromatic lenses and the imaging lens is quite complicated [1]. Second, a splitter needs to be mounted inside the relay lens, which restricts the choice of the relay system to an achromatic pair, which is simple but provides low-quality images.

3. **Previous CIS Using Fore-Attached Relay Systems (FRS).** As shown in Figure 1.3(f), a novel compound imaging system (named as CIS_FRS) is proposed to provide the external access to image and aperture planes by mounting an afocal relay system in front of the imaging lens [10]. This method has two shortcomings. First, this fore-relocated aperture provided by CIS_FRS is only adapted to multiplexed imaging in the object space [10]. Second, by providing an intermediate image plane inside the relay system, CIS_FRS is not suitable for image modulation, unless it uses low-quality achromatic pairs.

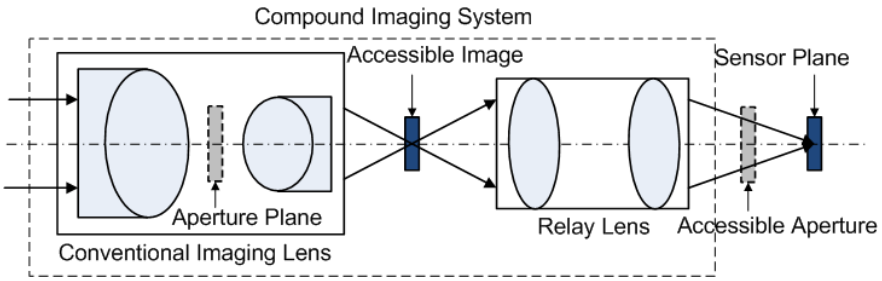

Figure 1.4: Our compound imaging systems with rear-attached joint relay system (CIS_RJRS). It provides both external apertures and accessible image planes for multiplexed imaging.

Among those previous methods, only CIS_FRS provides an external access to the aperture of an off-the-shelf imaging lens. This chapter proposes another CIS that provides external access to both the aperture and image planes without any structural modification of the lens. As shown in Figure 1.4, as opposed to CIS_FRS, our CIS_RJRS repositions the aperture plane from inside to behind the imaging lens, where the aperture can be manipulated for a wider range of multiplexed imaging applications [5, 6, 3, 1, 4]. We outline the similarities and differences between these two CIS—the previous CIS_FRS and our CIS_RJRS as follows.

1. **Optical Structure.** Both CIS_FRS and our CIS_RJRS consist of an imaging lens and a relay lens. However, their requirements on the relay system are different. The former requires the aperture size of the fore-attached relay system to be proportional to the field-of-view (FOV) of the imaging lens, while the latter requires the aperture size of the

rear-attached relay lens to be proportional to the aperture the imaging lens.

2. **Aperture Access and Manipulation.** Both CIS methods can provide external access to the aperture of the imaging lens. CIS_RJRS is advantageous over CIS_FRS in multiplex imaging applications involving aperture manipulation in the image space. By repositioning the aperture behind the imaging lens, CIS_RJRS can (1) protect the aperture-modulating pattern from extraneous environmental light and (2) be easily used to build the compact single-lens-multi-sensor multiplexed imaging system [5, 6, 3, 1].

3. **Image Access and Manipulation.** Both CIS methods form an intermediate image which is optically conjugate to the image in the sensor plane. These intermediate image planes can be controlled for multiplexed imaging applications, e.g., HDR imaging [13, 14, 15, 18]. However, to realize this HDR imaging, CIS_FRS must sacrifice the imaging quality by using the achromatic system as its relay system. By relocating the image and aperture planes outside the relay lens, CIS_RJRS allows the employment of the joint-optimized relay lens and thus has a higher imaging quality.

Although many advanced imaging functions are facilitated by providing external access to both aperture and image planes in our CIS_RJRS, our major contribution is the external accessible apertures, for the way the intermediate image planes are formed is similar to previous work [13, 14, 15, 18]. Thus, we mainly focus on aperture access and manipulation in this chapter. Specifically, we discuss controlling the position, area, orientation or transmissivity of the aperture by inserting a mirror or a coded mask. We show the external aperture of our CIS_RSRS by building a physical prototype and present one of its multiplexed imaging application, i.e., aperture splitting for high dynamic range (HDR) imaging.

This chapter is organized as follows. Section 1.2 presents the design of the rear-attached joint relay system in CIS_RJRS, Section 1.3 describes multiplexed imaging applications of CIS_RJRS, Section 1.4 presents simulation and experimental results, and Section 1.5 presents concluding remarks.

1.2 Proposed Rear-Attached Joint Relay System

This section presents the design of rear-attached joint relay system used to build our CIS_RJRS. By attaching the relay system behind the imaging lens, CIS_RJRS provides an external aperture that can be accessed and manipulated for many multiplexed imaging applications.

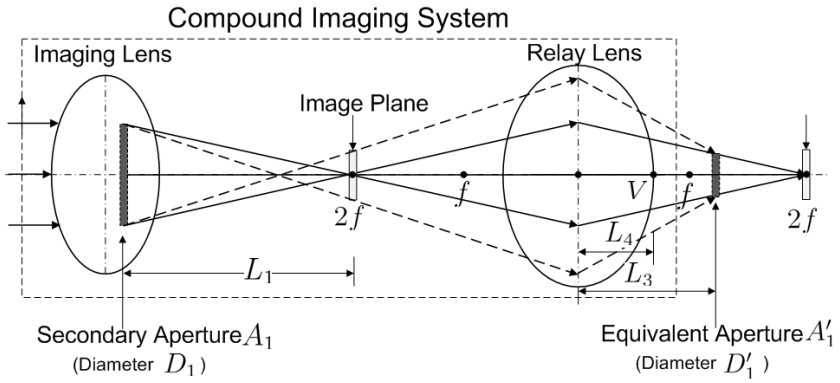

Figure 1.5: The optical layout of our compound imaging system CIS_RJRS. By mounting a relay lens behind the imaging lens with the image plane at the $2f$ point of the relay lens, CIS_RJRS provides the equivalent aperture D_1' behind the imaging and relay lenses.

As shown in the Figure 1.5, the rear-attached relay system is mounted with its frontal $2f$ plane at the image plane of the imaging lens. Thus, it repositions the image plane to the sensor plane, which is located at its rear $2f$ plane. In addition, our relay system relocates aperture A_1 at the equivalent aperture A_1' between the relay lens and the sensor.

The aim of this proposed relay system is to gain external access to aperture A_1 behind the imaging lens and relay lens (Figure 1.5) without altering the imaging properties. To achieve this goal, our design of this relay system must meet three major conditions: (1) reform an image at the sensor plane with the unit magnification ratio, (2) provide an equivalent aperture A_1' (an optical conjugate to aperture A_1) behind the relay lens, and (3) allow optimizing the relay lens, which is independent of aperture manipulation.

1.2.1 Equivalent Image with Unit Magnification

The preferred relay system in our CIS_RJRS is symmetric with unit magnification. The imaging lens and the relay system are concatenated such that the image plane of the imaging lens coincides with the frontal $2f$ plane of the relay system. In this way, our relay system forms an equivalent image on the sensor with the unit magnification ratio, without modifying the imaging properties of the host camera. However, in practice, it is difficult to control the distance between the relay system and the imaging lens precisely so as to achieve unit magnification. So, we will study how positioning affects the position and size of the equivalent image. For instance, if the image plane is displaced by a short distance d from the $2f$ focal plane, then the equivalent image is shifted away from the rear $2f$ focal plane by a distance of M^2d, where M is the transverse magnification and $M = 1$ when the relay system is symmetric.

1.2.2 Effective Aperture behind Relay System

To relocate an effective aperture A_1' behind the relay system, the design of our relay system involves two requirements: forming an image A_1' of A_1 behind the relay lens and making sure that any imaging beam passing through A_1 will not be blocked by the relay system.

First, to form an image A_1' of A_1 behind the relay lens, we need to determine the focal length f and the structural parameter L_4 for the relay system, where L_4 denotes the distance between the rear vertex V and the center of the relay lens. Suppose that the distance between A_1 and the image plane is L_1 and the distance between A_1' and the optical center of the relay lens is L_3. According to the object-to-image relationship [17], i.e., $\frac{1}{f} = \frac{1}{L_1+2f} + \frac{1}{L_3}$, the image distance L_3 is determined as follows:

$$L_3 = f + \frac{f^2}{f + L_1}. \tag{1.1}$$

Following are two designs of the relay lens that can provide rear accessible apertures.

1. **Design 1: the rear focus point is selected to be outside the relay lens ($L_4 \leq f$).** From Eq. (1.1), we have $L_3 > f \geq L_4$, and

thus A_1' is formed behind the relay lens. This kind of relay lens can be employed for gaining external access to the aperture of any imaging lens.

2. **Design 2: the rear focus point is selected to be inside the relay lens ($L_4 > f$).** In this case, the image distance L_3 of A_1' must be larger than L_4. According to Eq. (1.1), given that an imaging lens with L_1, the focal lens and structural parameters of the relay lens must satisfy the condition, i.e., $\frac{f^2}{L_4 - f} - f > L1$.

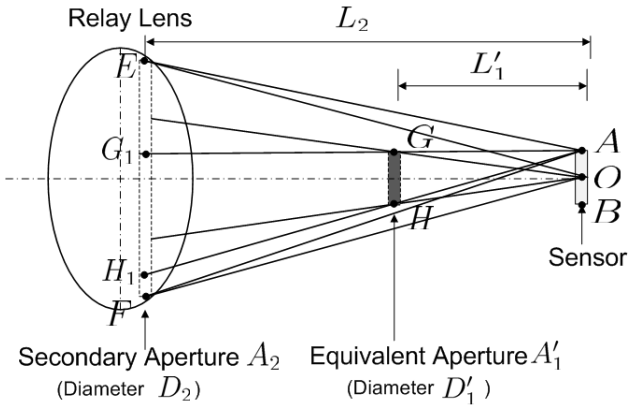

Figure 1.6: Relationship between the image lens aperture A_1 (or equivalently A_1') and the relay lens aperture A_2.

Second, we must ensure that any imaging beam passing through A_1 is not blocked by the rear-attached relay lens. In the compound imaging system, there are always two apertures—aperture A_1 (relative aperture: D_1/L_1) in the imaging lens and aperture A_2 (relative aperture: D_2/L_2), the secondary aperture of relay lens. The one with smaller relative aperture controls the imaging beam and hence is called the effective aperture. Since it is not desirable to relocate the effective aperture inside the relay lens, similar to the previous method (Figure 1.3(c)), we design our relay system with a larger relative aperture than that of the imaging lens. In this case, our proposed relay system repositions the effective aperture A_1 to A_1' outside the relay lens. As shown in Figure 1.6, the equivalent aperture A_1' is conjugate to the aperture A_1, and thus their relative apertures should be equivalent ($D_1'/L_1' = D_1/L_1$). In the following, we present two conditions on the relative aperture $\frac{D_2}{L_2}$ of the relay lens.

1. **The condition for the aperture to be effective.** For the aperture A_1 and its image A_1' to be effective, any imaging beam originating from point O within the cone angle $\angle GOH$ must be allowed to pass through the aperture A_2. Thus, it is required that $D_2/L_2 \geq D_1'/L_1' = D_1/L_1$.

2. **The condition for avoiding vignetting.** To suppress optical vignetting, every point on the sensor should receive the same amount of irradiance, given the radiances of outside scene points are the same. Since A_1' (diameter: GH) is the effective aperture, any imaging beam passing through A_1' is able to go through A_2 without being blocked. To satisfy this condition, specific ray (AHH_1) should go though A_2. We hence derive the relationship of A_1 and A_2, which is the prerequisite to avoid any vignetting effect.

$$\frac{D_2}{L_2} \geq \frac{D_1}{L_1} + |AB| \cdot \frac{L_2 - L_1'}{L_1' \cdot L_2}. \tag{1.2}$$

1.2.3 Imaging Quality

It is required that inserting a relay system not degrade the quality of the image formed by the imaging lens. In general, there is no ideal lens (point-to-point mapping). By attaching a relay lens, the imaging quality of the host camera will decrease to some extent. To the best possible quality, we need to improve the point spread function of the relay lens, which depends on the material, shape, and positions of individual lenses constituting the relay lens. The previous relay systems in Figure 1.3(c)(f) respectively require an image modulator and an aperture modulator to be mounted inside the relay lens, which limits the selection of relay lens to simple achromatic pairs and thus decreases the imaging quality. By repositioning the accessible aperture outside the relay lens, our CIS_RJRS enables us to optimize the relay lens and manipulate the aperture simultaneously. Thus, by inserting a high-quality joint relay lens, the image quality of the imaging lens will almost keep unchanged (Figure 1.7(a)).

Using the optical design software ZMAX, we simulate the imaging quality of achromatic pairs and the joint optimized relay lens in our CIS_RJRS, both of which are available from Edmund Optics. Modulation transfer function (MTF) is the most widely used method of describing lens performance. It

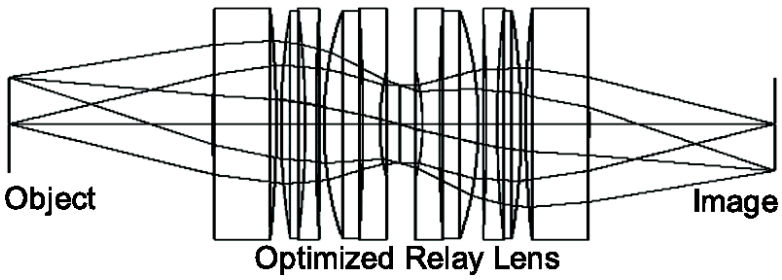

(a)

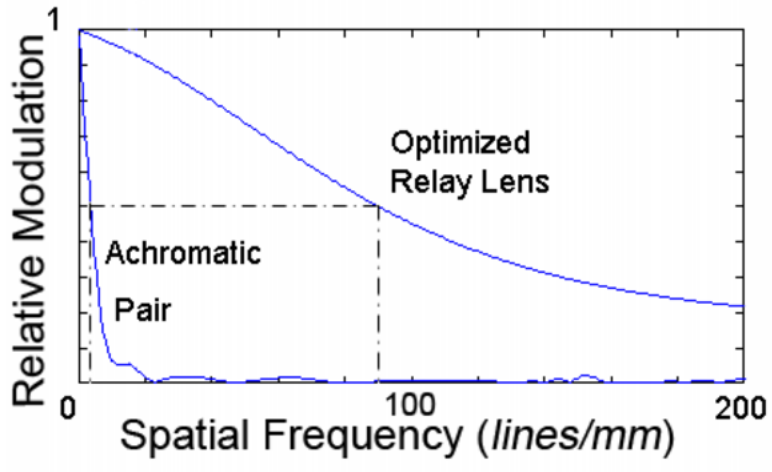

(b)

Figure 1.7: (a) Optical structure of the optimized relay lens. (b) MTFs of the mounted achromatic pair and the optimized relay lens.

is defined as the response of an optical system to multiple sine waves with different frequencies. It measures how faithfully the lens reproduces detail from the object to the image. In general, the imaging quality of a lens can be represented by the cutoff frequency of MTF [17]. According to Figure 1.7(b), the cutoff frequency of the joint optimized relay lens is up to 90 lines/mm, which is much higher than that of the achromatic pairs (<10 lines/mm).

1.3 Multiplexed Imaging Applications of Aperture Manipulation

On the external aperture provided by our CIS_RJRS, the imaging beam can be sampled, coded or split to achieve many multiplexed imaging applications. Here, we show two kinds of aperture manipulation—aperture splitting (Figure 1.8(a) and (b)) as well as aperture coding (Figure 1.8(c) and (d)). For aperture splitting, previous CIS_RSRS (Figure 1.3(d)) require one achromatic lens to be mounted in front of each sensor and thus necessitate calibrating multiple lenses and sensors. Previous CIS_FRS (Figure 1.3(f)) is not suitable for aperture splitting, due to the requirement that the splitter should be mounted in front of the imaging lens. Compared with previous CIS, splitting aperture in our CIS_RJRS is much easier and more practical. As shown in Figure 1.8(a, b), HDR imaging [6], multi-focus imaging [19] and multi-aperture photography [1] can be realized by just mounting the mirror array on the external aperture and sensors on the equivalent image planes. For aperture coding [2, 3], our CIS_RJRS allows inserting complex aperture filters and replacing the aperture modulators (Figure 1.8(c, d)), much more easily than previous methods (Figure 1.3(a)).

In this section, we focus on two of these multiplexed imaging applications, real-time HDR imaging and multi-focus imaging by splitting aperture on our CIS_RJRS.

1.3.1 Necessity of Beam-Splitting on Aperture

As shown in the Figure 1.8(a), by mounting a reflective beam splitter (mirror array) and multiple sensors behind CIS_RJRS, we can split the aperture for multiplexed imaging applications. Now, we discuss the necessity of placing

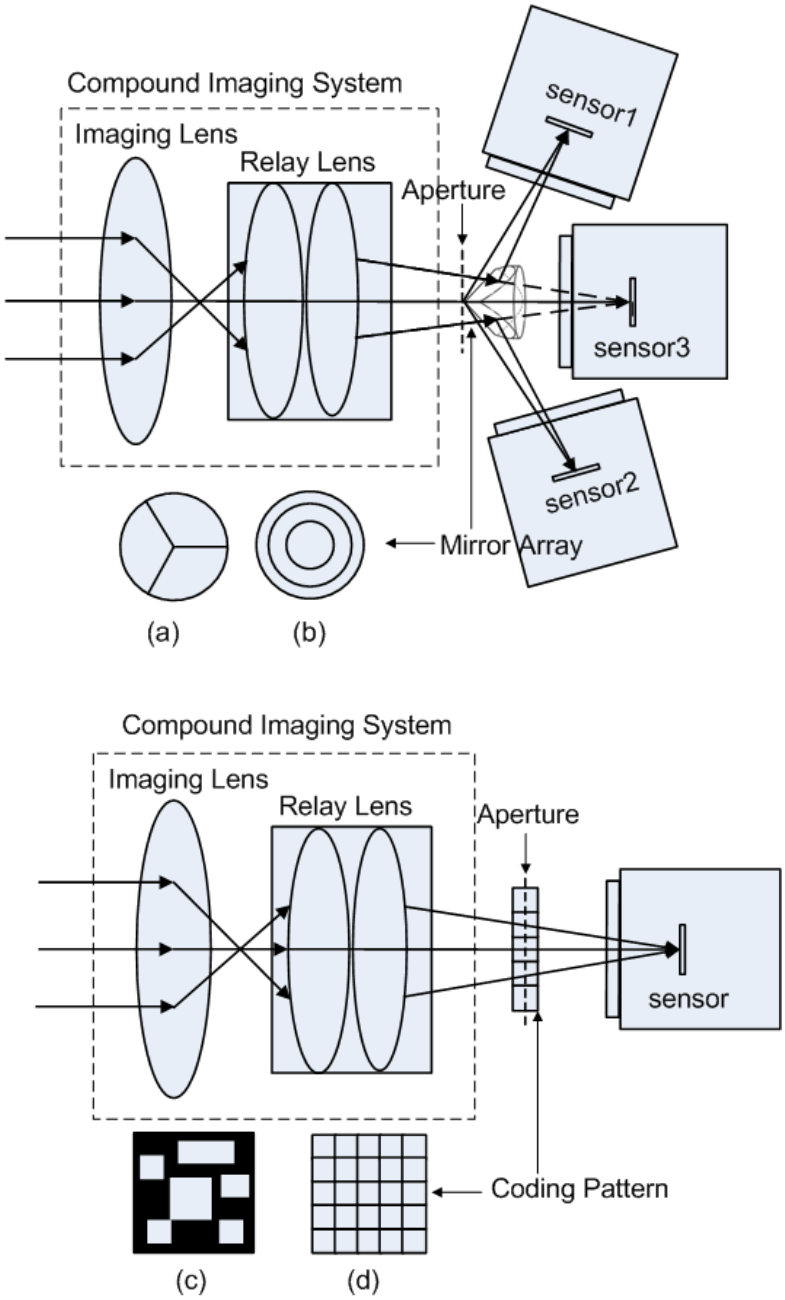

Figure 1.8: Aperture manipulation with our CIS_RJRS. (1) Aperture splitting: (a) HDR imaging and multi-focus imaging using fan-shaped mirror array and (b) multi-aperture photography using circular mirror array. (2) Aperture coding using (c) coding pattern and (d) SLM.

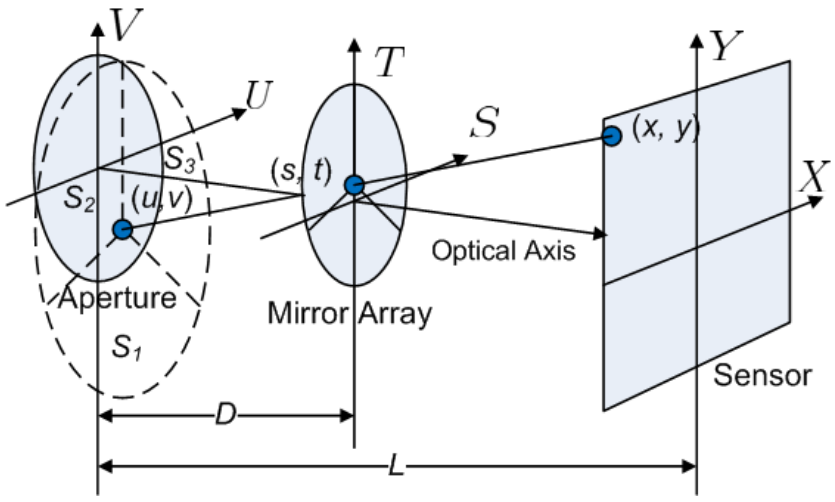

Figure 1.9: Vignetting in images captured through sub-apertures. Each facet of the mirror array reflects a part of the incoming rays and forms an image on its corresponding sensor. By projecting the mirror array onto the aperture plane $U - V$, the aperture is partitioned into three sub-apertures (S_1,S_2, and S_3, depicted by dashed lines). The lightness of pixel (x, y) is proportional to the area of the corresponding sub-aperture.

the mirror array on the aperture plane, along with the optical axis. As shown in Figure 1.9, suppose the distance between the aperture and the sensor is L, we place the mirror pyramid at the distance of D from the aperture plane, with an offset (s, t) from the optical axis. Along the rays arriving at any pixel (x, y) on the sensor, we can project the mirror onto the aperture. The projection of the mirror center is (u, v).

$$\begin{cases} u = s + (s - x)\frac{D}{L-D}, \\ v = t + (t - y)\frac{D}{L-D}. \end{cases} \tag{1.3}$$

We partition the aperture plane into three sub-apertures (S_1, S_2, and S_3). If D is nonzero, the coordinates (u, v) of the mirror center and the size of sub-apertures depend on the location of the corresponding pixel (x, y) on the sensor. In this case, the size of the sub-aperture ($S_i, i = 1, 2$, or 3) varies as the pixel (x, y) moves from the sensor center to its edge, which causes the vignetting effect (the intensity variation across sensor). Therefore, to suppress the vignetting effect, we should mount the mirror array with its vertex on the aperture ($D = 0$). This ensures that every pixel on the same sensor is identi-

cally exposed. Thus, we mount the splitter on the aperture with offset (s, t) from the optical axis and capture images through sub-apertures. For HDR imaging, each sensor should capture the images through the sub-apertures of different sizes, which requires the offset (s, t) is nonzero. For multi-focus imaging, each sensor stands at different position along the optical axis, capturing images though sub-apertures of the same size $(s = 0, t = 0)$.

1.3.2 Splitting Aperture for Extending HDR

As shown in Figure 1.8, we place a mirror array on the aperture of our CIS_RJRS and shift it in the aperture plane to split the aperture asymmetrically. Through sub-apertures of various sizes, we can capture multi-exposure images. The dynamic range of the CCD detector can be defined as the ratio of the maximum to the minimum electron charge measurable by the potential wells, or as the ratio of the maximal ($I_{\max}$) to the minimal ($I_{\min}$) detectable radiances [14], as shown in Eq. (1.4). This HDR imaging system enhances the normal dynamic range by the area ratio of the maximal to minimal sub-apertures, as shown in Eq. (1.4). In addition, we can choose a mirror array with 6 or more facets to widen the dynamic range.

$$\begin{aligned} \mathrm{DR} &= 20 \log \tfrac{I_{\max}}{I_{\min}}, \\ \mathrm{HDR} &= 20 \log (\tfrac{I_{\max}}{I_{\min}} \tfrac{\max\limits_i S_i}{\min\limits_i S_i}). \end{aligned} \tag{1.4}$$

1.3.3 Splitting Aperture for Extending DOF

Each lens camera can only capture a sharp image for objects at the specific range of distance, or called depth-of-field (DOF). Depth-of-field is defined as the distance between the near and far points in outside scene, whose images on the sensor is smaller than the confusion circle c, where c is often set to be the pixel size. The DOF becomes shallower when increasing the size d of aperture. As shown in Figure 1.8(a), multiple sensors can capture images of the same scene though sub-apertures of our CIS_RJRS. By shifting these sensors along the optical axis such that their DOFs are concatenated without any overlapping, we can implement CIS_RJRS for multi-focus imaging with

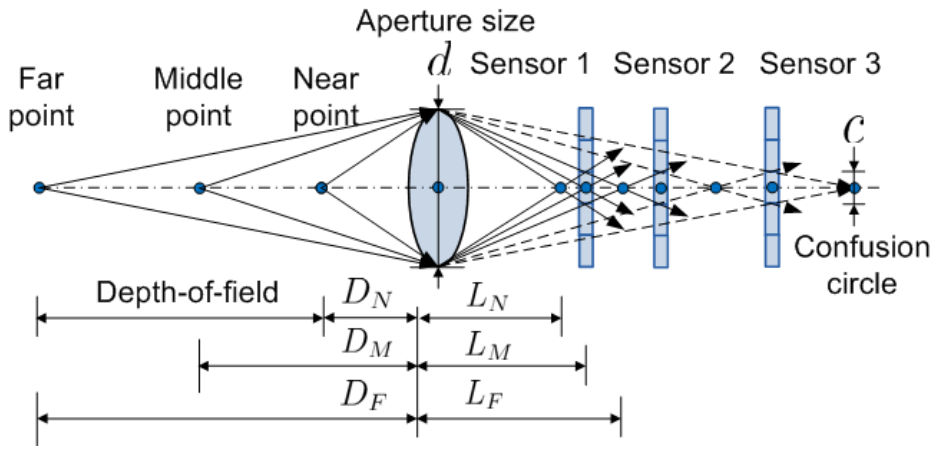

Figure 1.10: Extending the depth-of-field (DOF) in multi-focus imaging.

an extended DOF, as shown in Figure 1.10. For simplicity of notation, we set the far point of sensor 1 at the infinity distance (i.e., $D_F = \inf, L_F = f$, where f is the focal length). Then, the DOF of sensor 1 can be denoted by the distance D_N of its near point. According to Gaussian lens formulas $\frac{1}{D_N} + \frac{1}{L_N} = \frac{1}{f}$ and $L_F = f$, we induce $L_N = \frac{d+c}{d-c}f$ and its corresponding $D_N = \frac{d+c}{2c}f$. If n sensors are concatenated, the extended DOF is specified by the nearest focus distance D_N^n, satisfying the following relationship.

$$\begin{cases} L_N^n = \frac{(d+c)^n}{(d-c)^n}f, \\ D_N^n = \frac{(d+c)^n}{(d+c)^n-(d-c)^n}f. \end{cases} \tag{1.5}$$

1.4 Simulation and Experimental Results

In this section, we will show some experimental results obtained from our CIS_RJRS consisting of a conventional imaging lens and an off-the-shelf relay lens. We also demonstrate that CIS_RJRS is a practical solution to aperture access and manipulation. In the following subsections, we will describe the CIS_RJRS prototype, as well as its calibration, evaluation, and applications.

Table 1.1: Parameters of COSMICAR imaging lens and TECHSPEC relay lens in CIS_RJRS, where EFL and BFL respectively stand for effective and back focal length.

Name	EFL	$f/\#$	L_1
COSMICAR Imaging Lens	25 mm	≥ 1.4	47.5 mm
Name	EFL	$f/\#$	BFL
TECHSPEC Relay Lens	45 mm	4.0	-12.5 mm

Table 1.2: Intrinsic parameters of the imaging system with or without the relay lens.

Name	Focal Length (mm)	Principal Point (pixels)	Distortion
COSMICAR Imaging Lens	$f_x = 25.39$ $f_y = 26.62$	$cc(1) = 579.25$ $cc(2) = 353.31$	$kc(1) = -0.20077$ $kc(2) = -15.07476$
Compound Imaging System2	$f_x = 25.73$ $f_y = 26.97$	$cc(1) = 631.71$ $cc(2) = 380.80$	$kc(1) = -0.50684$ $kc(2) = 7.28243$

1.4.1 CIS_RJRS Prototype and Calibration

Since CIS_RJRS repositions both the aperture and image planes outside the relay system, inserting the aperture modulator does not impose any requirement on choosing relay system. Thus, to construct CIS_RJRS, we choose the TECHSPEC relay lens which is globally optimized, i.e., its object and image lenses are jointly designed to achieve the best imaging quality. Using the optical design software ZMAX, we simulate its modulation transfer function (Figure 1.7(b)) and imaging parameters (Table 1.1). According to BFL $= f - L_4 = -12.5$ mm and EFL$= f = 45$ mm, the focal point should lie inside the relay lens. By the condition $L_1 < \frac{f^2}{L_4 - f} - f$ in Section 1.2.2, we conclude that the TECHSPEC relay lens is only suitable for those imaging lenses with their secondary aperture $L_1 < 117$ mm. In general, since the secondary apertures of most imaging lenses satisfy $L_1 < 100$ mm, this optimized relay lens is capable of accessing the aperture of most lenses. We choose a COSMICAR imaging lens, as shown in Table 1.1. We refocus a LEICA microscope to get the secondary aperture in focus and then adjust the microscope to focus on the mounting plane. The adjustment in distance is an estimate of the position ($L_1 = 47.5$ mm) of the aperture. Thus, we can

access the aperture of this COSMICAR lens.

The relative aperture of the relay lens is equal to the reciprocal of $f/\#$ ($D_2/L_2 = \frac{1}{f/\#} = 1/4.0$). As discussed in Section 1.2.2, it is required that the relative aperture of the imaging lens satisfies $D_1/L_1 \leq 1/5.6$ to avoid vignetting. In this case, the aperture of the relay lens is ineffective. In other words, the aperture of the CIS_RJRS is the one located in the imaging lens, or its image behind CIS_RJRS.

We build a CIS_RJRS prototype by mounting the imaging lens and relay lens on a optical bench (Figure 1.12(a)). We continue adjusting their relative positions until the two lenses are concentric. The mounting and calibrating process is simpler for CIS_RJRS, compared to the previous method that uses a separate achromatic pair. Using the Camera Calibration Toolbox [20], we estimate the intrinsic parameters of the imaging lens and the CIS_RJRS prototype, respectively (Table 1.2). The focal length of the CIS_RJRS prototype is slightly different from that of the COSMICAR imaging lens, which indicates the magnification ratio of the relay lens is 1:1. The difference between the principal points of CIS_RJRS and the imaging lens is due to the misalignment between the relay lens and the imaging lens. It should be noted that the distortion of the CIS_RJRS prototype, which is due to both the imaging lens and the relay lens, is more than twice that of the COSMICAR imaging lens.

1.4.2 Evaluation of Image Quality of CIS_RJRS

In general, due to the insertion of an additional relay lens, the image quality of CIS_RJRS can be expected to decrease to some extent compared to that of the conventional imaging lens. In this section, we test the image quality of the CIS_RJRS prototype using simulation and experimental data.

As shown in Section 1.2.3, our rear-attached relay system allows the use of a globally optimized relay lens. We analyze the performance of CIS_RJRS in terms of the imaging quality of the relay lens, specifically MTF and point spread function (PSF). The MTF of the optimized relay lens has a half-cutoff frequency up to 90 lines/mm (Figure 1.7(b)). We also evaluate the imaging quality of the optimized relay lens in terms of the spatial domain version of MTF—PSF. PSF is the response of an imaging system to a point source.

The PSF of a perfect imaging system is assumed to be one point. Using ZMAX, we can simulate the PSF and the spot diagram of the optimized relay lens (Figure 1.11). The diameter of the diffusion disc is roughly 10 microns, roughly the size of two pixels. From this simulation result, we conclude that the spherical aberration of this relay lens is quite small. To measure the PSF of CIS_RJRS, we place a tiny light point in front of the imaging lens and mount a digital camera (SONY DFW-sx900) at the equivalent image plane of CIS_RJRS (Figure 1.12(a)). To obtain a symmetrical PSF, we capture multiple images of the shifted point source. The PSF of CIS_RJRS is obtained by normalizing the average of those images so that the sum of its elements equals one. As shown in Figure 1.13, the PSF of CIS_RJRS is very close to that of the COSMICAR imaging lens without the relay lens, and their diffusion discs only cover the 3×3 pixel patch (pixel size: 4.65×4.65 microns). The measured PSF of CIS_RJRS is close to the simulated PSF of the optimized relay lens.

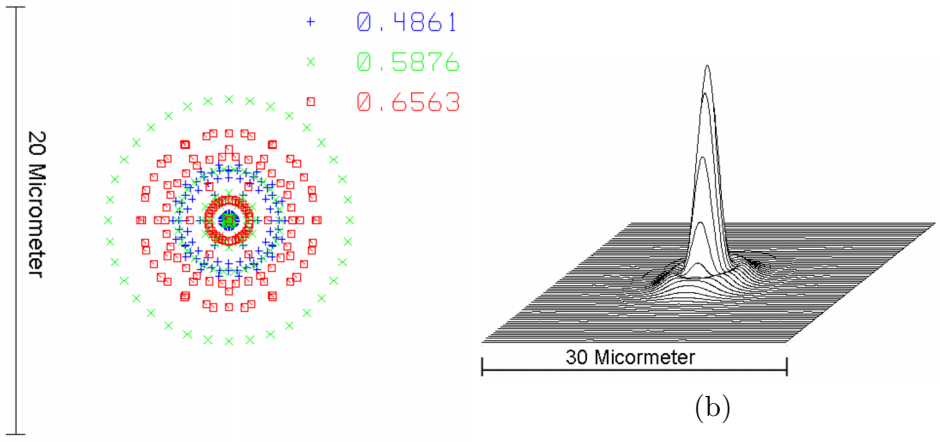

Figure 1.11: Parameters of optimized relay lens from simulation. (a) Spot diagram, which is distribution of three imaging beams (red, green and blue) on the image plane from a single point source. (b) Point spread function.

We now describe our experiments on qualitative evaluation of the imaging quality of CIS_RJRS. Initially, we capture an image using a regular camera (Cosmicar imaging lens and SONY DFW-SX900) as the original image (Figure 1.14(a)(d)). As shown in Figure 1.12(a)(b), we build up CIS_RJRS with two kinds of relay lenses (the optimized relay lens and the achromatic pair

from Edmund Optics) and respectively capture an image of the same scene. The image (Figure 1.14(b)(e)) captured with the optimized relay lens retains most of the contrast of the original image (Figure 1.14(a)(d)). But the image (Figure 1.14(c)(f)) captured with the achromatic pair is significantly blurred. These results are consistent with the simulated MTF of the optimized relay lens and the achromatic pair (Figure 1.7(b)).

(a) (b)

Figure 1.12: (a) CIS_RJRS prototype using optimized relay lens, and (b) CIS_RJRS prototype using achromatic pair.

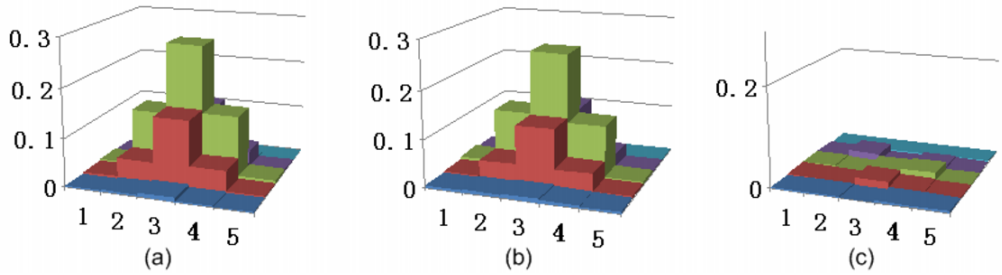

Figure 1.13: (a) Measured PSF of COSMICAR imaging lens, (b) measured PSF of compound imaging lens, and (c) their difference.

1.4.3 Accessible Aperture and Imaging Planes behind CIS_RJRS

In this section, we demonstrate that CIS_RJRS indeed repositions the accessible aperture and image planes behind it.

According to Eq. (1.2), if the relative aperture (the ratio of aperture size to focal length) of COSMICAR is adjusted to below 1:5.6 such that any incoming beam passing through it will not be blocked by the relay lens, the CIS_RJRS prototype provides the equivalent aperture and image planes without causing the vignetting effect. To detect the positions of the accessible

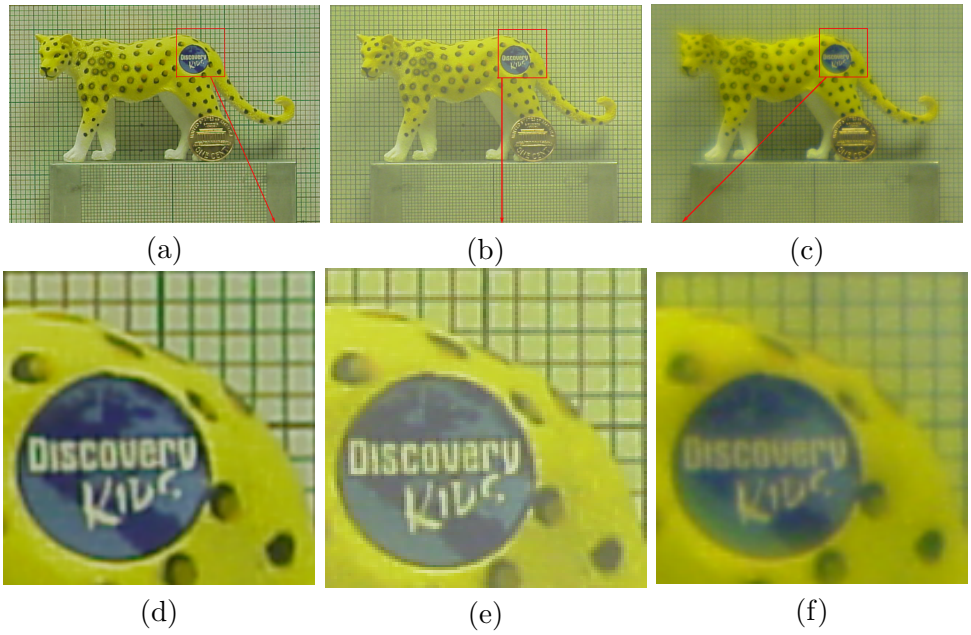

Figure 1.14: (a) Original image with close-up (d), (b) image captured with optimized relay lens with close-up (e), (c) image captured with achromatic pair with close-up (f).

aperture and image planes, we place a diffusive screen just behind the relay lens (Figure 1.15(a)). While moving away from the relay lens, the screen displays different patterns (Figure 1.15(b, c, d, e)). The position of the equivalent aperture is the one where the sharp hexagonal pattern is observed (Figure 1.15(c)), which demonstrates that the CIS_RJRS prototype indeed provides an external aperture behind it. On this accessible aperture plane, we can place any aperture modulator (filters, mirror arrays, or lens arrays) to access and manipulate the aperture. To show the vignetting effect, we capture the image of a uniform lighting box by mounting a camera (AVT Guppy F-033) behind the CIS_RJRS prototype. With the same illumination and aperture setting, we capture the image formed between the imaging lens and the relay lens. When the relative aperture of the imaging lens is adjusted to below 1:5.6, the image formed behind CIS_RJRS has the same intensity as that formed behind the COSMICAR imaging lens in the center and decreases to 84% at the corner, as shown in Figure 1.16. This kind of vignetting effect is tolerable in computational imaging and can be corrected by calibration.

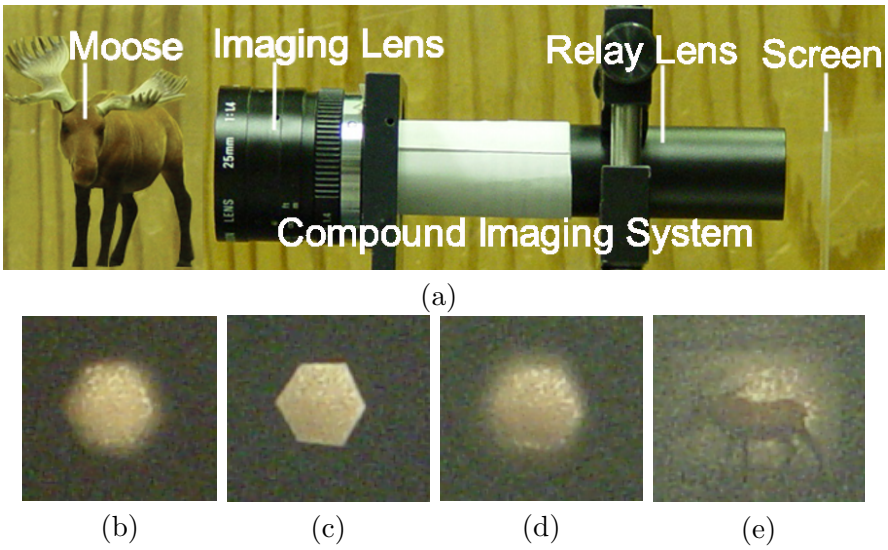

Figure 1.15: Accessible aperture and image planes behind our CIS. (a) CIS prototype. The patterns on the screen when it stands (b) in front of, (c) on, (d) behind the aperture plane, and (e) on the image plane. The sharp hexagonal pattern indicates the position of the accessible aperture.

1.4.4 Aperture-Splitting for HDR Imaging

In this section, we split the external aperture of CIS_RJRS for HDR imaging, similar to [6] except that we replace the costly customized lens with the proposed CIS_RJRS. As shown in Figure 1.17, we use a three-facet mirror array to partition the equivalent aperture and direct the beam reaching each sub-aperture onto its corresponding sensor. For image acquisition, we choose three cameras (AVT Guppy F-033). The HDR imaging system is constructed by simply mounting the mirror on the equivalent aperture and the sensors on the image planes. By shifting the mirror array in the direction perpendicular to the optical axis, we split the aperture unevenly and capture multi-exposure images through various sub-apertures (Figure 1.18(a, b, c)). Since almost no rays are blocked or absorbed by the mirror array, we can make full use of the common imaging beam provided by CIS_RJRS. For the HDR image reconstruction, we choose the gradient-domain fusion algorithm in [21], which constructs the synthetic gradient field by suppressing large gradients and then searches the optimal image intensity whose gradient field is closest to the synthetic one. From the HDR reconstruction, CIS_RJRS captures the clear image of objects under extreme illumination conditions, such

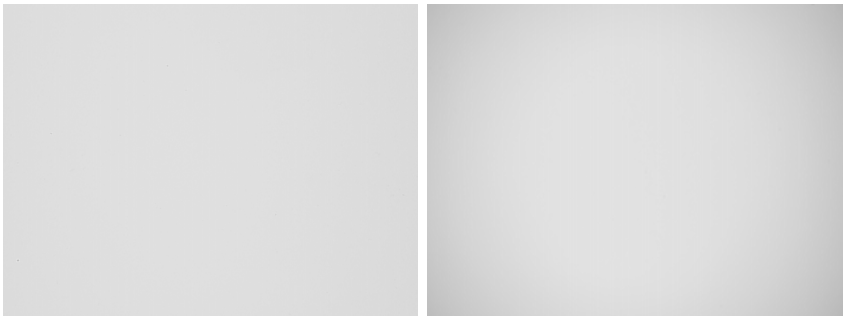

(a) (b)

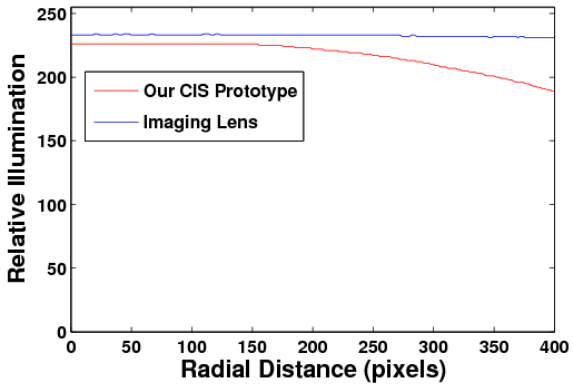

(c)

Figure 1.16: Vignetting calibration at the imaging lens $f/\# = 5.6$. Images captured from (a) COSMICAR imaging lens and (b) CIS_RJRS prototype. (c) Illumination chart (from center to corner).

as shading and specular surfaces. The synthetic HDR image (Figure 1.18(d)) illustrates that CIS_RJRS provides a practical solution to aperture-splitting based HDR imaging.

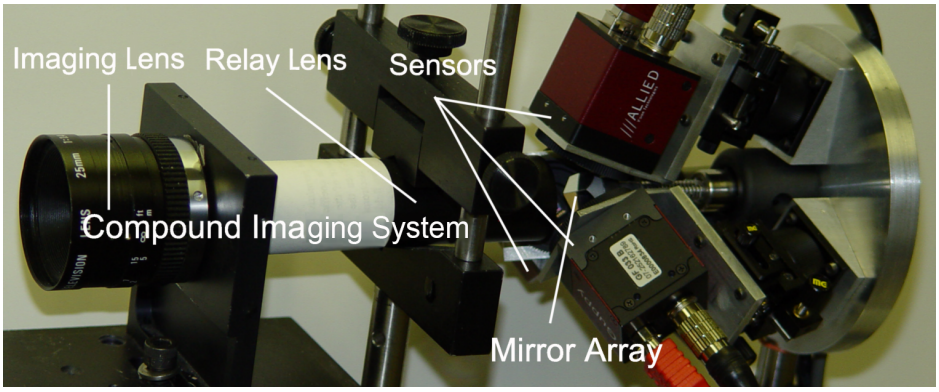

Figure 1.17: Prototype of a high dynamic imaging system constituted by CIS_RJRS.

1.4.5 Aperture-Splitting for Multi-Focus Imaging

In this section, we implement another multiplexed application—multi-focus imaging on the CIS_RJRS prototype. Our multi-focus imaging camera is similar to the HDR imaging camera (Figure 1.17), except that (1) the three sensors are mounted at different positions along the optical axis and (2) the aperture is evenly split in our multi-focus imaging camera. Thus, multi-focus imaging camera can capture three images under identical exposure with different focus distance, as shown in Figure 1.19(a)(b)(c). From these three varying-focus images, we can fuse a multi-focus image by (1) detecting the in-focus regions for each image and combining the in-focus regions by the gradient-fusion algorithms [21], as show in Figure 1.19(d).

1.5 Summary

In this chapter, we propose a practical solution to accessing and manipulating aperture—CIS_RJRS. CIS_RJRS can provide external access to both aperture and image planes behind the imaging lens, without any structural modification on the imaging lens or using a custom lens. Different from

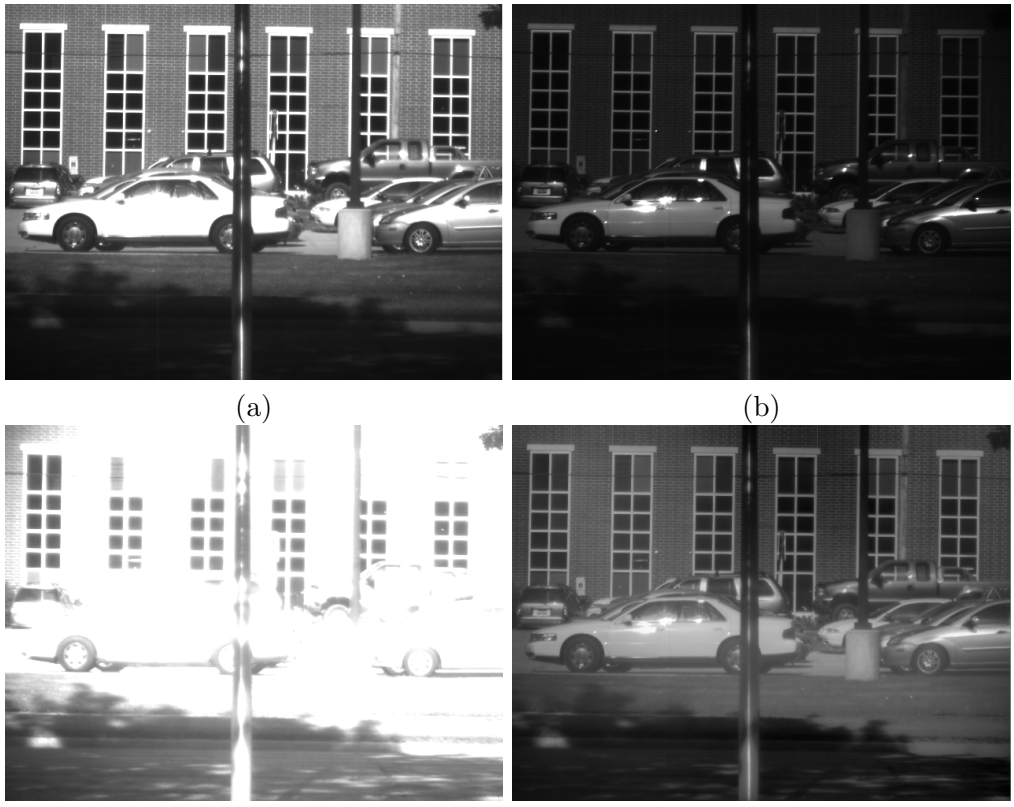

Figure 1.18: (a) Under-exposure image, (b) normally exposed image, (c) over-exposure image, and (d) fused HDR image.

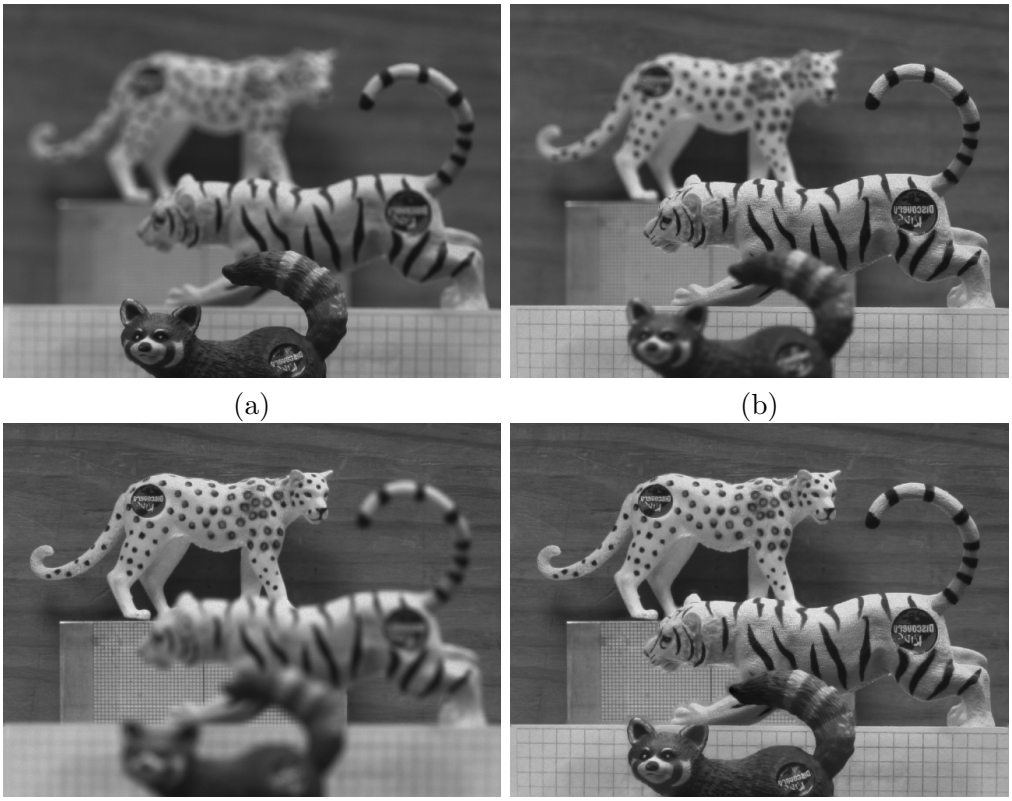

(a) (b)

(c) (d)

Figure 1.19: (a) Near-focus image, (b) mid-focus image, (c) far-focus image, and (d) fused multi-focus image.

previous rear-attached separate relay system CIS_RSRS, our CIS_RJRS relocates the aperture outside of the relay lens and allows inserting an aperture-manipulating pattern without harming the imaging quality. Thus, CIS_RJRS can maintain the high imaging quality of the imaging lens. Compared with the front-relocated aperture of previous CIS_FRS, the rear-relocated aperture provided by CIS_RJRS can be manipulated for different multiplexed imaging applications, such as aperture coding for depth acquisition and light field acquisition, aperture splitting for real-time HDR imaging and multi-focus imaging. The CIS_RJRS prototype and two of its applications are presented to show that our CIS_RJRS is indeed a practical solution to aperture access and manipulation for multiplexed imaging.

Admittedly, CIS_RJRS requires a high-quality, large-aperture joint relay lens, which can be used with ordinary imaging lenses. However, this kind of relay lens is much easier to design than a high-quality imaging lens with external aperture. Given a high-quality relay lens that satisfies the requirements of Section 1.2.2, our new imaging system CIS_RJRS is quite promissing in many computational imaging applications

CHAPTER 2

HYBRID COMPRESSIVE SAMPLING (HCS) VIA TVL1

2.1 Introduction

Digital images or signals are conventionally acquired by Nyquist/Shannon sampling. That requires, to incur no loss, the underlying analog signal must be sampled at the Nyquist rate which is at least twice its highest analog frequency. The resulting raw digital data is too large to sense, transmit and store in many applications. One solution to this problem is the well-known image compression methodology, such as the JPEG2000 [22] compression standard, which represents a digital image by a smaller number of dominant components and relaxes the storage and transmission requirements. However, sensing a large image is still challenging.

Recently, compressive sensing [23] or particularly compressive sampling, has been introduced to address this problem more efficiently. CS exploits the redundancy present in the image at the time of sampling itself. Instead of sensing all the pixels that define the complete image, compressive sampling acquires a linear combination of randomly selected pixels and recovers the full image from these samples [24, 25, 26, 27, 28]. Instead of first sampling and then compressing, this imaging model avoids sampling of the redundant aspects of the data in the first place.

Compressive sampling assumes that an image (vectorized as I, size: L) can be represented as $I = \Psi z$ in the Ψ-transform domain, where z has K nonzero elements (called K-sparsity). Instead of sensing z directly in the Ψ-transform domain, it may be easier to efficiently sample I in a different subspace defined by Φ. Then, sensing acquires a small number of projections of I onto this subspace such that $b = \Phi I$, where $\Phi \in \mathbb{C}^{M \times L} (K < M < L)$ is a sampling matrix. Given the measurements b, CS recovers the K dominant components constituting z. Thus, the original image I or its coefficients z

can be recovered from compressive samples b as follows:

$$\min_I \quad \|\Psi^T I\|_0 \quad \text{s. t.} \quad \Phi I = b, \tag{2.1}$$

$$\text{or,} \quad \min_z \quad \|z\|_0 \quad \text{s. t.} \quad Az = \Phi\Psi z = b. \tag{2.2}$$

However, ℓ_0-norm minimization is an NP-complete problem [29]. Fortunately, it has been proven that the intractable ℓ_0-problem is equivalent to the convex ℓ_1 minimization, if the sampling matrix $A = \Phi\Psi$ obeys uniform uncertainty principle (UUP), introduced in [30] and refined in [31]. According to the definition in [31], a measurement matrix $A \in \mathbb{R}^{M\times L}$ is said to obey UUP, if the inequality,

$$\frac{1}{2}\cdot\frac{M}{L}\|z\|_2^2 \le \|Az\|_2^2 \le \frac{3}{2}\cdot\frac{M}{L}\|z\|_2^2, \tag{2.3}$$

holds for all $K-$sparse signals z. According to [30], random sampling matrix and Fourier sampling matrix both obey UUP, if $M \ge \alpha\Delta K$, where $\alpha > 0$ is a constant, $\Delta = \log(L/K)$ for the random matrix and $\Delta = \log^6(L/K)$ for the Fourier matrix. They are capable of recovering z (with an overwhelming probability) from b of size $M \ge \alpha K\log(L/K)$ and $M \ge \alpha K\log^6(L/K)$, respectively.

In addition to the sparsity in the Ψ-transform domain (wavelets [26, 25], curvelets [32] et al.), compressive sampling often uses Total Variation (TV) [33] to exploit the sparsity in finite difference domain. In some applications [32, 34, 35, 36], Ψ-transform sparsity and TV are enforced together to improve the recovery accuracy as follows:

$$\min_z \mathrm{TV}(I) + \lambda\|\Psi^T I\|_1 \quad \text{s. t.} \quad \|\Phi I - b\|_2^2 \le \sigma^2, \tag{2.4}$$

where λ trades TV with Ψ-transform sparsity and σ^2 is the noise variance.

In this chapter, we concentrate on how to evaluate and improve TV-based compressive sampling. The most widely used form of TV in CS [24, 25, 26, 34, 36] including the Single-Pixel Camera (SPC) [28] is TVL1L2, denoted as $\mathrm{TV}_{\ell_1\ell_2}$, which computes the summation of the magnitudes of gradients (SMG) across the image: $\mathrm{TV}_{\ell_1\ell_2}(I) = \sum_i \sqrt{(D_h I)_i^2 + (D_v I)_i^2}$ where D_h and D_v are horizontal and vertical gradient operators. This TV measure has the following shortcomings: (1) The gradient magnitude field is not as sparse as

partial gradients fields; (2) $\mathrm{TV}_{\ell_1\ell_2}$ is prone to causing blurring across sharp edges, since SMG prefers to suppress large partial gradients; (3) SMG is a nonlinear operator, which makes it difficult to minimize $\mathrm{TV}_{\ell_1\ell_2}$ efficiently. For the efficiency of the decoding algorithm, [37] employs a TV measure that calculates the ℓ_1-norm of partial gradients $\|D_h I\|_1 + \|D_v I\|_1$, which is a simplified version of TVL1, denoted as TV_{ℓ_1}. This simplified version of TV_{ℓ_1} seeks the intensity continuity horizontally and vertically, but fails to enforce the intensity continuity diagonally. Thus, to overcome these shortcomings of the existing TV measures in compressive sampling, we propose a new TV measure TV_{ℓ_1}.

In CS, random sampling is generally assumed to be near-optimal in reducing the sampled data for unstructured images Donoho06,Candes0502. The references [24, 25, 26] combine low-frequency sampling and random sampling, on intuitive grounds alone, without formal justification. In this chapter, we present a hybrid CS method using a new TV measure with the following two contributions:

1. We propose a new TV measure TV_{ℓ_1}, which recovers piecewise smooth images with all possible sharp edges by exploiting the sparsity and continuity in the gradient domain. In addition, the UUP condition shows our TV_{ℓ_1} achieves higher accuracy and requires fewer measurements for the same quality of reconstruction than previous $\mathrm{TV}_{\ell_1\ell_2}$.

2. We present a theoretical analysis on hybrid sampling, which shows that low resolution sampling (LRS) and random sampling (RS) indeed complement each other for most natural images, and gives the criteria for the best combination of LRS and RS.

This chapter is organized as follows. Section 2.2 describes our TV_{ℓ_1} based hybrid CS. Section 2.3 discusses implementation of our method. Section 2.4 presents experimental results. Section 2.5 gives concluding remarks.

2.2 Proposed Hybrid CS with TVL1

Total variation $\mathrm{TV}_{\ell_1\ell_2}$ is a widely used measure for enforcing intensity continuity and recovering a piecewise smooth image in CS [24, 25, 26, 34, 36]. In this chapter, we propose a new TV measure TV_{ℓ_1}, which exploits the

continuity and sparsity in the partial gradient domain. In comparison with $\mathrm{TV}_{\ell_1\ell_2}$, our TV_{ℓ_1} is able to recover sharper images with greater accuracy. Our TV_{ℓ_1} based CS problem can be formulated as follows.

$$\min_I \mathrm{TV}_{\ell_1}(I) \quad \text{s. t.} \quad \Phi I = b \quad \text{and} \quad \Phi' I = d, \tag{2.5}$$

where Φ is a random sampling (RS) matrix or Fourier sampling matrix for large-scale images, and Φ' is a low-resolution sampling (LRS) matrix, which acquires LR data d. To compare our TV_{ℓ_1} with $\mathrm{TV}_{\ell_1\ell_2}$ directly, we do not combine our TV_{ℓ_1} with any Ψ-transform sparsity, even if their combination might improve the recovery accuracy.

2.2.1 A New TV Measure

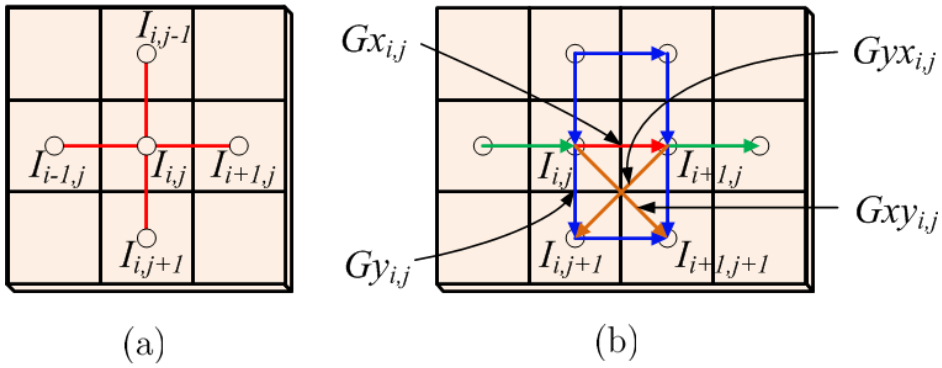

Figure 2.1: (a) For intensity continuity, or gradient sparsity, we enforce each pixel, e.g. $I_{i,j}$, to be continuous with its four neighbors. (b) For gradient continuity, we enforce each partial gradient, e.g. $Gx_{i,j}$ marked as a red line, to be of similar value to its six neighbors marked as blue lines.

In this section, we present a new TV measure TV_{ℓ_1}. For intensity continuity in Figure 2.1(a), the pixel $I_{i,j}$ is desired to be of similar value to its four neighbors in smooth regions. Similarly, partial gradients $Gx_{i,j} = I_{i+1,j} - I_{i,j}$ and $Gy_{i,j} = I_{i,j+1} - I_{i,j}$ can be continuous along all directions except their own directions, where they are desired to be discontinuous to obtain a sharp edge. Take $Gx_{i,j}$ (Figure 2.1(b)) for example, our TV_{ℓ_1} will not enforce its continuity along the horizontal axis, but will do so along all other directions, as in Figure 2.1(b)). For notational simplicity, we consider the continuity

of partial gradients in a 2×2 neighborhood $(I_{i,j}, I_{i+1,j+1}, I_{i+1,j}, I_{i,j+1})$. The continuity constraints depend on the direction $\overrightarrow{D}$ associated with the edge, if it exists in the neighborhood. For different cases of $\overrightarrow{D}$, the continuity constraints are:

$$\begin{cases} \|Gxx_{i,j}\|_1 = \|Gx_{i,j} - Gx_{i,j+1}\|_1 = 0 & \text{if } \overrightarrow{D} \text{ is vertical.} \\ \|Gyy_{i,j}\|_1 = \|Gy_{i,j} - Gy_{i+1,j}\|_1 = 0 & \text{if } \overrightarrow{D} \text{ is horizontal.} \\ \|Gxy_{i,j}\|_1 = \|Gx_{i,j} + Gy_{i+1,j}\|_1 = 0 & \text{if } \overrightarrow{D} \text{ is left-lower.} \\ \|Gyx_{i,j}\|_1 = \|Gy_{i,j} - Gx_{i,j}\|_1 = 0 & \text{if } \overrightarrow{D} \text{ is right-lower.} \end{cases}$$

Thus, we enforce the directional continuity of Gx and Gy by minimizing the ℓ_1-norm of Gxy, Gyx, Gxx and Gyy. $Gxx_{i,j}$ is the derivative of $Gx_{i,j}$ along the vertical axis and $Gyy_{i,j}$ is the derivative of $Gy_{i,j}$ along the horizontal axis. Actually, $\|Gxx_{i,j}\|_1 = \|I_{i+1,j+1} + I_{i,j} - I_{i+1,j} - I_{i,j+1}\|_1 = \|Gyy_{i,j}\|_1$. By including the intensity continuity constraints in Figure 2.1(a), we define our TV measure TV_{ℓ_1} as follows:

$$\mathrm{TV}_{\ell_1}(I) = \|Gx\|_1 + \|Gy\|_1 + \gamma(\|Gxy\|_1 + \|Gyx\|_1 + 2\|Gxx\|_1), \qquad (2.6)$$

where γ trades the intensity continuity with the gradient continuity. Gx, Gy, Gxy and Gyx are respectively horizontal, vertical, and two diagonal partial gradients in Figure 2.1(b). Given our goal is to recover the sparsest gradients, $\|Gxx_{i,j}\|_1 = \|Gyy_{i,j}\|_1 = 0$ implies zero partial gradients along one of four directions in the 2×2 neighborhood, or equivalently $Gx_{i,j} = 0$, $Gy_{i,j} = 0$, $Gxy_{i,j} = 0$ or $Gyx_{i,j} = 0$. In this case, minimizing $\|Gxx\|_1$ is redundant under the condition of minimal $\|Gx\|_1 + \|Gy\|_1 + \|Gxy\|_1 + \|Gyx\|_1$. Thus, our TV_{ℓ_1} can be simplified.

$$\mathrm{TV}_{\ell_1}(I) = \|Gx\|_1 + \|Gy\|_1 + \gamma(\|Gxy\|_1 + \|Gyx\|_1). \qquad (2.7)$$

This simplified TV_{ℓ_1}, enforces the sparsity and directional continuity in the gradient domain by seeking the γ-weighted sparsity of partial gradient fields $G = [Gx; Gy; Gxy; Gyx]$.

In comparison with previous TV measures ($\mathrm{TV}_{\ell_1\ell_2}$ and TV_{ℓ_1} when $\gamma = 0$), our TV_{ℓ_1} based CS can recover any piecewise smooth image with all possible sharp edges (horizontal, vertical or diagonal), where the tuning parameter γ plays a crucial role in determining its preference. In general, TV-based CS

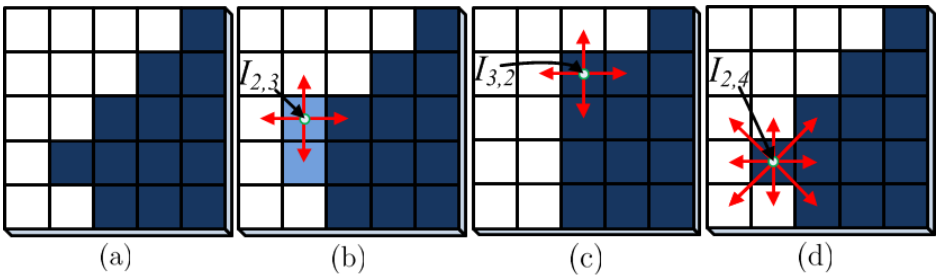

Figure 2.2: Comparison of TV measures (the intensities of white, dark-blue and light-blue pixels are 1, 0 and 0.5). (a) Original sharp corner, (b) blurred image recovered by minimizing $\mathrm{TV}_{\ell_1\ell_2}$, (c) straight edge image recovered by minimizing $\mathrm{TV}_{\ell_1,\gamma=0}$, (d) diagonal corner image recovered by minimizing $\mathrm{TV}_{\ell_1,\gamma=1}$.

seeks the image that has the minimal TV value and is closest to the measurements. The widely used measure $\mathrm{TV}_{\ell_1\ell_2}$ minimizes the sum of magnitudes of gradients (SMG) and penalizes larger partial gradients. Thus $\mathrm{TV}_{\ell_1\ell_2}$ is prone to recovering a blurred image (Figure 2.2(b)). The simlified version $\mathrm{TV}_{\ell_1,\gamma=0}$, is prone to recovering an image of sharp horizontal and vertical edges in Figure 2.2(c) by enforcing $\|Gx\|_1 + \|Gy\|_1$. However, these two images (Figure 2.2(b)(c)) cause larger ℓ_1-norm of Gyx. $\mathrm{TV}_{\ell_1,\gamma=1}$ equally penalizes the ℓ_1-norm of each elements in the four partial gradient fields G, whether large or small. So, $\mathrm{TV}_{\ell_1,\gamma=1}$ is prone to recovering the sharp image of diagonal edges (Figure 2.2(d)), since it has small $\mathrm{TV}_{\ell_1,\gamma=1}$ and is closest to the original image (Figure 2.2(a)).

2.2.2 UUP Condition for TV_{ℓ_1} Based CS

In this section, we present the UUP condition for TV based compressive sampling. According to this UUP condition, we compare our TV_{ℓ_1} and previous $\mathrm{TV}_{\ell_1\ell_2}$ in terms of the number of measurements for lossless recovery. An image I can be represented as a linear combination of each partial gradient field plus some constant values, i.e., $I = \Psi_x Gx + I_x = \Psi_y Gy + I_y = \Psi_{xy} Gxy + I_{xy} = \Psi_{yx} Gyx + I_{yx}$, where constant vectors I_x, I_y, I_{xy} and I_{yx} are equal to some rearrangements of the first row pixels as well as the first and last column pixels. For instance, I_x is a repetition of the first column pixels. According to Eq. (2.5), $b = \Phi I = \Phi\Psi_x Gx + \Phi I_x = \Phi\Psi_y Gy + \Phi I_y = \Phi\Psi_{xy} Gxy + \Phi I_{xy} =$

$\Phi\Psi_{yx}Gyx + \Phi I_{yx}$. Suppose $\gamma = 1$ and no LRS for simplicity, our TV_{ℓ_1} based CS problem (2.5) is reformulated as:

$$\min_{G} \|G\|_1 \quad \text{s. t.} \quad AG = [b_x; b_y; b_{xy}; b_{yx}], \tag{2.8}$$

where the partial gradient fields $G = [G_1; G_2; G_3; G_4] = [Gx; Gy; Gxy; Gyx]$, the sampling matrix $A = \mathrm{diag}(A_1, A_2, A_3, A_4) = \mathrm{diag}(\Phi\Psi_x, \Phi\Psi_y, \Phi\Psi_{xy}, \Phi\Psi_{yx})$, and the sampled data $[b_x; b_y; b_{xy}; b_{yx}] = [b - \Phi I_x; b - \Phi I_y; b - \Phi I_{xy}; b - \Phi I_{yx}]$.

If replacing the objective function with $\sqrt{Gx^2 + Gy^2}$, we induce the $\mathrm{TV}_{\ell_1\ell_2}$ based CS problem. The major difference between these two TVs is $\mathrm{TV}_{\ell_1\ell_2}$ enforces the sparsity in the gradient magnitude fields and TV_{ℓ_1} enforces that of partial gradients.

Table 2.1: The sparsity of a 256× 256 LENA image in the field of gradient magnitudes and the four partial gradient fields. The partial gradient fields has similar sparsity, which is much smaller than that of the gradient magnitude field.

Gx	Gy	Gxy	Gyx	$K_{\mathrm{TV}_{\ell_1}}$	$K_{\mathrm{TV}_{\ell_1\ell_2}}$
28111	27767	28760	28633	28760	40652

Now, we compare the sparsity (denote its maximal value as $K_{\mathrm{TV}_{\ell_1}}$ or K_1) in each partial gradient field and that (denoted as $K_{\mathrm{TV}_{\ell_1\ell_2}}$ or K_2) in the gradient magnitude field. For most natural images, it is generally true that $K_1 \leq K_2$, as shown in Table 2.1. In the gradient magnitude field, K_2 is equal to the size of pixels having nonzero gradient magnitude, which equals to $\sqrt{Gx_{i,j}^2 + Gy_{i,j}^2}$ at the location (i, j). Thus, K_2 is larger than both the sparsity of Gx and that of Gy. At each pixel, the diagonal gradients $Gxy_{i,j} = Gx_{i,j} + Gy_{i+1,j}$ and $Gyx_{i,j} = Gy_{i,j} - Gx_{i,j}$. So, the sparsity of diagonal gradients Gxy or Gyx is also smaller than the gradient magnitude sparsity K_2. Thus, we reach the conclusion that $K_1 \leq K_2$ for any image.

According to Eq. (2.8), each individual sampling matrix $A_i, i = 1, 2, 3, 4$, corresponds to a partial gradient field G_i (size $N^2 \times 1$, image size: $N \times N$). For each random sampling matrix $A_i \in \mathbb{R}^{M \times N^2}, 1 \leq i \leq 4$ to obey the UUP condition Eq. (2.3), the inequality,

$$\frac{1}{2} \cdot \frac{M}{N^2} \|G_i\|_2^2 \leq \|A_i G_i\|_2^2 \leq \frac{3}{2} \cdot \frac{M}{N^2} \|G_i\|_2^2, \tag{2.9}$$

must hold for any K_1-sparsity partial gradient G_i, where $K_1 \leq M/(\alpha \log(N^2/M))$. In other words, each $A_i \in \mathbb{R}^{M \times N^2}$ obeys the UUP condition, provided that $M \geq \alpha K_1 \log(N^2/K_1)$. As far as our TV_{ℓ_1} based CS in Eq. (2.8), we need to induce the UUP condition of the big matrix A which involves all four gradient fields G. By summing the four components in Eq. (2.9), we obtain the inequality for the matrix A,

$$\begin{aligned} \frac{1}{2} \cdot \frac{M}{N^2} \sum_i \|G_i\|_2^2 \leq \quad & \textstyle\sum_i \|A_i G_i\|_2^2 \quad \leq \frac{3}{2} \cdot \frac{M}{N^2} \sum_i \|G_i\|_2^2, \\ \frac{1}{2} \cdot \frac{M}{N^2} \|G\|_2^2 \leq \quad & \|AG\|_2^2 \quad \leq \frac{3}{2} \cdot \frac{M}{N^2} \|G\|_2^2. \end{aligned} \tag{2.10}$$

Obviously, the combined sampling matrix A obeys the UUP condition, given that each sampling matrix $A_i, i = 1, 2, 3, 4$ obeys the UUP condition, or given the condition $M \geq \alpha K_1 \log(N^2/K_1)$. Suppose the gradient magnitude is sampled randomly, we can induce that the number of measurements required by previous $\text{TV}_{\ell_1 \ell_2}$ based CS is $M \geq \alpha K_2 \log(N^2/K_2)$.

Therefore, our TV_{ℓ_1} based compressive sampling requires fewer samples than $\text{TV}_{\ell_1 \ell_2}$ for the same quality of reconstruction. In other words, based on the same number of measurements, our TV_{ℓ_1} based CS will recover an image of higher quality.

2.2.3 Optimal Hybrid Sampling

For most natural images, our hybrid sampling Eq. (2.5) consisting of low-resolution sampling (LRS) and random sampling (RS) requires fewer measurements than random sampling alone for the same quality of reconstruction. In this section, we will give a theoretical analysis on the optimal hybrid sampling and its minimal number of measurements for lossless reconstruction.

Both low resolution sampling (LRS) and random sampling (RS) aim at reducing the size of sampled data non-adaptively. The major difference is that LRS measures the low-frequency information with averaging filter (block size: $n \times n$) while RS senses the combination of randomly selected data.

To demonstrate how RS and LRS complement each other in our TV_{ℓ_1} based CS, we develop a hierarchical gradient transform (HGT), similar to the Harr wavelet transform. The HGT consists of an average basis Ψ'' at the

(a) (b) (c)

Figure 2.3: (a)Hierarchical gradient transform (HGT), (b) a Bernoulli random matrix and (c) magnitude of its HGT.

coarsest level and a series of difference bases Ψ' at finer levels (Figure 2.3(a)). Consider a 2×2 block at the finest level, the three partial gradients inside this block are highly correlated. Thus, our HGT represents these partial gradients by three partial gradients at the left-upper pixel. Similarly, we can de-correlate the partial gradients in larger scale 2×2 blocks at coarser levels, as shown in Figure 2.3(a). Thus, given an image, HGT outputs a series of hierarchical gradients G' and some average responses.

For a piecewise smooth image, G' has denser nonzero elements at coarser levels, while Bernoulli random sampling (RS) senses G' almost uniformly in the HGT domain (Figure 2.3(c)). Thus, sole RS is not efficient and hybrid sampling is desired. In hybrid sampling Eq. (2.5), we measure the coarser levels of G' by LRS, and the rest finer levels of G' (denoted by G'_d) by random sampling (RS). Since G'_d is quite sparse, hybrid sampling sacrifices some low-resolution samples d for dramatically reducing the number of RS measurements b.

An $N \times N$ image I can be represented as linear combinations of LR samples d on coarser scales and K'_d-sparsity G'_d associated with d, $I = \Psi' G'_d + \Psi'' d$. For the sake of simplicity, we approximate our TV_{ℓ_1} minimization by enforcing the sparsest G'_d, and reformulate Eq. (2.5) as follows:

$$\min_{G'_d} \|G'_d\|_1 \quad \text{s. t.} \quad A' G'_d = \Phi \Psi' G'_d = b - \Phi \Psi'' d, \tag{2.11}$$

where A' is the sampling matrix. The minimal number of measurements for the lossless reconstruction is $\alpha K'_d \log(N^2/K'_d)$, where α is a constant.

Proposition 1 *The hybrid sampling approach consisting $n \times n$ low-resolution sampling and M random projections is capable of recovering the original image (size $N \times N$), if the sampling matrix A' obeys UUP [30] for the unknown K'_d-sparsity coefficients G'_d at the finer levels of HGT. Consequently, for lossless reconstruction, the minimal number of measurements M_{min} equals $(N/n)^2 + \alpha K'_d \log((N^2 - (N/n)^2)/K'_d)$, where α is a constant.*

The optimal hybrid sampling depends on selection of the block size n in LRS and other parameters, such as d and K'_d. By varying LRS and its corresponding RS, we can seek the optimal hybrid sampling with the smallest number of measurements ($\hat{M}_{min} = (N/\hat{n})^2 + \alpha \hat{K}'_d \log((N^2 - (N/\hat{n})^2)/\hat{K}'_d)$), where $1/\hat{n}$ is the frequency of the optimal LRS.

2.3 Implementation Issues

2.3.1 Practical Hybrid Sampling

One problem with random sampling is its inefficiency for large-scale images. The notable CS application of random sampling is Single Pixel Camera (SPC) [27, 28], which is advantageous over the conventional pixel-array camera in reducing sampling rate (ratio of sample size and data size, denoted as R). It sequentially acquires random linear measurements of scene brightness by a digital micro-mirror (DMD) and thus its sensing rate is limited. To date, DMD can provide at most 32000 random patterns/second. Suppose we need to capture an image of size 1024×768 at $R = 10\%$, then the sensing process takes $1024 \times 768 \times 0.1/32000 = 2.46$ seconds. Our hybrid sampling can increase the frame rate (RS) by incorporating some LR samples and even reduce the total sampled data from RS and LR, for the same quality of reconstruction.

Another problem with random sampling is its high computational cost. For instance, to recover a 1024×768 image at $R = 10\%$, we need more than 7 gigabytes of memory just to store the Bernoulli random matrix. To reduce the cost of time and memory, many efforts have been made to develop structural sampling methods (Fourier transform [35], scrambled Fourier [38], Hadarmard transform [39], Noiselet [40, 26]). A typical application of structural

sampling is Magnetic Resonance Imaging (MRI) [35] using Fourier sampling.

2.3.2 Sparsity Decoding

In this section, we present our approach to recover the image from the limited measurements by decoding the sparse gradient G. There is a number of algorithms available for decoding, including Orthogonal Matching Pursuit (OMP) [41], Basis Pursuit(BP) [42] listed in SparseLab Toolbox [43], second-order cone programming (SOCP) implemented in ℓ_1-Magic [44], and iterative shrinkage/thresholding (IST) [36].

For decoding, we aim to solve Eq. (2.5) and recover the image I and its sparse partial gradients G. We employ a primal-dual interior-point optimization routine called PDCO [45]. Since random sampling is computationally costly, we need to replace it by Fourier sampling for sensing large-scale images. Given the partial Fourier data b, we use the IST method [36] to solve Eq. (2.5) to recover the image I.

2.4 Experimental Results

In this section, we present some experimental results to compare our hybrid compressive sampling using TV_{ℓ_1}, with the widely used $\mathrm{TV}_{\ell_1\ell_2}$ based CS method. We present results for both qualitative (visual) and quantitative evaluations.

2.4.1 Selection of Parameter γ

As shown in Eq. (2.7), our TV_{ℓ_1} seeks the γ-weighted gradient sparsity and recovers images with sharp edges. For a sharp image containing 40% diagonal edges, our TV_{ℓ_1} can achieve much higher accuracy than $\mathrm{TV}_{\ell_1\ell_2}$and its accuracy depends on selection of γ (Figure 2.4(a)). As shown in Figure 2.4(b), in comparison with other TV measure, our TV_{ℓ_1} ($\gamma = 1$) requires fewer samples at images containing many diagonal edges and more samples at images containing few diagonal edges, for the same recovery accuracy. That means, the value of the optimal γ should be proportional to the percentage of diagonal edges in the image. This result is consistent with the claim that our

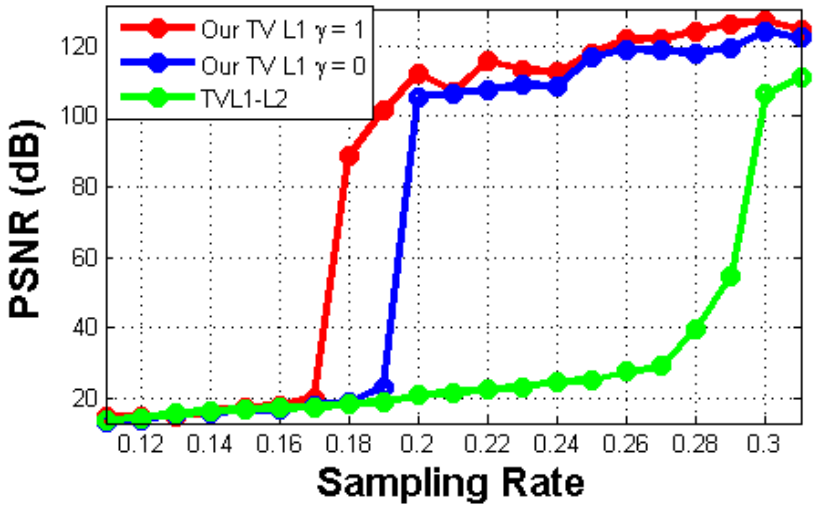

(a)

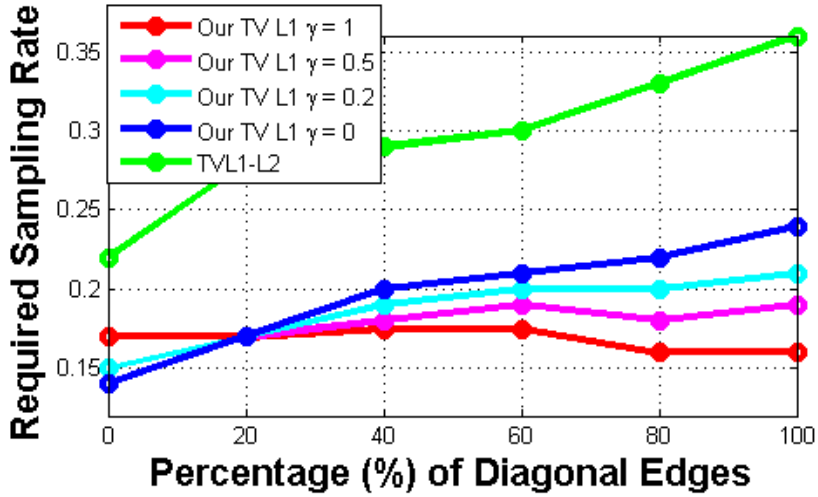

(b)

Figure 2.4: Comparison of TV measures. (a) The recovery accuracy of a sharp image in which 40% of edges are diagonal. (b) The required sampling rates on different images, for the recovery accuracy (PSNR) to be larger than 40 dB.

TV_{ℓ_1} can recovery all possible sharper edges (vertical, horizontal or diagonal) in Section 2.2.1. In our following experiments, the optimal γ is selected as $0.2 \leq \gamma \leq 1$.

2.4.2 Hybrid Compressive Sampling via Our TV_{ℓ_1}

To show the advantage of our TV_{ℓ_1} over $\text{TV}_{\ell_1\ell_2}$, we choose small piecewise smooth images, e.g., ECCV image in Figure 2.5 and the ball image in Figure 2.6, due to the expensive sparsity decoding. As shown in Figure 2.5, our TV_{ℓ_1} based CS is able to reconstruct the sharp ECCV image almost perfectly while $\text{TV}_{\ell_1\ell_2}$ causes serious artifacts at $R = 25\%$. Our TV_{ℓ_1} is still advantageous over previous $\text{TV}_{\ell_1\ell_2}$ at varying sampling rates (Figure 2.5(c)). As shown in Figure 2.6, the ball image is almost a real image, except that we remove some noise in the gray region. Given the same sampled data, our TV_{ℓ_1} acquires an image (Figure 2.6(b)) whose Peak-Signal-Noise-Ratio (PSNR) is 3.0 dB higher than that recovered by previous $\text{TV}_{\ell_1\ell_2}$ (Figure 2.6(a)).

For most natural images, low-resolution sampling (LRS) and random sampling (RS) can complement each other. For instance, the recovery accuracy of our TV_{ℓ_1} is improved by combining RS with LRS ($n = 3$) on the ball image (Figure 2.6). As shown in Figure 2.6 (d), both our TV_{ℓ_1} and previous $\text{TV}_{\ell_1\ell_2}$ achieve the optimal accuracy at the LRS ($n = 3$), given the total sampling rate $R = 60\%$.

Table 2.2: The estimated and real minimal number of required measurements on the ball image ($N = 32$), for each hybrid sampling methods associated with different LRS (block size: $n \times n$).

$n \times n$ LRS	K_1'	$Esti.M_{min}$ at $\alpha = 1.2$	$RealM_{min}$ for PSNR ≥ 40 dB
No LRS	576	$0 + 576\alpha = 691$	717
4×4	512	$64 + 512\alpha = 678$	680
3×3	440	$121 + 440\alpha = 649$	653
2×2	368	$256 + 368\alpha = 698$	665
2×1	250	$512 + 235\alpha = 794$	756

According to Proposition 1, we can determine the optimal hybrid sampling that requires the fewest samples M_{min}. Now, we want to verify Proposition 1 by some experimental results. Since K_1' is comparable to $N^2 - (N/n)^2$, we approximate the estimated M_{min} by $(N/n)^2 + \alpha K_1'$. Table 2.2 shows one

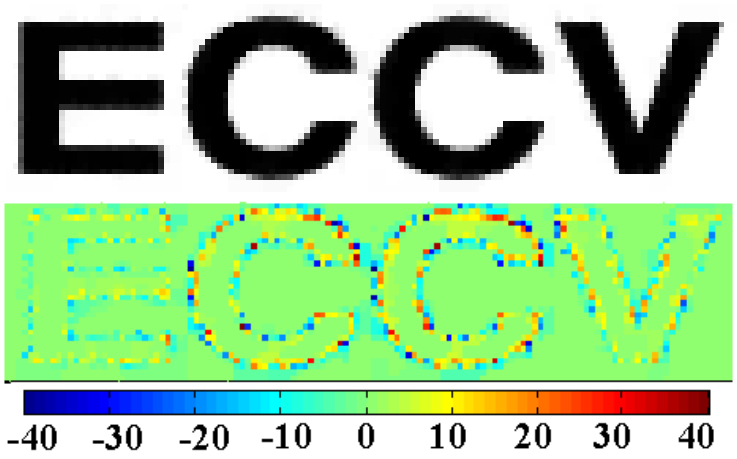

(a)

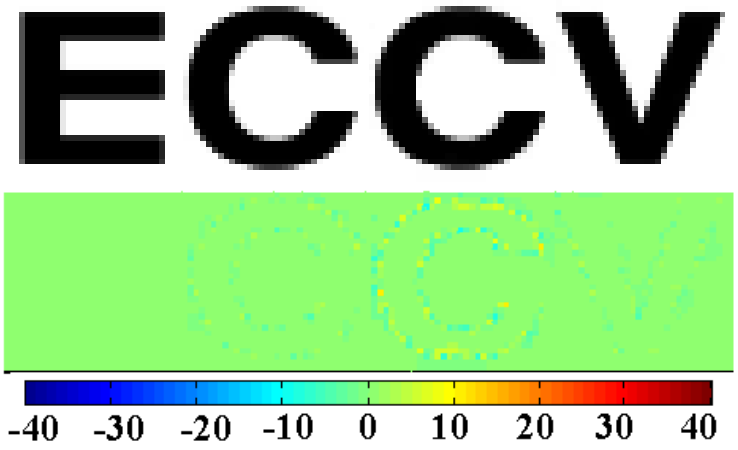

(b)

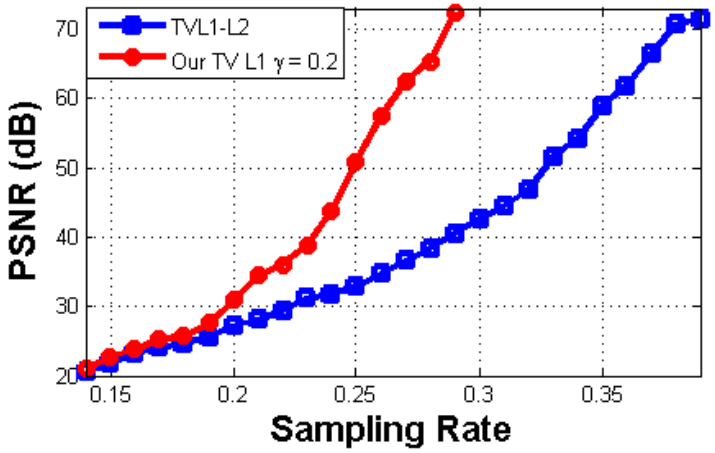

(c)

Figure 2.5: Recovered ECCV images (upper) and error maps (lower) by (a)$\mathrm{TV}_{\ell_1\ell_2}$ (PSNR = 32.88 dB) and (b) TV_{ℓ_1} (PSNR = 48.17 dB) at the sampling rate $R = 25\%$ (LRS:6.25% and RS:18.75%). (c) Comparison of TV measures on ECCV image sensed by our hybrid sampling with LRS ($F = 1/4$).

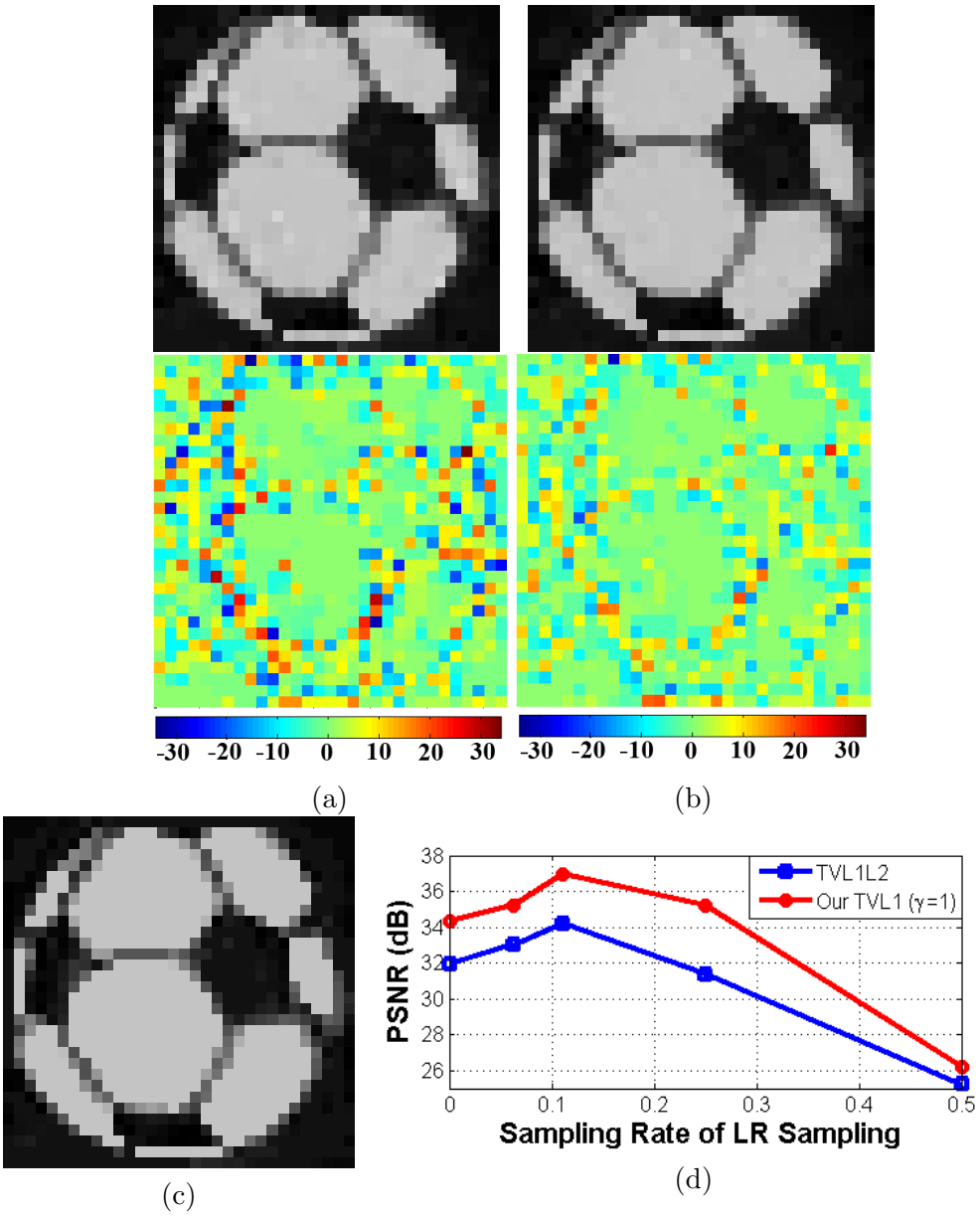

Figure 2.6: Ball images (with error maps) recovered by (a) $\mathrm{TV}_{\ell_1\ell_2}$ (PSNR = 29.8 dB) and (b) TV_{ℓ_1} (PSNR = 32.8 dB) at random sampling (41%) and LR sampling ($F = 1/3$). (c) Original ball image (size: 32×32). (d) Curve of recovery accuracy of TV_{ℓ_1} and $\mathrm{TV}_{\ell_1\ell_2}$ at varying LR sampling rates and fixed total hybrid and sampling rate ($R = 60\%$).

successful case ($\alpha = 1.2$), in which our estimated M_{min} is close to the real M_{min} required to achieve the accuracy (PSNR = 40dB). At $\alpha = 1.2$, hybrid sampling with LRS ($n = 3$) requires the smallest M_{min} and thus is optimal, which is consistent with the accuracy chart in Figure 2.6 (d).

2.4.3 Evaluation of our TV_{ℓ_1} by Fourier Sampling

Now, we evaluate our TV_{ℓ_1} based CS on two real MR images (chest and bone) by Fourier sampling ([35]). Given 14% Fourier samples, our TV_{ℓ_1} can recover the chest image I_1 (Figure 2.7(c)), whose PSNR is 1.3 dB higher than that I_2 (Figure 2.7(b)) by $TV_{\ell_1\ell_2}$. Figure 2.7(g) shows the difference map $I_d = I_1 - I_2$, which is close to the second derivatives of the chest image (Figure 2.7(a)). Similarly, the region boundary (Figure 2.7(f)) in the bone image recovered from our TV_{ℓ_1} is obviously sharper than that in Figure 2.7(e), which is also demostrated by their difference map (Figure 2.7(h)). Thus, our TV_{ℓ_1} is prone to enforcing sparse partial gradients in piecewise smooth images. Besides, our TV_{ℓ_1} achieves higher accuracy at varying sampling rates than $TV_{\ell_1\ell_2}$ in recovering these images, as shown in Figure 2.7(i).

2.5 Summary

In this chapter, we proposed a hybrid compressive sampling camera that combines the conventional random sampling and low-resolution sampling, which is shown to advantageous over the sole random sampling on natural images. In addition, we proposed a new TV measure TV_{ℓ_1}, which enforces the sparsity and the directional continuity in the partial gradient domain. We induce a UUP condition for TV based compressive sampling, which shows that our TV_{ℓ_1} requires fewer measurements than widely used $TV_{\ell_1\ell_2}$ for the same quality reconstruction. In addition, theoretical analysis is presented to show the advantage of hybrid sampling over random sampling for most natural images. Finally, our hybrid CS camera using TV_{ℓ_1} achieves better performance in experimental results.

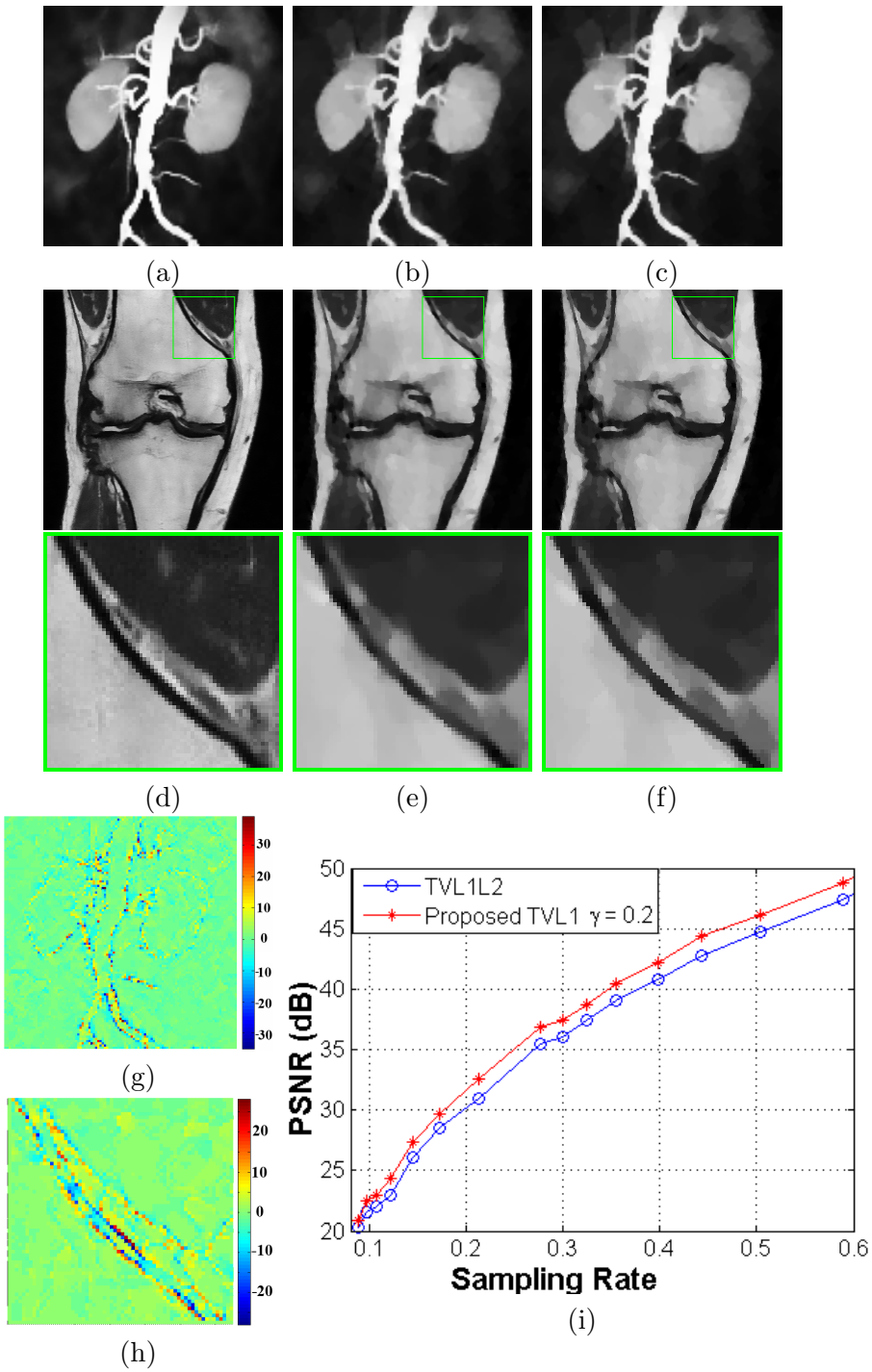

Figure 2.7: Comparison of TV measures by Fourier sampling. (a) Original chest image sensed at $R = 14\%$, images recovered by (b) $\mathrm{TV}_{\ell_1\ell_2}$ (PSNR = 26.0 dB) and (c) TV_{ℓ_1} (PSNR = 27.3 dB). (d) Original bone image sensed at $R = 9.34\%$, images recovered by (e) $\mathrm{TV}_{\ell_1\ell_2}$ (PSNR = 27.1 dB) and (f) TV_{ℓ_1} (PSNR = 27.6 dB). The difference map of TV_{ℓ_1} recovery and $\mathrm{TV}_{\ell_1\ell_2}$ recovery on (g) chest image and (h) bone image. (i) Varying accuracy with sampling rate on the chest image.

CHAPTER 3

THREE-DIMENSIONAL COMPRESSIVE SAMPLING (3DCS)

3.1 Introduction

Digital images and videos are being acquired by new imaging sensors with ever-increasing fidelity, resolution and frame rate. The theoretical foundation is the Nyquist sampling theorem, which states that the signal information is preserved if the underlying analog signal is uniformly sampled above the Nyquist rate, which is twice its highest analog frequency. Unfortunately, Nyquist sampling has two major shortcomings. First, acquisition of a high resolution image necessitates a large-sized sensor. This may be infeasible or extremely expensive in infrared imaging. Second, the raw data acquired by Nyquist sampling is too large to acquire, encode and transmit in short time, especially in the applications of wireless sensor networks, high speed imaging cameras, magnetic resonance imaging (MRI) and so forth.

Compressive sensing [23, 38] or compressive sampling (CS), was developed to solve this problem effectively. It is advantageous over Nyquist sampling, because it can (1) relax the computational burden during sensing and encoding, and (2) acquire high resolution data using small sensors. Assume a vectorized image or signal I of size L is sparsely represented as $I = \Psi z$, where z has K nonzero entries (called K-sparse) and Ψ is the wavelet transform. CS acquires a small number of incoherent linear projections $b = \Phi I$ and decodes the sparse solution $I = \Psi^T I$ as follows:

$$\min_I \quad \|\Psi^T I\|_0 \quad \text{s. t.} \quad \Phi I = b, \tag{3.1}$$

$$\text{or} \quad \min_z \quad \|z\|_0 \quad \text{s. t.} \quad Az = \Phi\Psi z = b, \tag{3.2}$$

where Φ is a random sampling (RS) ensemble or a circulant sampling ensemble. According to [30], CS is capable of recovering K-sparse signal z (with

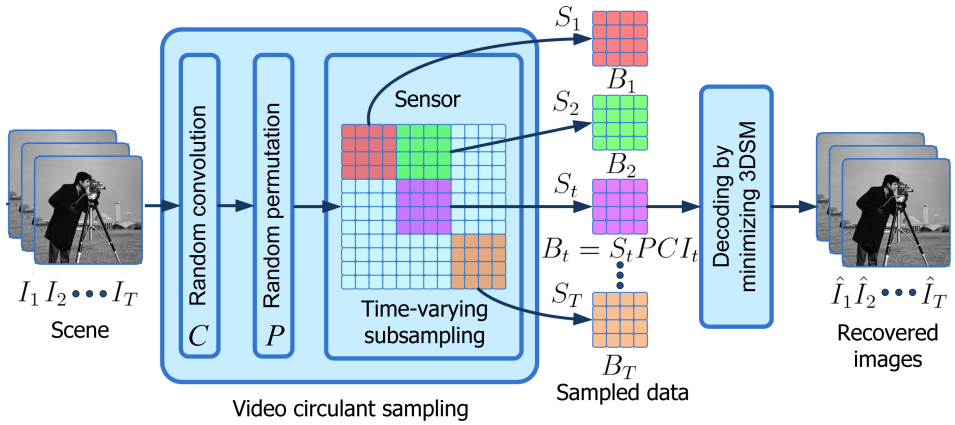

Figure 3.1: A compressive imaging (CI) camera using the proposed 3DCS. In this CI camera, a photographic lens (for forming image sequences, vectorized as $I_t, 1 \leq t \leq T$) is followed by video compressive sampling, which consists of optical random convolution (C), random permutation (P) and time-varying subsampling (S_t) on a sensor. From the sampled data sequences $B_t = S_t P C I_t, 1 \leq t \leq T$, the image sequences $\hat{I}_t, 1 \leq t \leq T$ is decoded by minimizing the 3DSM.

an overwhelming probability) from b of size M, provided that the number of random samples meets $M \geq \alpha K \log(L/K)$. The required sampling rate $\frac{M}{L}$, to incur lossless recovery, is roughly proportional to $\frac{K}{L}$. A compressive imaging camera prototype using RS is presented in [28]. Recently, circulant sampling (CirS) [46]) was introduced to replace RS with the advantages of easy hardware implementation, memory efficiency and fast decoding. It has been shown that CirS is competitive with RS in terms of recovery accuracy [46].

CS often reduces the required sampling rate by seeking the sparsest representation or by exploring some prior knowledge of the signal. Image CS (called 2DCS) decodes each image independently by minimizing both its sparsity in wavelet domain and total variation (TV2D+2DWT) [35, 34]. However, due to the significant sparsity, the required sampling rate is still quite high. Video CS (called 3DCS) is introduced to further reduce the sampling rate by adding the temporal correlation. Adaptive methods sense a key frame by Nyquist sampling and then sense consecutive frames [47] or frame differences [48] by CS. Sequential methods first decode a key frame and then recover other frames based on motion estimation [49]. Joint methods recover a video by seeking its 3D wavelet sparsity (3DWT) [50], or by minimizing the wavelet sparsity of its first frame and subsequent frame differences (Bk and Ck) [51].

However, none of the existing methods has exploited the major features of videos, i.e. 3D piecewise smoothness and temporal low-rank property.

In this chapter, a new 3DCS approach is proposed to facilitate a promising CI camera (Figure 3.1) requiring a very low sampling rate. Without any computational cost, this CI camera acquires the compressed data $B_t, 1 \leq t \leq T$, from which a video clip is recovered by minimizing a new 3D sparsity measure (3DSM). This 3DSM is motivated by two characteristics of videos. First, videos are often piecewise smooth in the 2D image domain and temporal domain. Second, image sequences in a video are highly correlated along the temporal axis, which can be modeled as a temporal low-rank matrix [52] with sparse innovations. Thus, a new 3DSM is constructed by combining 3D total variation (TV3D) and the low-rank measure in the Ψ-transform domain (Psi3D). The contributions of this chapter are as follows:

1. A generic 3D sparsity measure (3DSM) is proposed, which exploits the 3D piecewise smoothness and temporal low-rank property in video CS. Extensive experiments demonstrate (1) the superiority of our 3DSM over other measures in terms of much higher recovery accuracy and (2) robustness over small camera motion.

2. An efficient algorithm is developed for the 3DSM with guaranteed convergence, which enables the recovery of large-scale videos.

3. A 3DCS camera using video circulant sampling (CirS) is presented (Figure 3.1) and a random lens is proposed to simplify the conventional implementation of circulant sampling, i.e. Fourier optics.

This chapter is organized as follows. Section 3.2 presents the proposed 3DSM and video CirS. Section 3.3 develops the recovery algorithm for the 3DSM. Section 3.4 describes the experiments in comparison with existing methods. Section 3.5 gives the concluding remarks.

3.2 Proposed Method

3.2.1 Overview of Our 3D Sparsity Measure (3DSM)

In this section, a 3D sparsity measure (3DSM) is given for a fixed CI camera and will be extended to a moving camera later. A video clip is represented as a matrix $\mathbf{I} = [I_1, ..., I_t, ..., I_T]$, where each column I_t denotes one frame. For computational convenience, $\mathbf{I}$ is often vectorized as $I = [I_1; I_2; ...; I_T]$. A 3D sparsity measure (3DSM) is built by combining two complementary measures—3D total variation (TV3D) and 3D Ψ-transform sparsity (Psi3D). TV3D keeps the piecewise smoothness, while Psi3D retains the image sharpness and enforces the temporal low-rank property. As shown in Figure 3.1, the video I is recovered from the sampled data B by minimizing 3DSM.

$$\min_I \text{TV3D}(I) + \lambda \text{Psi3D}(I) \quad \text{s. t.} \quad \overline{\Phi} I = B, \tag{3.3}$$

where λ is a tuning parameter, $\overline{\Phi} = \text{diag}(\Phi_1, \Phi_2, ..., \Phi_T)$ is the video circulant sampling matrix, and $B = [B_1; B_2; ...; B_T]$ is the sampled data.

3.2.2 3D Total Variation

In this section, TV3D is presented in detail. In 2DCS, total variation (TV) is often used to recover an image from incomplete measurements, by exploiting its piecewise smoothness in the spatial domain. The widely used form of TV is TVL1L2 [35, 24, 34, 36], denoted as $\text{TV}_{\ell_1\ell_2}(I_t) = \sum_i \sqrt{(D_1 I_t)_i^2 + (D_2 I_t)_i^2}$. In [53], the ℓ_1-norm based TV measure $\text{TV}_{\ell_1}(I_t) = \|D_1 I_t\|_1 + \|D_2 I_t\|_1$ is proven to be better than $\text{TV}_{\ell_1\ell_2}$ in reducing the sampling rate. By extending TV_{ℓ_1} to the three-dimensional (spatial and temporal) domain, a new measure TV3D is formulated as:

$$\text{TV3D}(I) = \|D_1 I\|_1 + \|D_2 I\|_1 + \rho \|D_3 I\|_1, \tag{3.4}$$

where (D_1, D_2, D_3) are finite difference operators in the 3D domain and ρ is proportional to the temporal correlation.

3.2.3 3D Sparsity Measure in Ψ-Transform Domain

In a video captured by a fixed camera, most pixels correspond to static scene and almost keep constant value over time. This video is temporally correlated and sparsely innovated (a small number of pixels varies with time), the same as its Ψ-transform coefficients $\mathbf{Z} = [Z_1, ..., Z_T] = [\Psi^T I_1, ..., \Psi^T I_T]$. Motivated by robust principal component analysis (RPCA) [54], $\mathbf{Z}$ is modeled as the sum of a low-rank (LR) matrix $\overline{\mathbf{Z}}$ and sparse innovation $\widehat{\mathbf{Z}}$. Thus, Psi3D is formulated as follows:

$$\text{Psi3D}(I) = \min_{\overline{Z},\widehat{Z}} \mu \text{Rank}(\overline{\mathbf{Z}}) + \eta \|\overline{Z}\|_1 + \|\widehat{Z}\|_1 \quad \text{s. t.} \quad \overline{\Psi}^T I = \overline{Z} + \widehat{Z}, \quad (3.5)$$

where $\overline{\Psi} = \text{diag}(\Psi, ..., \Psi)$, $\overline{Z} = [\overline{Z}_1; ...; \overline{Z}_T]$ and $\widehat{Z} = [\widehat{Z}_1; ...; \widehat{Z}_T]$ are vectorized versions of $\overline{\mathbf{Z}}$ and $\widehat{\mathbf{Z}}$. The weight coefficient μ tunes the rank of $\overline{\mathbf{Z}}$ and η must be set as $\eta \leq 1$; otherwise, the optimal $\overline{\mathbf{Z}}$ is prone to vanish. Different from the RPCA which seeks $\overline{Z}$ and $\widehat{Z}$ from complete data I, our 3DCS needs to recover $\overline{Z}$ and $\widehat{Z}$ from incomplete projections $B = \overline{\Phi} I$. Thus, both the sparsity and rank of $\overline{\mathbf{Z}}$ are explored to decode I. The proposed Psi3D attempts to minimize the number of nonzero singular values of $\overline{\mathbf{Z}}$, which is NP-hard and no efficient solution is known [55]. In practice, the widely used alternative [56, 54] is the *nuclear norm* $\|\overline{\mathbf{Z}}\|_* = \sum_{k=1} \sigma_k(\overline{\mathbf{Z}})$, which equals the sum of the singular values. Thus, the Psi3D is approximated as:

$$\begin{aligned} \text{Psi3D}_1(I) = \min_{\overline{Z},\widehat{Z}} \mu \|\overline{\mathbf{Z}}\|_* + \eta \|\overline{Z}\|_1 + \|\widehat{Z}\|_1 \\ \text{s. t. } \overline{\Psi}^T I = \overline{Z} + \widehat{Z}. \end{aligned} \quad (3.6)$$

By assuming constant background, i.e., $\text{Rank}(\overline{\mathbf{Z}}) = 1$ and $\overline{Z} = [\overline{Z}_c, ..., \overline{Z}_c]$, the Psi3D is simplified by deleting the rank term as follows:

$$\text{Psi3D}_2(I) = \eta T \|\overline{Z}_c\|_1 + \|\widehat{Z}\|_1 \text{ s. t. } \Psi^T I_t = \overline{Z}_c + \widehat{Z}_t, \forall t. \quad (3.7)$$

By setting $\eta T = 1$, the simplified Psi3D_2 is similar to the joint sparsity model of multiple signals [57]. In the case of constant background, Psi3D_2 requires less tuning parameters and computational cost than Psi3D_1. However, it is expected that Psi3D_1 achieves higher recovery accuracy than Psi3D_2 in the case of time-varying background ($\text{Rank}(\overline{\mathbf{Z}}) > 1$), e.g., illumination

changes.

3.2.4 Robustness over Camera Motion

In this section, the 3DSM in Eq. (3.3) will be modified to be robust to camera motion. The 3DSM proposed in Eq. (3.3) explores the piecewise smoothness and the low-rank property, which is quite effective in improving the recovery accuracy of 3DCS. However, this model assumes a fixed camera or low-texture background. Even small camera motion might cause misalignments among real image sequences $I = [I_1; ...; I_T]$ and increase the temporal rank dramatically. These misalignments of I are modeled as a group of transformations (affine or perspective) $\Omega = \{\Omega_1, ..., \Omega_T\}$ on well-aligned image sequences $\tilde{I} = [\tilde{I}_1; ...; \tilde{I}_T]$ captured by a fixed camera. Specifically, $I_t = \tilde{I}_t \circ \Omega_t, 1 \leq t \leq T$. By introducing a group of transformations Ω, the 3DSM is extended to the moving camera as follows:

$$\min_{I,\Omega} \mathrm{TV3D}(\tilde{I}) + \lambda \mathrm{Psi3D}(\tilde{I}) \quad \text{s. t. } \overline{\Phi} I = B, \;\; I_t = \tilde{I}_t \circ \Omega_t. \tag{3.8}$$

3.2.5 Video Circulant Sampling

Circulant sampling (CirS) [46], also called random convolution [58], was introduced to replace random sampling (RS). CirS is advantageous over RS, in terms of friendliness in hardware implementation, memory efficiency and fast decoding. In addition, CirS has been shown to be as effective as RS in reducing the sampling rate ($\frac{M}{L}$) [46].

In this section, we present a video circulant sampling (CirS) method, which, together with decoding using 3DSM, constitutes a compressive imaging camera using 3DCS (Figure 3.1). This video CirS consists of two steps:

1. Random convolution. Video CirS convolves an image I_t by a random kernel H, denoted by CI_t, where C is a circulant matrix with H as its first column. C is diagonalized as $C = \mathcal{F}^{-1}\mathrm{diag}(\widehat{H})\mathcal{F}$, where $\widehat{H}$ is the Fourier transform of H, denoted by $\widehat{H} = \mathcal{F}H$.

2. Random subsampling, which consists of random permutation (P) and time-varying subsampling (S_t). S_t selects a block of M pixels from all

N pixels on PCI_t and obtains the data $B_t = S_t PCI_t \triangleq \Phi_t I_t$. Note that the selected block drifts with time t (Figure 3.1). To relax the burden of both sensing and encoding, it is desirable to implement a physical mapping from a random subset to a 2D array (sensor). Although it might be challenging, a possible solution is to implement random permutation by a bundle of optical fibers, followed by a moving small sensor. The easy way—sensing the whole image CI_t by a big sensor and throwing away the unwanted $N - M$ pixels, does not benefit sensing but yields a method of computation-free encoding.

3.2.6 A Random Lens for Random Convolution

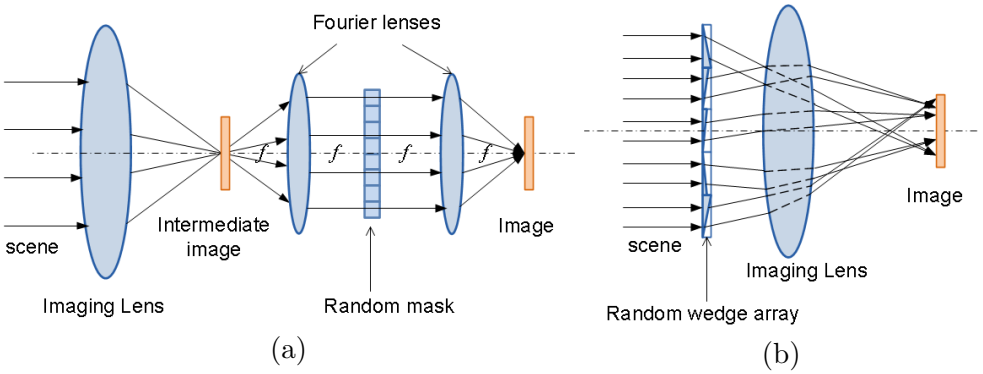

Figure 3.2: (a) The conventional method of implementing random convolution: placing a 4F correlator [58] behind the imaging lens. (b) The proposed random lens for random convolution, which consists of a random wedge array and a imaging lens. The random wedge array can deviate the incoming light from one direction to multiple random directions. The image formed behind the imaging lens is equivalent to the convolution of the outside scene with a random kernel.

As presented in [58], circulant sampling (or random convolution) is much more efficient than random sampling in both sensing and image decoding processes. In convention, we can implement circulant sampling by mounting a 4F correlator (with a random mask) [58] behind the imaging lens, as shown in Figure 3.2. However, this 4F correlator is quite complicated and bulky. In this chapter, we propose to develop another simpler physical implementation of random convolution, i.e., a random lens, which consists of a imaging lens and a random wedge array. As shown in Figure 3.2, the incoming parallel

light arriving at the random wedge array is deflected to multiple random directions and converged by the lens onto a random point on the sensor. Contrary to the conventional lens, the light emanating from a far object point will be directed to multiple random image points. Thus, the image formed by our random lens is equivalent to the convolution of the outside scene by a random kernel, which is desirable in compressive sensing. Compared with other simple implementation of random convolutoin, e.g., random pinhole array [59] and random mirror array [60], our random lens has higher light-gathering power and higher imaging quality, due to the imaging lens.

3.3 3DCS Recovery Algorithms

3.3.1 Brief Introduction to Several Convex Optimization Methods

Before presenting our efficient 3DCS recovery algorithm, we give a brief introduction to several convex optimization methods, including the dual ascent method, augmented Lagrangian method (ALM) and augmented Lagrangian method-alternating direction method (ALM-ADM). Our introduction is just a shorter version of the review in [61] and thus we refer readers to [61] for details. Let us consider a single equality constrained convex optimization problem,

$$\min_x f(x) \quad \text{s. t.} \quad Ax = b, \tag{3.9}$$

with variable $x \in \mathbb{R}^n$, where $A \in \mathbb{R}^{m \times n}$ and $f : \mathbb{R}^n \to \mathbb{R}$.

The Lagrangian function for the original problem in Eq. (3.9) is

$$\mathcal{L}(x, y) = f(x) + y^T(Ax - b), \tag{3.10}$$

where $y \in \mathbb{R}^m$ is the Lagrange multiplier or dual variable and the corresponding dual problem is

$$g(y) = \inf_x \mathcal{L}(x, y) = \inf_x f(x) + y^T(Ax - b). \tag{3.11}$$

Assuming the objective function f is strictly convex, the dual ascent method [61] solves this equality constrained problem by two steps: (1) an

x-minimization step and (2) dual update of y by gradient ascent.

$$\begin{aligned} x^{k+1} &= \arg\min_x \mathcal{L}(x, y^k) \\ y^{k+1} &= y^k + \alpha^k (Ax^{k+1} - b), \end{aligned} \tag{3.12}$$

where α^k is the step size at the k^{th} iteration.

The augmented Lagrangian method (ALM), also called the method of multipliers [61], was developed to improve the convergence of the dual ascent method without the assumption—strict convexity of f. The augmented Lagrangian function for the original problem in Eq. (3.9) is

$$\mathcal{L}_\beta(x, y) = f(x) + y^T(Ax - b) + \frac{\beta}{2}\|Ax - b\|_2^2, \tag{3.13}$$

where $\beta > 0$ a penalty parameter. The advantage of ALM is that the dual function $g_\beta(y) = \inf_x \mathcal{L}_\beta(x, y)$ can be shown to be differentiable under rather mild conditions on the original problem in Eq. (3.9). Thus, the ALM algorithm is listed as follows

$$\begin{aligned} x^{k+1} &= \arg\min_x \mathcal{L}_\beta(x, y^k) \\ y^{k+1} &= y^k + \beta(Ax^{k+1} - b). \end{aligned} \tag{3.14}$$

The major differences of ALM from the standard dual ascent are that (1) ALM minimizes the augmented Lagrangian function and (2) it uses the penalty parameter β as the step size α^k. It is well motivated to choose the particular step size β in the dual update of Eq. (3.14). The optimality conditions for the original problem in Eq. (3.9) are the primal and dual feasibility, which are respectively listed as follows:

$$Ax^* = b, \qquad \nabla f(x^*) + A^T y^* = 0. \tag{3.15}$$

In the first step of the ALM algorithm (Eq. (3.14)), the optimality condition for x^{k+1} is

$$0 = \nabla_x \mathcal{L}_\beta(x, y^k) = \nabla f(x^{k+1}) + A^T(y^k + \beta(Ax^{k+1} - b)). \tag{3.16}$$

By setting β as the step size in the dual update of ALM, the update (x^{k+1}, y^{k+1})

at each iteration is dual feasible, i.e.,

$$0 = \nabla f(x^{k+1}) + A^T(y^{k+1}). \tag{3.17}$$

As the ALM algorithm proceeds, the primal residual $Ax^* - b$ converges to zero, yielding the primal feasibility.

Despite the great improvement of convergence over dual ascent, ALM also brings a cost—non-decomposability of the augmented Lagrangian function. Suppose the objective function $f(x)$ can be separated as $f_1(x_1) + f_1(x_1)$, the equality constrained convex optimization problem can be written as follows:

$$\min_{x_1,x_2} f_1(x_1) + f_2(x_2) \quad \text{s. t.} \quad Ax_1 + Bx_2 = c. \tag{3.18}$$

The augmented Lagrangian function $\mathcal{L}_\beta(x_1, x_2, y) = f_1(x_1)+f_2(x_2)+y^T(Ax_1+Bx_2-c)+\frac{\beta}{2}\|Ax_1+Bx_2-c\|_2^2$ becomes not separable. Thus, the x-minimization step in ALM cannot be carried out separately with respect to x_1 and x_2, and the joint minimization of x is often much more computationally costly.

The augmented Lagrangian multiplier-alternating direction method (ALM-ADM), also called the alternating direction method of multipliers (ADMM) [61], is intended to improve the decomposability of ALM. Different from ALM that jointly minimizes $L_\beta(x, y)$ with respect to $x = [x_1, x_2]$, ALM-ADM sequentially minimizes it over x_1 and x_2 in an alternating fashion as follows:

$$\begin{aligned} x_1^{k+1} &= \arg\min_{x_1} \mathcal{L}_\beta(x_1, x_2^k, y^k) \\ x_2^{k+1} &= \arg\min_{x_2} \mathcal{L}_\beta(x_1^{k+1}, x_2, y^k) \\ y^{k+1} &= y^k + \beta(Ax_1^{k+1} + Bx_2^{k+1} - c). \end{aligned} \tag{3.19}$$

By assuming the objective $f(x)$ can be separated as two parts $f_1(x_1)$ and $f_2(x_2)$, ALM-ADM is shown to converge under some mild conditions in the literature [61, 36].

3.3.2 3DCS Recovery Using Inexact ALM-ADM

In this section, an efficient algorithm is presented to solve the 3DSM for a fixed camera. By introducing weight parameters $\alpha_1 = \alpha_2 = 1, \alpha_3 = \rho$, and auxiliary parameters $\chi \triangleq (G_i, \overline{Z}, \widehat{Z}, R)$, our 3DCS using Psi3D$_1$ Eq. (3.3) can

be rewritten as:

$$\min_{I,G_i,\overline{Z},\widehat{Z}} \quad \sum_{i=1}^{3} \alpha_i \|G_i\|_1 + \lambda(\mu\|\overline{\mathbf{Z}}\|_* + \eta\|\overline{Z}\|_1 + \|\widehat{Z}\|_1)$$
$$\text{s. t. } G_i = D_i I, \ \overline{Z} + \widehat{Z} = \overline{\Psi}^T I, \ R_t = C I_t, \ S_t P R_t = B_t. \tag{3.20}$$

This equality constrained problem can be solved by augmented Lagrangian multipliers (ALM) [36]. Given an L1-norm problem $\min \|a\|_1 \quad \text{s. t.} \quad a = b$, its augmented Lagrangian function (ALF) is defined as $\mathcal{L}_\beta(a, b, y) = \|a\|_1 - y(a-b) + \frac{\beta}{2}\|a-b\|_2^2$. Suppose the Lagrangian multipliers is denoted as $\rho \triangleq (b_1, b_2, b_3, d, g)$, the ALF of Eq. (3.20) is written as

$$\begin{aligned}\mathcal{L}(I, \chi, \rho) = &\sum_{i=1}^{3} \alpha_i \mathcal{L}_{\beta_i}(G_i, D_i I, b_i) + \lambda(\mu\|\overline{\mathbf{Z}}\|_* + \eta\|\overline{Z}\|_1 + \|\widehat{Z}\|_1 \\ &+ \frac{\beta_4}{2}\|\overline{Z} + \widehat{Z} - \overline{\Psi}^T I - \frac{d}{\beta_4}\|_2^2) + \frac{\beta_5}{2}\|R - \overline{C} I - \frac{g}{\beta_5}\|_2^2 \\ &\text{s. t.} \quad S_t P R_t = B_t, 1 \le t \le T, \end{aligned} \tag{3.21}$$

where $\beta_i, 1 \le i \le 5$ are over-regularization parameters and $\overline{C} = \text{diag}(C, ..., C)$. ALM solves Eq. (3.20) by iterating between the following two steps:

1. Solve $(I^{k+1}, \chi^{k+1}) \leftarrow \arg\min \mathcal{L}(I, \chi, \rho^k)$.
2. Update ρ^{k+1} with $(\rho^k, I^{k+1}, \chi^{k+1})$.

Each ALM iteration requires an exact minimization of $\mathcal{L}(I, G_i, \overline{Z}, \widehat{Z}, R)$, which is expensive. Fortunately, at fixed I and ρ^k, minimization of $\mathcal{L}(G_i, \overline{Z}, \widehat{Z}, R)$ can be performed independently. In this case, all the variables can be divided into two groups (I and $\chi = \{G_i, \overline{Z}, \widehat{Z}, R\}$), and $\mathcal{L}(I^k, \chi)$ can be minimized by applying the alternating direction method (ADM) [36]. Given ρ^{k+1} is updated at a sufficiently slow rate, the exact minimization can be simplified as only one round of alternating minimization (called inexact ADM). As shown in Algorithm refalg1, the inexact ALM-ADM solves our 3DCS by iterating among three major steps: (1) separate rectification of χ, (2) joint reconstruction of I and (3) update of ρ.

As shown in Algorithm refalg1, we scale the conventional step size by a constant τ for better convergence [62]. Given the exact solution to $\arg\min_\chi \mathcal{L}(I^k, \chi, \rho^k)$ is reached in the first step, the group of components χ is equivalent to a single variable and the inexact ALM-ADM with respect to two variables χ and

Algorithm 1 Solving 3DCS using inexact ALM-ADM

Require: C, $\widehat{H}$, P, S_t and $B_t, 1 \leq t \leq T$
Ensure: I^{k+1}
1: $I^0 \leftarrow G_i^0 \leftarrow b_i^0 \leftarrow \text{zeros}(m, n, T), 1 \leq i \leq 3;$
$\overline{Z}^0 \leftarrow \widehat{Z}^0 \leftarrow d^0 \leftarrow R^0 \leftarrow g^0 \leftarrow \text{zeros}(m, n, T).$
2: **while** I not converged **do**
3: Separate Rectification of: $\chi = \{G_i, \overline{Z}, \widehat{Z}, R\}$:
$\chi^{k+1} \leftarrow \arg\min_\chi \mathcal{L}(I^k, \chi, \rho^k)$.
4: Joint Reconstruction:
$(I^{k+1}) \leftarrow \arg\min \mathcal{L}(I, \chi^{k+1}, \rho^k)$.
5: Update ρ by "Adding back noise":
$b_i^{k+1} \leftarrow b_i^k - \tau\beta_i(G_i^{k+1} - D_i I^{k+1})$,
$d^{k+1} \leftarrow d^k - \tau\beta_4(Z^{k+1} - \overline{\Psi}^T I^{k+1})$,
$g^{k+1} \leftarrow g^k - \tau\beta_5(R^{k+1} - \overline{C} I^{k+1})$.
6: $k \leftarrow k + 1$
7: **end while**

I is guaranteed with convergence. Motivated by the convergence analysis in [62], the convergence condition of our recovery algorithm using inexact ALM-ADM is given as follows.

Theorem 1 *If the over-regularization parameters $\beta_i > 0, \forall 1 \leq i \leq 5$ and the step length $\tau \in (0, (1 + \sqrt{5})/2)$, the video sequence I^{k+1} reconstructed by the inexact ALM-ADM (Algorithm 1) will uniquely converge the solution to Eq. (3.20).*

Separate Rectification Using Soft Shrinkage The convergence of the inexact ALM-ADM requires an exact solution to $\arg\min_\chi \mathcal{L}(I^k, \chi, \rho^k)$ at each iteration, which can be obtained separately with respect to G_i, R and the pair $\{\overline{Z}, \widehat{Z}\}$. Define a soft shrinkage function as $S(X, 1/\beta) = \max\{\text{abs}(X) - 1/\beta, 0\} \cdot \text{sgn}(X)$, where "$\cdot$" denotes elementwise multiplication, then $G_i^{k+1}, 1 \leq i \leq 3$ are straightforwardly updated by

$$G_i^{k+1} \leftarrow S(D_i I^k + \frac{b_i^k}{\beta_i}, \frac{1}{\beta_i}). \tag{3.22}$$

As for Psi3D$_1$, $\{\overline{Z}, \widehat{Z}\}$ are rectified from I^k and d^k by singular value shrinkage (SVS)[63]. To meet the convergence condition in Theorem 1, the pair $\{\overline{Z}, \widehat{Z}\}$ need to be rectified iteratively until the pair is converged. In practice,

the algorithm can be accelerated by just applying one round of rectification.

$$\overline{\mathbf{Z}}^{k+1} \leftarrow US(\Sigma, \mu/\beta_4)V^T \tag{3.23}$$

$$\overline{Z}^{k+1} \leftarrow S(\overline{Z}^{k+1}, \eta/\beta_4) \tag{3.24}$$

$$\widehat{Z}^{k+1} \leftarrow S(\overline{\Psi}^T I^k + \frac{d^k}{\beta_4} - \overline{Z}^{k+1}, \frac{1}{\beta_4}), \tag{3.25}$$

where $[U, \Sigma, V] = \text{svd}(\overline{\Psi}^T I^k + \frac{d^k}{\beta_4} - \widehat{Z}^k)$. Similarly, as for Psi3D$_2$, $\{\overline{Z}, \widehat{Z}\}$ can be rectified without SVS operation.

The complete circulant samples $R = [R_1; ...; R_T]$ are rectified by 3D data I^k and partial circulant samples B_t.

$$R_t^{k+1} \leftarrow CI_t^k \tag{3.26}$$

$$R_t^{k+1}(\text{Picks}_t, :) \leftarrow B_t, \tag{3.27}$$

where Picks_t are the indices of rows selected by S_t.

Efficient Joint Reconstruction Using 3D FFT

In this section, an efficient algorithm is presented to recover I^{k+1} jointly from rectified variables $(G_i^{k+1}, \overline{Z}^{k+1}, \widehat{Z}^{k+1}, R^{k+1})$. This algorithm is greatly accelerated by our 3DSM and video circulant sampling. By setting the derivative of $\mathcal{L}$ with respect to I to be zero, the optimal condition of I is induced as follows:

$$\sum_{i=1}^{3} \alpha_i \beta_i D_i^T (G_i - D_i I - \frac{b_i}{\beta_i}) + \lambda \beta_4 \overline{\Psi}(\overline{Z} + \widehat{Z} - \overline{\Psi}^T I - \frac{d}{\beta_4}) + \beta_5 \overline{C}^T (R - \overline{C} I - \frac{g}{\beta_5}) = 0. \tag{3.28}$$

Eq. (3.28) is reformulated into the form $\Gamma I = \Theta$, where $\Gamma = \sum_{i=1}^{3} \alpha_i \beta_i D_i^T D_i + \lambda \beta_4 + \beta_5 \overline{C}^T \overline{C}$. Under the periodic boundary condition [64] of finite operators $D_i, 1 \le i \le 3$, both $\overline{C}^T \overline{C}$ and $D_i^T D_i, 1 \le i \le 3$ are block-circulant matrices. The operation Γ on 3D data I is equivalent to the sum of separate convolutions with five point spread functions $\text{PSF}_i, 1 \le i \le 5$, which are given as

follows:

$$\begin{aligned}
\text{Horizontal: } \mathrm{PSF}_1 &= \alpha_1\beta_1[1;-2;1], && (3.29)\\
\text{Vertical: } \mathrm{PSF}_2 &= \alpha_2\beta_2[1,-2,1], && (3.30)\\
\text{Temporal: } \mathrm{PSF}_3 &= \alpha_3\beta_3[1:-2:1], && (3.31)\\
\text{Dirac delta: } \mathrm{PSF}_4 &= \alpha_4\beta_4\delta(x,y), && (3.32)\\
\text{2D: } \mathrm{PSF}_5 &= \beta_5\mathcal{F}^{-1}(\hat{H}^*\cdot\hat{H}), && (3.33)
\end{aligned}$$

where $[A_1 : A_2 : A_3]$ denotes concatenating A_1, A_2 and A_3 along the third (temporal) axis and $\hat{H}^*$ is the complex conjugate of $\hat{H}$. According to the convolution theory, this optimal condition with respect to I can be solved efficiently by applying 3D fast Fourier transform.

$$\sum_{i=1}^{5}\mathcal{F}(\mathrm{PSF}_i)\cdot\mathcal{F}(I)=\mathcal{F}(\Theta), \tag{3.34}$$

Given χ^{k+1} and ρ^k, Θ^{k+1} can be updated as follows:

$$\begin{aligned}
\Theta^{k+1} &= \sum_{i=1}^{3}\alpha_i\beta_i D_i^T(G_i^{k+1}-b_i^k)+\lambda\beta_4\overline{\Psi}(\overline{Z}^{k+1}+\widehat{Z}^{k+1}-d^k)\\
&\quad +\beta_5\overline{C}^T(R^{k+1}-g^k). && (3.35)
\end{aligned}$$

Then, I^{k+1} is recovered by three steps: (1) fast Fourier transform (FFT) on $\sum_{i=1}^{5}\mathrm{PSF}_i$ and Θ^{k+1}, (2) applying element-wise division to obtain $\mathcal{F}(I)$ and (3) inverse fast Fourier transform (IFFT). Our decoding algorithm is extremely efficient, for its joint reconstruction only requires several times FFT and some simple filterings.

3.3.3 3DCS Recovery with Camera Motion

In this section, the inexact ALM-ADM in Eq. (3.20) can be adapted to solve Eq. (3.8) for the moving camera. The objective function can be relaxed as

$\mathbf{F}(I, \Omega)$ as:

$$\mathbf{F}(I, \Omega) = \sum_{i=1}^{3} \alpha_i \|G_i\|_1 + \lambda(\mu\|\overline{\mathbf{Z}}\|_* + \eta\|\overline{Z}\|_1 + \|\widehat{Z}\|_1)$$
$$\text{s. t. } G_i = D_i(I \circ \Omega^{-1}),\ \overline{Z} + \widehat{Z} = \overline{\Psi}^T(I \circ \Omega^{-1}),\ S_t P C I_t = B_t. \tag{3.36}$$

The main difficulty in solving Eq. (3.36) is the complicated dependence of aligned images $\tilde{I}_t = I_t\Omega_t$ on unknown transformations $\Omega_t, 1 \leq t \leq T$. It is almost impossible to solve $\tilde{I}_t$ and Ω_t simultaneously. The ADM is applied to solve them by iterating between the following two steps:

1. Given Ω^k, solve $I^{k+1} \leftarrow \min_I \mathbf{F}(I, \Omega^k)$. This can be solved by adding forward and backward transformations in each iteration cycle of inexact ALM-ADM (Algorithm 1), however, it might be time-consuming. To accelerate it, the misalignments Ω_t are modeled as translation $(\Delta x_t, \Delta y_t)$. According to Fourier shift theorem, $\mathcal{F}(I_t)$ is equal to multiplying $\mathcal{F}(\tilde{I}_t)$ by a linear phase $P(\Delta x_t, \Delta y_t)$. It is induced that $CI_t = \mathcal{F}^{-1}(\hat{H} \cdot \mathcal{F}(I_t)) = \mathcal{F}^{-1}(\hat{H} \cdot P(\Delta x_t, \Delta y_t) \cdot \mathcal{F}(\tilde{I}_t)) = \tilde{C}_t\tilde{I}_t$, where $\tilde{C}_t = \mathcal{F}^{-1}(\hat{H} \cdot P(\Delta x_t, \Delta y_t))$. Thus, I is recovered by fast solving $\tilde{I}$, followed by circulant shift $(\Delta x_t, \Delta y_t)$.

$$\min_{\tilde{I}} \sum_{i=1}^{3} \alpha_i \|G_i\|_1 + \lambda(\mu\|\overline{\mathbf{Z}}\|_* + \eta\|\overline{Z}\|_1 + \|\widehat{Z}\|_1)$$
$$\text{s. t. } G_i = D_i\tilde{I},\ \ \overline{Z} + \widehat{Z} = \overline{\Psi}^T\tilde{I},\ \ S_t P \tilde{C}_t \tilde{I}_t = B_t. \tag{3.37}$$

2. Given I^{k+1}, solve $\Omega^{k+1} \leftarrow \min_\Omega \mathbf{F}(I^{k+1}, \Omega)$, without considering the constraint $S_t P C I_t = B_t$. It is quite similar to robust image alignment. Readers are referred to [65] for detailed algorithms.

3.4 Experimental Results

Although the compressive imaging camera has not been built, the 3DCS approach can still be evaluated by feeding the intermediate images $I_t, 1 \leq t \leq T$ (Figure 3.1) with three surveillance videos from [66], i.e., an airport video (size: 144×176 pixels), a brighter lobby video (size: 128×160 pixels) and

a darker lobby video (size: 128×160 pixels), as well as a video captured by a handheld camera (building video, size: 480×480). Our 3DSM (default: TV3D+Psi3D$_1$) is compared with existing sparsity measures, such as TV2D+2DWT, 3DWT, Bk and Ck. Peak signal-to-noise ratio (PSNR) is used as the measure of recovery accuracy.

3.4.1 Parameter Selection

Assigning appropriate values to weight parameters $\lambda, \rho, \eta, \mu, \tau$ and $\beta_i, 1 \leq i \leq 5$ seems quite complicated but it is actually not. Weight parameters λ and ρ are often set to be greater than 1. η is often set to be $\frac{1}{T}$. μ depends on the rank of the background components in the video. Over-regularization parameters $\beta_i, 1 \leq i \leq 5$ prefer large values. To evaluate our 3DSM and its decoding algorithm, the values of the weight parameters are set empirically through all experiments, i.e. $\lambda = 4, \rho = 3, \eta = \frac{1}{T}, \tau = 1.6$ and $\beta_i = 100, \forall i$.

3.4.2 Evaluation of Our 3DSM in Video CS

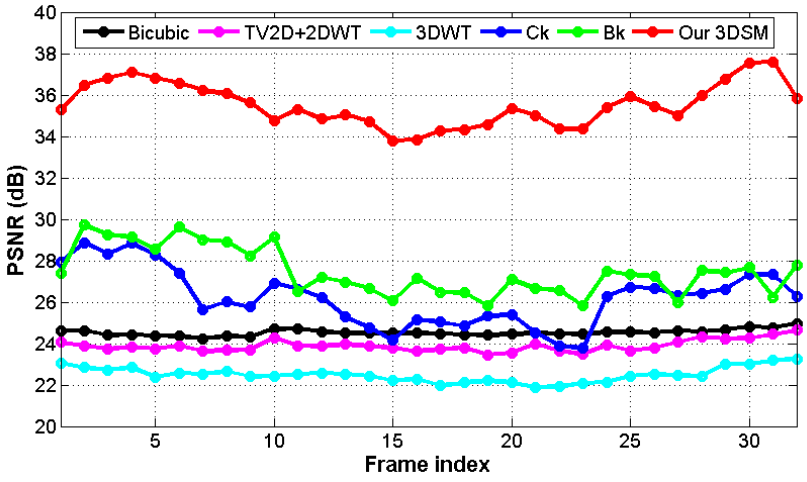

Figure 3.3: Recovery accuracy of different sparsity measures on a 32-frame airport video at sampling rate $\frac{M}{L} = 25\%$.

Fixed Sampling Rate. Our 3DSM is evaluated on the airport video (32 frames) at the sampling rate 25%, in comparison with other sparsity measures and a naive method—bicubic interpolation after half downsampling. The computing time is about 123 seconds on a normal computer (Intel E6320

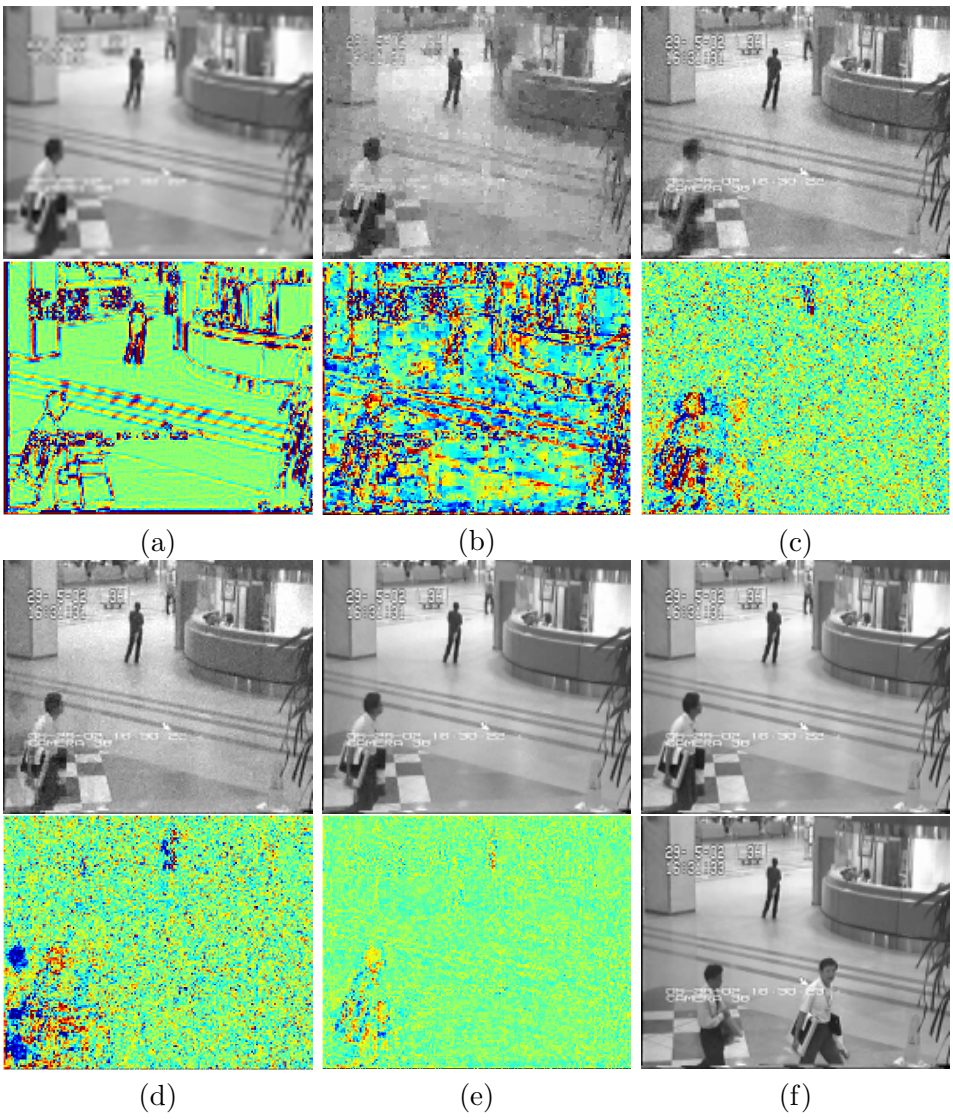

Figure 3.4: Reconstructed images (top) of 4th frame and error maps at sampling rate $\frac{M}{L} = 25\%$ using (a) bicubic (PSNR: 24.42 dB), (b) TV2D+2DWT (PSNR: 23.84 dB), (c) Ck (PSNR: 28.84 dB), (d) Bk (PSNR: 29.13 dB), and (e) our 3DSM (PSNR: 37.10 dB). (f) The original 4th (top) and 17th (bottom) frames in airport video.

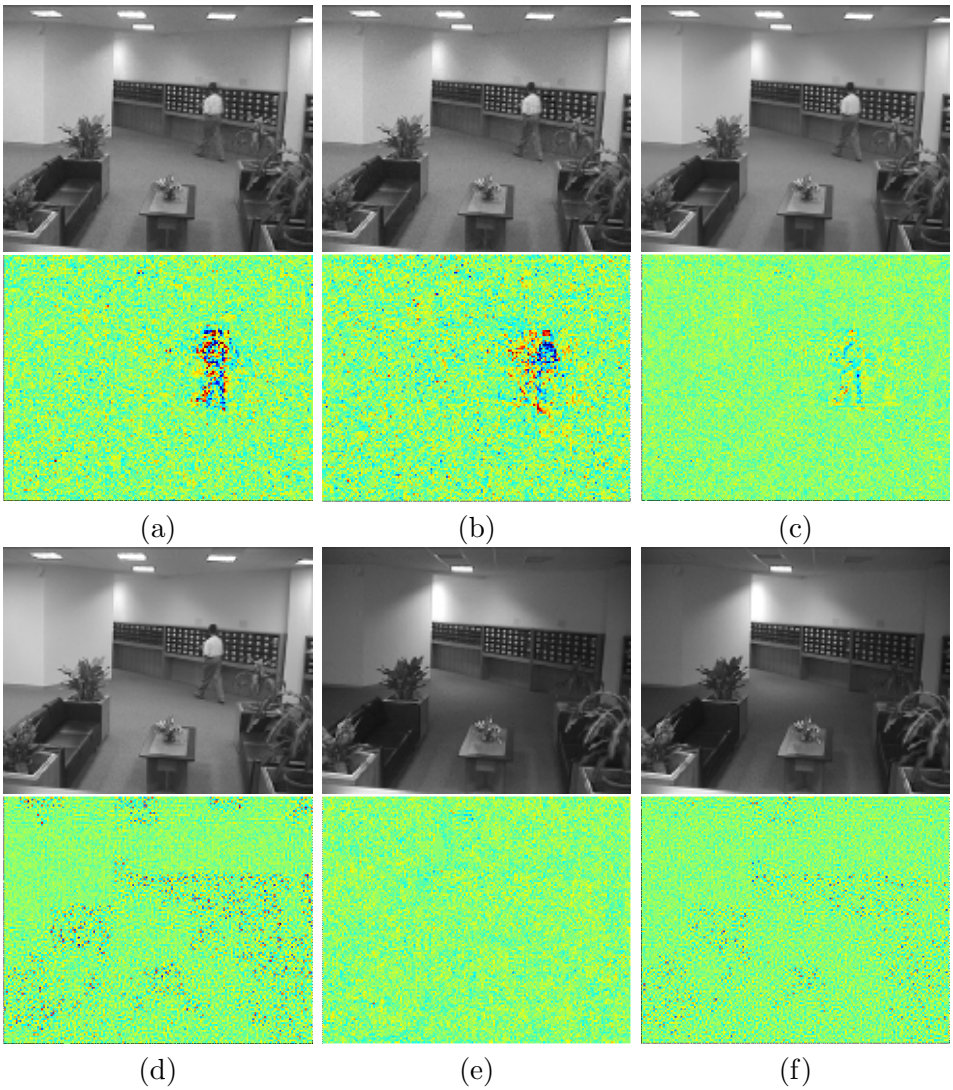

Figure 3.5: Reconstructed images (top) at $\frac{M}{L} = 30\%$ and error maps (bottom) from the bright video clip (10 frames) using (a) Ck (PSNR: 40.62 dB), (b) Bk (PSNR: 39.75 dB) and (c) our 3DSM (PSNR: 46.09 dB), with (d) their original image (top) and error map of its JPEG version (bottom), compression ratio: 30%, PSNR: 40.59 dB). (d) Our 3DSM recovery (top, PSNR: 44.66 dB) and error map (bottom) from 30% circulant samples of the darker clip (10 frames), with (f) its original image (top) and error map of its JPEG version (bottom, compression ratio: 30%, PSNR: 42.53 dB).

CPU, 3 GB memory). As shown in Figure 3.3, our 3DSM achieves a recovery accuracy at least 6 dB higher than all the other methods at each frame. 2DCS fails to achieve high recovery accuracy, for the PSNR of its state-of-art (TV2D+2DWT) is lower than bicubic interpolation, which suffers from significant blur. As shown in Figure 3.4, our 3DSM recovery is much sharper, cleaner and closer to the original 4th frame. The recovery accuracy of our 3DSM decreases as the size of moving foreground grows, e.g., the 4th and 17th frames in Figure 3.4. Our 3DSM is tested on the brighter and darker lobby videos at the sampling rate of 30%. Figure 3.5 shows that our 3DSM decodes much better images (PSNR: up to 45 dB) than other measures and the JPEG version of the original image (compression ratio: 30%). Our 3DSM achieves better recovery in the brighter lobby than that in the darker one, due to the significant photon-counting noise under the darker condition.

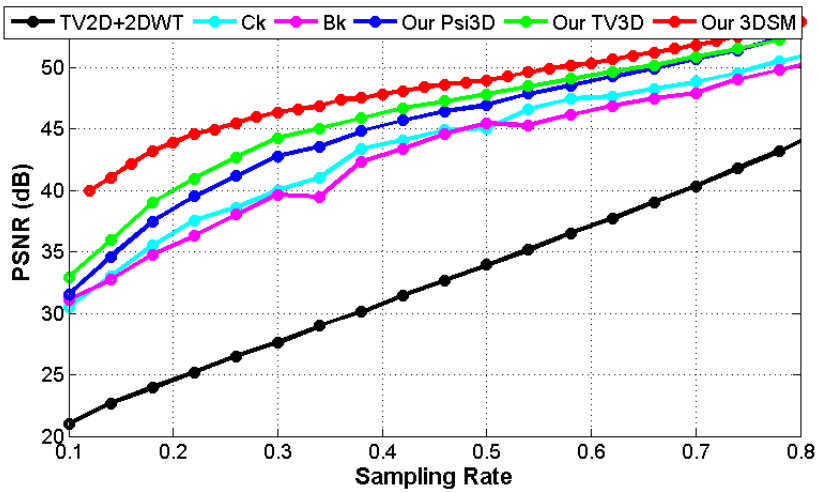

Figure 3.6: Averaged recovery accuracy of 10 frames at varying sampling rates in the brighter lobby video.

Varying Sampling Rate. By varying the sampling rate, TV3D, Psi3D$_2$ and 3DSM are tested on the brighter lobby video. As shown in Figure 3.6, either TV3D or our Psi3D is better (3 dB higher PSNR) than other measures at any sampling rate ($\frac{M}{L}$), and their combination (3DSM) is better than each one alone. The superiority of our 3DSM over other measures at $\frac{M}{L} = 25\%$ is up to 7 dB. At $\frac{M}{L} = 10\%$, 3DSM achieves the recovery accuracy (PSNR: 40 dB), which is conventionally considered to be lossless.

Varying Video Size T. As shown in Figure 3.1, our 3DCS divides a video into short clips of T frames and then decode each short clip by minimizing our

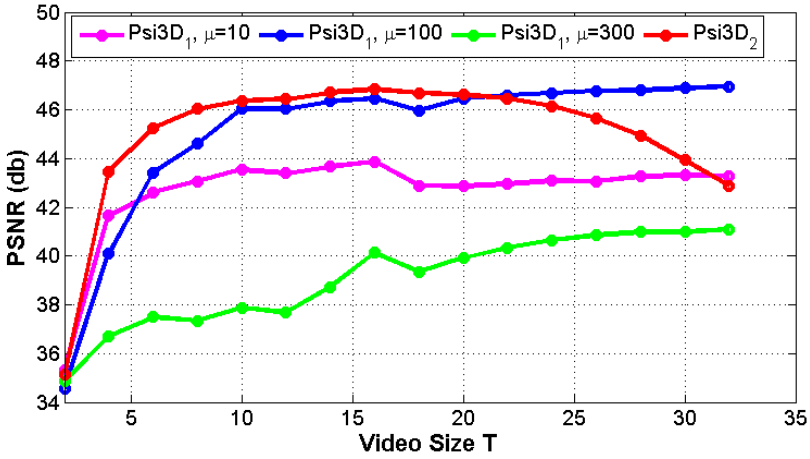

Figure 3.7: Comparison of Psi3D_1 and Psi3D_2 by varying T. This hybrid lobby video consists of 16 frames from brighter lobby and 16 from the darker one.

3DSM. To study the influence of T on the decoding accuracy, a hybrid video is built by 16 frames from brighter lobby and 16 frames from from darker lobby. The average accuracy of all T frames using our 3DSM increases quickly with T in the beginning and reaches a stable value when $T \geq 10$. When the lighting changes at the 17th frame, both the accuracy of Psi3D_1 and that of Psi3D_2 decrease to some extent (Figure 3.7).

(a) (b) (c) (d)

Figure 3.8: Low-rank recovery using our 3DSM (Psi3D_1, $\mu = 100$) from the hybrid lobby video (brighter: 16 frames and darker: 16 frames) at $\frac{M}{L} = 30\%$. Reconstructed four frames (bottom) with low-rank components (top): (a) (PSNR: 45.98 dB), (b) (PSNR: 46.36 dB), (c) (PSNR: 45.31 dB) and (d) (PSNR: 46.28 dB).

Psi3D_1 and Psi3D_2. As shown in Figure 3.7, under constant lighting ($T \leq 16$), our 3DSM using Psi3D_2 is better than using Psi3D_1 at any tuning

parameter μ. However, under varying lighting conditions ($T > 16$), the decoding accuracy of Psi3D$_1$ at $\mu = 100$ remains almost invariant (46 dB $\leq$ PSNR $\leq$ 47 dB) as T increases, and is much higher than that of Psi3D$_2$. This can be explained by the background models of Psi3D$_1$ and Psi3D$_2$. Psi3D$_1$ uses a low-rank background model and can recover rank-2 background images (top row in Figure 3.8). Thus, the innovation images of Psi3D$_1$ will be sparser than that of Psi3D$_2$, which rigidly assumes rank-1 background. Since the complete data I is unknown, the low-rank images recovered by Psi3D$_1$ are different from the real background (Figure 3.8).

Robustness over Motion. the robustness of our 3DSM over motion is evaluated by applying it to a video acquired by a moving (up and down) camera. As shown in Figure 3.9, without image alignment, our 3DSM can still recover the image sequences at $M/L = 30\%$ with acceptable accuracy (top row: PSNR $>$ 31 dB). From this initial recovery, the transformations $\Omega_t, 1 \leq t \leq 12$ are estimated, of which the dominant components are translations $(\Delta x_t, \Delta y_t)$. Given the translation knowledge, our 3DSM improves upon the initial recovery by 2.6 dB in terms of PSNR, less noise (e.g., bricks) and more detailed information (e.g., parking sign), as shown in Figure 3.9 (mid row). For computational efficiency, the translations are rounded to integer pixels. It is expected that our 3DSM recovery can be further improved by using perspective transformations.

3.5 Summary

In this chapter, a 3D compressive sampling (3DCS) approach, consisting of video circulant sampling and decoding using 3D sparsity measure (3DSM), has been proposed with an efficient decoding algorithm with convergence guarantee. By exploiting the 3D piecewise smoothness and temporal low-rank property of videos, our 3DSM reduces the required sampling rate to a practical level (e.g. 10% in Figure 3.6). Extensive experiments have been conducted to show (1) the superiority of our 3DSM over existing sparsity measures in terms of recovery accuracy with respect to the sampling rate, and (2) robustness over small camera motion. A practical design of the 3DCS camera using video circulant sampling is presented and a simpler physical implementation of circulant sampling is proposed, i.e., a random lens consisting

(a) (b) (c)

Figure 3.9: Recovery of the 12-frame building video acquired by a handheld camera using our 3DSM at $M/L = 30\%$. Top: initial results without image alignment (a) (PSNR: 31.50 dB), (b) (PSNR: 31.71 dB) and (c) (PSNR: 32.63 dB). From initial results, the estimated translations $(\Delta x, \Delta y)$ are listed as (a) (2.35, 3.11), (b) (0.62, -1.77), (c) (-0.31, 2.36). Middle: final results with estimated $(\Delta x, \Delta y)$ (a) (PSNR: 33.85 dB), (b) (PSNR: 34.10 dB) and (c) (PSNR: 35.18 dB). Bottom: three original frames.

of a random wedge array and an imaging lens.

CHAPTER 4

ROBUST ORTHONORMAL SUBSPACE LEARNING (ROSL) FOR EFFICIENT LOW-RANK RECOVERY

4.1 Introduction

The problem of learning and exploiting a low-rank matrix from its corrupted observation has become a standard paradigm in machine learning and neural networks. Its state-of-the-art methods, e.g., Robust PCA (RPCA, also called PCP in [54]) and Sparse Low-Rank Matrix Decomposition (SLRMD) [67], employ the nuclear norm as a surrogate for the highly non-convex rank minimization [68]. RPCA has been shown to be a convex problem with performance guarantee [54]. It assumes the observation matrix $X \in \mathbb{R}^{m \times n}$ is generated by additively corrupting a low-rank matrix A (rank: $r \ll \min\{m, n\}$) with a sparse matrix E. Suppose Singular Value Decomposition (SVD) of A is denoted as $A = USV^T$, where S is a diagonal matrix with singular values $S_i, 1 \leq i \leq \min\{m, n\}$) on the diagonal, RPCA recovers the low-rank matrix A from the corrupted observation X as follows:

$$\min_{A,E} \|A\|_* + \lambda \|E\|_1 \quad \text{s. t.} \quad A + E = X, \tag{4.1}$$

where nuclear norm $\|A\|_* = \sum_{i=1}^{n} S_i$.

Despite its excellent results, RPCA is computationally heavy with the complexity $\mathcal{O}(\min(m^2 n, mn^2))$, due to multiple iterations of SVD. Reducing the number of the required SVD operations is a possible remedy [69], yet the computational load is dominated by SVD itself. Instead of full SVD, partial RPCA [70], (P-RPCA) computes κ ($r < \kappa$) major singular values, thus it has $\mathcal{O}(\kappa mn)$ complexity. Nevertheless, P-RPCA requires a proper way to preset the optimal value of κ. GoDec [71] uses bilateral random projection to accelerate the low-rank approximation in RPCA. Similarly, RP-RPCA [72] applies random projection P on A (i.e., $A' = PA$) and then minimizes the

rank of A'. However, rank minimization using randomized SVD is unstable and might be even slower than RPCA, for it requires conducting SVD on many different projected matrices A' at each iteration.

Non-convex matrix factorization approaches including RMF [73] and LMaFit [74] have been also proposed for fast low-rank recovery. Instead of minimizing the rank of A, these approaches represent A under some preset-rank subspaces (spanned by $D \in \mathbb{R}^{m \times k}$) as $A = D\alpha$, where coefficients $\alpha \in \mathbb{R}^{k \times n}$ and $r < k \ll \min(m, n)$. Due to its SVD-free property, these non-convex matrix factorization approaches are computationally preferable to RPCA. Still, their quadratic complexity $\mathcal{O}(kmn)$ is prohibitive for large-scale low-rank recovery. Besides, they require an accurate initial rank estimate, which is not easy to obtain itself.

This chapter presents a computationally efficient low-rank recovery method, called as Robust Orthonormal Subspace Learning (ROSL). Motivated by the group sparsity (structure) in sparse coding [75, 76, 77, 78, 79], ROSL speeds the rank-minimization of a matrix A by imposing the group sparsity of its coefficients α under orthonormal subspace (spanned by orthonormal bases D). Its underlying idea is that, given the subspace represenation $A = D\alpha$, the rank of A is upper bounded by the number of nonzero rows of α. ROSL can be regarded as a non-convex relaxation of RPCA by replacing nuclear norm with this rank heuristic. First, this relaxation enables the employment of efficient sparse coding algorithms in low-rank recovery, therefore ROSL has only $\mathcal{O}(rmn)$ $(r < \kappa, k)$ complexity, much faster than RPCA. Second, by imposing this rank heuristic, ROSL is able to seek the most compact orthonormal subspace that represents the low-rank matrix A without requiring accurate rank estimate (unlike RMF and LMaFit). Third, this rank heuristic is proven to be lower bounded by nuclear norm, which means that ROSL has the same global minimum as RPCA.

An efficient ROSL solver is also presented. This solver incorporates a block coordinate descent (BCD) algorithm into an inexact alternating direction method (ADM). Despite its non-convexity, this solver is shown to exhibit strong convergence behavior, given random initialization. Experimental results validate that the solution obtained by this solver is identical or very close to the global optimum of RPCA.

As a minor contribution, a random sampling algorithm is introduced to further speed up ROSL such that ROSL+ has linear complexity $\mathcal{O}(r^2(m+n))$.

At the time of writing this chapter, we became aware of the related work [80], describing a similar sampling based framework (DFC) for RPCA. Although following the same idea—Nystrom method [81, 82, 83], ROSL+ and DFC are proposed to attack different problems, i.e., ROSL and RPCA, in different manners. In addition, ROSL+ elucidates a key point in Nystrom method—how to estimate multiple sub-matrices, which were missed by DFC.

4.2 Robust Orthonormal Subspace Learning

As shown in Figure 4.1, similar to RPCA, ROSL assumes that the observation $X \in \mathbb{R}^{m \times n}$ is generated by adding a low-rank matrix A (rank: $r \ll \min\{m, n\}$) and a sparse outlier matrix E. Different from RPCA that uses the principal subspace, ROSL represents the low-rank matrix A under an ordinary orthonormal subspace (spanned by $D = [D_1, D_2..., D_k] \in \mathbb{R}^{m \times k}$), denoted as $A = D\alpha$, where coefficients $\alpha = [\alpha_1; \alpha_2; ...; \alpha_k] \in \mathbb{R}^{k \times N}$ and α_i specifies the contribution of D_i to each column of A. The dimension k of the subspace is set as $k = \beta_1 r$ ($\beta_1 > 1$ is a constant).

4.2.1 Group Sparsity under Orthonormal Subspace

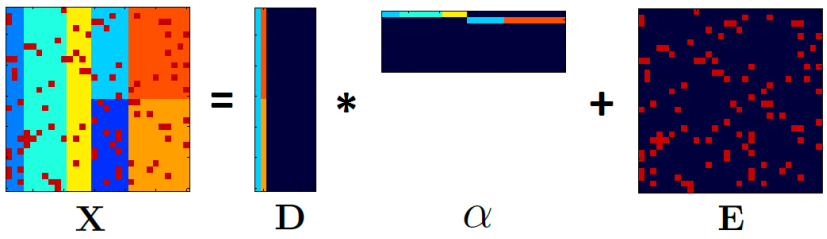

Figure 4.1: Illustration of the observation model $X = A + E = D\alpha + E$ in ROSL.

ROSL introduces a new formulation of rank minimization to replace the nuclear norm used in RPCA. Although the Frobenius-norm regularization is a valid substitute for nuclear norm, as shown in Lemma 1, it fails to recover the low-rank matrix without rank estimate.

Lemma 1 $\|A\|_* = \min_{D,\alpha} \frac{1}{2}(\|D\|_F^2 + \|\alpha\|_F^2) \quad s.\ t. \quad A = D\alpha$ [84, 85].

Motivated by the group sparsity [75, 76, 77, 78, 79], ROSL represents A under some vector subspace D and constraints the rank of A by imposing the group sparsity of its coefficients α. Its main idea is that, given $A = D\alpha$, the rank of A, or exactly α, is upper bounded by the number of nonzero rows of α, i.e. $\|\alpha\|_{\text{row-0}}$. In order to avoid the vanishing of coefficients α, the subspace bases are constrained to be on the unit sphere, i.e., $D_i^T D_i = 1, \forall i$. To further enable the group sparsity of α is a valid measure of rank (A), we should eliminate the correlation of columns of D by constraining it to be orthonormal, i.e., $D^T D = I_k$, where I_k is an identity matrix. Thus, ROSL recovers the low-rank matrix A from X by minimizing the number of nonzero rows of α, and the sparsity of E as follows:

$$\min_{E,D,\alpha} \|\alpha\|_{\text{row-0}} + \lambda \|E\|_0 \quad \text{s. t.} \quad D\alpha + E = X, D^T D = I_k, \forall i. \tag{4.2}$$

Lemma 2 *$\|A\|_* = \|\alpha\|_{\text{row-1}}$, when $A = D\alpha, D^T D = I_k$ and α consists of orthogonal rows.*

It is well known that sparsity-inducing ℓ_1-norm is an acceptable substitute for the sparsity measure (i.e., ℓ_0-norm). Similarly, the row-1 norm, which is defined as $\|\alpha\|_{\text{row-1}} = \sum_{i=1}^{k} \|\alpha_i\|_2$, is a good heuristic for the row sparsity (i.e., row-0 norm). Actually, it is easy to reach the conclusion that the nuclear norm $\|A\|_*$ is equal to the group sparsity $\|\alpha\|_{\text{row-1}}$ under orthonormal subspace D, where $A = D\alpha$, if rows of α are orthogonal, as stated in Lemma 2. In this case, the subspace bases $D = U$ and coefficients $\alpha = SV^T$, where $A = USV^T$ by SVD. For the computational efficiency, ROSL removes this orthogonal constraint on *alpha* and recover the low-rank matrix A from X by minimizing the row-1 norm of α, and the ℓ_1-norm of E.

$$\min_{E,D,\alpha} \|\alpha\|_{\text{row-1}} + \lambda \|E\|_1 \quad \text{s. t.} D\alpha + E = X, D^T D = I_k, \forall i. \tag{4.3}$$

4.2.2 Bound of Group Sparsity under Orthonormal Subspace

To show ROSL is a valid non-convex relaxation of the performance-guaranteed RPCA, we investigate the relationship between the group-sparsity-based rank formulation with matrix rank/nuclear norm.

Proposition 2 *Consider a thin matrix $A \in \mathbb{R}^{m \times n}$ $(m \geq n)$, its SVD and*

orthonormal subspace decomposition are respectively denoted as $A = USV^T$ *and* $A = D\alpha$*, where* $D \in \mathbb{R}^{m\times n}, \alpha \in \mathbb{R}^{n\times n}$ *and* $D^TD = I_n$ *without loss of generality. The minima of row-0 group sparsity and row-1 group sparsity of* A *under orthonormal subspace are respectively equal to rank(*A*) and nuclear norm* $\|A\|_*$*.*

$$\text{(P1.1)} \qquad \min_{D\alpha=A, D^TD=I_n} \|\alpha\|_{\text{row-0}} = \text{rank}(A), \tag{4.4}$$

$$\text{(P1.2)} \qquad \min_{D\alpha=A, D^TD=I_n} \|\alpha\|_{\text{row-1}} = \|A\|_*. \tag{4.5}$$

Proof of (P1.1) It is straightforward that the rank of A, where $A = D\alpha$, should not be larger than the dimension of α, resulting in that $\|\alpha\|_{\text{row-0}} \geq \text{rank}(\alpha) \geq \text{rank}(A)$. Thus, the row-0 norm of α under orthonormal subspace D is lower bounded by the rank of A.

Proof of (P1.2) This part can be restated as: $\|\alpha\|_{\text{row-1}} = \sum_{i=1}^{n} \|\alpha_i\|_2$, will reach its minimum $\|A\|_*$, when the orthonormal bases are equal to the principal components, i.e., $D = U$, where $A = USV^T$ by SVD. For simplicity of proof, we ignore other trivial solutions—the variations (column-wise permutation or $\pm$ column vectors) of U. Since both D and U are orthonormal bases, we reach the relationship, $D = U\Omega$ and $\alpha = \Omega^T SV^T$, where Ω is a rotation matrix ($\Omega^T\Omega = I_n, \det(\Omega) = 1$). Here, we introduce a decreasing sequence of non-negative numbers $\sigma_i, 1 \leq i \leq n$ such that $S_i = \sigma_i, 1 \leq i \leq n$. To validate (P1.2), we need to prove that the following relation holds for any Ω (the equality holds when Ω is the identity matrix).

$$\|\alpha\|_{\text{row-1}} = \|\Omega^T SV^T\|_{\text{row-1}} \geq \sum_{i=1}^{n} S_i = \|A\|_*. \tag{4.6}$$

1. We begin with the special case that all the singular values are identical. Specifically, we decrease the singular values such that $\forall i \in \{1, ..., n\}$, $S_i = \sigma_n$, where σ_n is the last number in the decreasing sequence $\sigma_i, 1 \leq i \leq n$. Since each row of the rotation matrix Ω is a unit vector, we reach the following relationship:

$$\|\alpha\|_{\text{row-1}} = \sum_{j=1}^{n} \sqrt{\sum_{i=1}^{n} \Omega_{ij}^2 S_i^2} = n\sigma_n = \sum_{i=1}^{n} S_i = \|A\|_*. \tag{4.7}$$

2. Then, we try to prove that $\|\alpha\|_{\text{row-1}} \geq \|A\|_*$ still holds in the general case, i.e., $S_i = \sigma_i, 1 \leq i \leq n$. We can transform the special case into the general case by $n-1$ steps, among which the t^{th} step is increasing the top $n-t$ singular values $(S_i, 1 \leq i \leq n-t)$ from σ_{n-t+1} to σ_{n-t}. When increasing $S_i, 1 \leq i \leq n-1$ from σ_n to σ_{n-1} in the first step, the partial derivative of $\|\alpha\|_{\text{row-1}}$ with respect to S_i is calculated as follows:

$$\frac{\partial \|\alpha\|_{\text{row-1}}}{\partial S_i} = \sum_{j=1}^{n} \frac{\Omega_{ij}^2}{\sqrt{\sum_{t=1}^{n-1} \Omega_{tj}^2 + \Omega_{nj}^2 (S_n^2 / S_i^2)}}. \tag{4.8}$$

Since $S_n \leq S_i, 1 \leq i \leq n-1$ and $\sum_{t=1}^{n} \Omega_{tj}^2 = 1$, we reach the following relationship:

$$\frac{\partial \|\alpha\|_{\text{row-1}}}{\partial S_i} \geq \sum_{j=1}^{n} \Omega_{ij}^2 = 1 = \frac{\partial \|A\|_*}{\partial S_i}. \tag{4.9}$$

Thus, $\|\alpha\|_{\text{row-1}} \geq \|A\|_*$ holds when increasing $S_i, 1 \leq i \leq n-1$ in the first step. In the same way, we can prove that $\|\alpha\|_{\text{row-1}} \geq \|A\|_*$ holds in the following $n-2$ steps.

3. In sum, $\|\alpha\|_{\text{row-1}} \geq \|A\|_*$ in the general case where singular values S_i are not identical, i.e., $S_i = \sigma_i, \forall i \in \{1, ..., n\}$.

According to Proposition 2, the minimum of row-1 group sparsity under orthonormal subspace is the nuclear norm, i.e., $\|\alpha\|_{\text{row-1}} \geq \|A\|_*$, where $A = D\alpha$ and $D^T D = I_k$. Suppose, at weight λ, RPCA recovers the low-rank matrix as its ground truth A^*, i.e., $\widehat{A} = A^*$, then, $\|\widehat{\alpha}\|_{\text{row-1}} + \lambda \|X - \widehat{A}\|_1 \geq \|\widehat{A}\|_* + \lambda \|X - \widehat{A}\|_1 \geq \|A^*\|_* + \lambda \|X - A^*\|_1$ holds for any $(\widehat{A}, \widehat{D}, \widehat{\alpha})_{\widehat{A} = \widehat{D}\widehat{\alpha}, \widehat{D}^T \widehat{D} = I_k}$. In sum, at the weight λ, ROSL has the same global minimum $(\widehat{A} = A^*, \widehat{D} = U, \widehat{\alpha} = SV^T)$ as RPCA, where $A^* = USV^T$ by SVD.

4.2.3 A General Framework of Robust Low-Rank Recovery Approaches

ROSL can be considered to be a compromise between RPCA and ordinary matrix factorization methods (e.g. RMF and LMaFit). On one hand, ROSL

improves upon RMF and LMaFit by seeking the group sparsity of A under orthonormal subspace D. This helps it to recover the low-rank structure of X without requiring accurate rank estimate. On the other hand, ROSL is a non-convex relaxation of RPCA by replacing nuclear norm $\|A\|_*$ with the group sparsity $\|\alpha\|_{\text{row-1}}$ under orthonormal subspace. As stated in Lemma 2, the nuclear norm $\|A\|_*$ is equal to the group sparsity $\|\alpha\|_{\text{row-1}}$ under orthonormal subspace D, where $A = D\alpha$, if rows of α are orthogonal. By removing the orthogonality constraint on α, ROSL can efficiently solve the low-rank recovery problem by sparse coding algorithms without requiring multiple iterations of SVD. To better comparison of our ROSL with other existing approaches, we present a general framework of robust low-rank recovery approaches, as shown in Table 4.1.

Table 4.1: A general framework of robust low-rank recovery approaches. Given a corrupted low-rank matrix $X = A + E$, $A \in \mathbb{R}^{m\times n}$ $(m > n)$ and its projected version A' can be represented as $A = D\alpha$ and $A' = D'\alpha'$. All approaches follow the same framework—minimizing the sparsity and rank measures under some constraints, where I_n and Δ_n respectively denote identity and diagonal matrices.

Approaches	RPCA/SLRMD	RP-RPCA	RMF	LMaFit	ROSL
Sparsity Measure	$\|E\|_1$	$\|E\|_1$	$\|E\|_1$	$\|E\|_1$	$\|E\|_1$
Rank Measure	$\|\alpha\|_{\text{row-1}}$	$\|\alpha'\|_{\text{row-1}}$	$\|D\|_F^2 + \|\alpha\|_F^2$	N/A	$\|\alpha\|_{\text{row-1}}$
Constraints	$D^TD = I_n$ $\alpha^T\alpha = \Delta_n$	$D'^TD' = I_n$ $\alpha'^T\alpha' = \Delta_n$	N/A	N/A	$D^TD = I_n$
SVD	dependent	dependent	free	free	free

4.3 Efficient Algorithm for ROSL

In this section an efficient algorithm is presented to solve the ROSL problem in Eq. (4.3).

4.3.1 Alternating Direction Method

Similar to [70], we apply the augmented Lagrange multiplier (ALM) [86] to remove the equality constraint $X = D\alpha + E$ in Eq. (4.3). Its augmented

Algorithm 2 Efficient ROSL Solver by inexact ALM-ADM and BCD

Require: $X \in \mathbb{R}^{m\times n}$, k, λ.
Ensure: D, α, E.

```
E^0 = Y^0 = zeros(m, n), D^0 = zeros(m, k), α^0 = rand(k, n), μ^0 > 0, ρ > 1, i = 0.
while E not converged do
    for t = 1 → k do
        Compute the t^th residual: R_t^i = X − E^i + Y^i/μ^i − Σ_{j<t} D_j^{i+1} α_j^{i+1} − Σ_{j>t} D_j^i α_j^i.
        Orthogonalization:
        R_t^i = R_t^i − Σ_{j=1}^{t−1} D_j^{i+1} (D_j^{i+1})^T R_t^i.
        Update: D_t^{i+1} = R_t^i α_t^{iT}.
                D_t^{i+1} = D_t^{i+1} / (‖D_t^{i+1}‖_2).
        Update: α_t^{i+1} = S̄_{1/μ^i}(D_t^{i+1T} R_t^i).
    end for
    Prune: for t = 1 → k, delete (D_t^{i+1}, α_t^{i+1}) and set k = k − 1, if ‖α_t^{i+1}‖_2^2 = 0.
    Update: E^{i+1} = S_{λ/μ^i}(X − D^{i+1} α^{i+1} + Y^i/μ^i).
    Update: Y^{i+1} = Y^i + μ^i(X − D^{i+1} α^{i+1} − E^{i+1}); μ^{i+1} = ρμ^i; i = i + 1.
end while
```

Lagrangian function is written as:

$$\begin{aligned}\mathcal{L}(D,\alpha,E,Y,\mu) = \|\alpha\|_{\text{row-1}} + \lambda\|E\|_1 + Y(X - D\alpha - E) \\ + \frac{\mu}{2}\|X - D\alpha - E\|_F^2 \quad \text{s. t.} \quad D^T D = I_k, \end{aligned} \tag{4.10}$$

where μ is the over-regularization parameter and Y is the Lagrange multiplier. We solve the above Lagrange function by inexact augmented Lagragian method-alternating direction method (ALM-ADM), which iterates through the following three steps:

1. Solve $(D^{i+1}, \alpha^{i+1}) = \arg\min \mathcal{L}(D, \alpha, E^i, Y^i, \mu^i)$.
2. Solve $E^{i+1} = \arg\min \mathcal{L}(D^{i+1}, \alpha^{i+1}, E, Y^i, \mu^i)$.
3. Update $Y^{i+1} = Y^i + \mu^i(X - D^{i+1}\alpha^{i+1} - E^{i+1}), \mu^{i+1} = \rho\mu^i$, where $\rho > 1$ is a constant.

In the first step, solving D and α simultaneously with constraint $D\alpha + E = X + \frac{Y}{\mu}$ is a non-convex problem. Fortunately, the sub-problem—updating one matrix when fixing the other one is convex. This indicates solving D

and α using coordinate descent method. In the second step, we can easily update $E^{i+1} = \mathbb{S}_{\lambda/\mu^i}(X - D^{i+1}\alpha^{i+1} + \frac{Y^i}{\mu^i}))$, where shrinkage function $\mathbb{S}_a(X) = \max\{\text{abs}(X) - a, 0\} \cdot \text{sign}(X)$ and "$\cdot$" denotes element-wise multiplication.

4.3.2 Block Coordinate Descent

Motivated by group sparse coding [78], we apply block coordinate descent (BCD) to solve D and α in the first step of ALM-ADM. Suppose the subspace bases $D = [D_1, ..., D_t, ..., D_k]$ and $\alpha = [\alpha_1; ...; \alpha_t; ...; \alpha_k]$, the BCD scheme sequentially updates the pair (D_t, α_t), by leaving all the other indices intact. In this way, it allows shrinking the group sparsity $\|\alpha\|_{\text{row-1}}$ under the orthonormal subspace D, while step-wisely updating (D_t, α_t). In addition, it obtains new subspace bases and coefficients that best fit the constraint $A = D\alpha$ and thus achieves a higher convergence rate, as explained in [87, 88]. The BCD scheme sequentially updates each pair $(D_t, \alpha_t), 1 \leq t \leq k$ such that $D_t\alpha_t$ is a good rank-1 approximation to R_t^i, where the residual is defined as $R_t^i = X + \frac{Y^i}{\mu^i} - E^i - \sum_{j<t} D_j^{i+1}\alpha_j^{i+1} - \sum_{j>t} D_j^i\alpha_j^i$. Thus, if removing the orthonormal constraint on D, the pair (D_t, α_t) can be efficiently updated as follows:

$$D_t^{i+1} = R_t^i {\alpha^i}^T, \tag{4.11}$$

$$\alpha_t^{i+1} = \frac{1}{\|D_t^{i+1}\|_2^2}\overline{\mathbb{S}}_{1/\mu^i}({D_t^{i+1}}^T R_t^i), \tag{4.12}$$

where $\overline{\mathbb{S}}_a(X) = \max\{\|X\|_2 - a, 0\}X/\|X\|_2\}$ if $\|X\|_2 > 0$ is the magnitude shrinkage function. Due to the space limit, we refer the readers to [78] for the detailed induction of Eq. (4.12).

When taking into account the orthonormal subspace, we need orthonormalise D_t^{i+1} by the Gram-Schmidt process. As shown in Algorithm 2, the new D_t^{i+1} is obtained via three steps: (1) project R_t^i onto the null space of $[D_1, ..., D_{t-1}]$, (2) update D_t^{i+1} as Eq. (4.11) and (3) then project it onto the unit sphere by normalization.

The BCD scheme attempts to keep sequentially fitting the rank-1 subspaces $(D_t^{i+1}\alpha_t^{i+1})$ to the objective $X + \frac{Y^i}{\mu^i} = D^{i+1}\alpha^{i+1} + E^i$, until the fitted subspace is canceled by magnitude shrinkage, i.e., $\|\alpha_t^{i+1}\|_2 = 0$. To improve the computational efficiency, we shrink the subspace dimension k by pruning

the zero pairs, for they will stay zero in the next iteration.

It is possible to run many rounds of BCD to solve D^{i+1} and α^{i+1} exactly in the first step of ALM-ADM. In practice, updating $(D_t^{i+1}, \alpha_t^{i+1})$, $1 \leq t \leq k$ once at each round of ALM-ADM is shown to be sufficient for the inexact ALM-ADM algorithm to converge to a valid solution (D^{i+1}, α^{i+1} and E^{i+1}) to Eq. (4.3).

As shown in Algorithm 2, ROSL can be solved using inexact ALM-ADM at the higher scale and inexact BCD at the lower scale. To the best of our knowledge, there is no established convergence theory, either for ALM-ADM algorithms applied to non-convex problems with more than two groups of variables [74], or for BCD algorithms applied to sparse coding [87, 78]. As all non-convex problems, ROSL has no theoretical guarantee of convergence. However, empirical evidence suggests that ROSL solver has strong convergence behavior and provides a valid solution: $A^{i+1} = D^{i+1}\alpha^{i+1}$ and E^{i+1}, when the initialize E^0, Y^0 and D^0 as zero matrices, as well as α^0 as a random matrix.

4.3.3 Computational Complexity

Compared with RPCA, which has cubic complexity of $\mathcal{O}(\min(m^2n, mn^2))$, ROSL is much more efficient. Its dominant computational processes are (1) left multiplying the residual matrix $R \in \mathbb{R}^{m \times n}$ by D, and (2) right multiplying it by α. Since the subspace dimension k will quickly converge to the rank r, where $r \leq k \ll \min(m, n)$, ROSL has the quadratic complexity of matrix size, i.e., $\mathcal{O}(mnr)$.

4.4 Acceleration by Random Sampling

Motivated by the Nystrom method [81, 82, 83], we present a random sampling algorithm to further speed up ROSL such that its accelerated version (ROSL+) has linear complexity with respect to the matrix size.

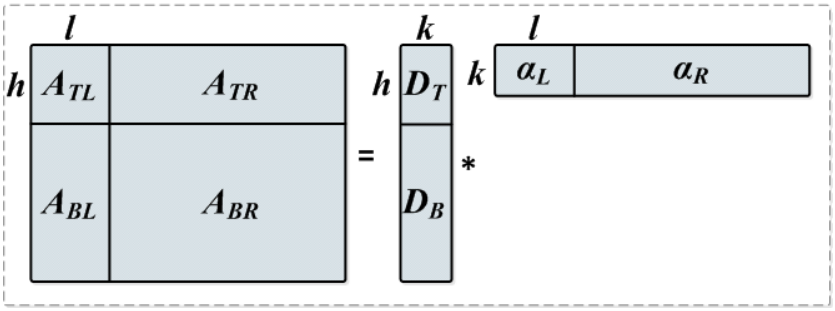

Figure 4.2: Decomposition of the low-rank matrix $A \in \mathbb{R}^{m \times n}$.

4.4.1 Random Sampling in ROSL+

As shown in Figure 4.2, the low-rank matrix $A \in \mathbb{R}^{m \times n}$ is first permuted column-wisely and row-wisely, and then divided into four sub-matrices ($A_{TL} \in \mathbb{R}^{h \times l}$, A_{TR}, A_{BL} and A_{BR}). Accordingly, top sub-matrix A_T and left sub-matrix A_L are respectively defined as $A_T = [A_{TL}, A_{TR}]$ and $A_L = [A_{TL}; A_{BL}]$. The same permutation and division are done on X and E. As shown in Figure 4.2, subspace bases D is divided into $D_T \in \mathbb{R}^{h \times k}$ and D_B, as well as coefficients α is divided into $\alpha_L \in \mathbb{R}^{k \times l}$ and α_R, such that

$$A = \begin{bmatrix} A_{TL} & A_{TR} \\ A_{BL} & A_{BR} \end{bmatrix} = \begin{bmatrix} D_T \\ D_B \end{bmatrix} [\alpha_L \quad \alpha_R]. \tag{4.13}$$

The Nystrom method is initially used for large dense matrix approximation [82], and extended to speed up RPCA in DFC [80]. Suppose $\text{rank}(A_{TL}) = \text{rank}(A) = r$, instead of recoverying the full low-rank matrix A, DFC first recovers its sub-matrices and then approximates $\widehat{A}$ as:

$$\widehat{A} = \widehat{A_L}(\widehat{A_{TL}})^{+}\widehat{A_T}, \tag{4.14}$$

where "+" denotes pseudo-inverse. However, DFC does not describe how to estimate the top-left sub-matrice.

Here, we investigate this specific issue and further simplify the Nystrom method in the framework of robust subspace learning. An intuitive solution would be independently recovering all three sub-matrices. But this requires exhaustively tuning different parameters λ, which eventually prevents from achieving high accuracy. The feasible way is that ROSL+ directly recovers the left sub-matrix and the top sub-matrix, i.e., $\widehat{A_L} = \widehat{D}\widehat{\alpha_L}$ and $\widehat{A_T} = \widehat{D_T}\widehat{\alpha}$,

and then approximates $\widehat{A_{TL}}$ by the left sub-matrix of $\widehat{A_T}$. Thus, the low-rank matrix A can be reconstructed as follows:

$$\widehat{A} = \widehat{A_L}((\widehat{A_T})_L)^+\widehat{A_T} = \widehat{D}\widehat{\alpha_L}((\widehat{\alpha})_L)^+\widehat{\alpha}, \tag{4.15}$$

where $(X)_L$ denotes the left sub-matrix of X. Actually, when $\text{rank}(A_{TL}) = \text{rank}(A)$ holds, $\widehat{\alpha_L}$ recovered from the left observation matrix X_L is a good approaximation to, or exactly equal to, $(\widehat{\alpha})_L$ recovered from the top observation matrix X_T. The same relationship exists between $(\widehat{D})_T$ and $\widehat{D_T}$, where $(\widehat{D})_T$ denotes the top sub-matrix of $\widehat{D}$. Thus, we can further simplify ROSL+ as

$$\widehat{A} = \widehat{D}\widehat{\alpha}, \tag{4.16}$$

where $\widehat{D}$ and $\widehat{\alpha}$ are respectively recovered from X_L and X_T in the following two simple steps.

1. Solve $\widehat{D}$ and $\widehat{\alpha_L}$ by applying ROSL on X_L:

$$\min_{D,\alpha_L,E_L} \|\alpha_L\|_{\text{row-1}} + \lambda\|E_L\|_1 \text{ s. t.} X_L = D\alpha_L + E_L, D^TD = I_k. \tag{4.17}$$

2. Solve $\widehat{\alpha}$ by minimizing $\|X_T - \widehat{D_T}\alpha\|_1$ by fixing $\widehat{D_T}$ as $(\widehat{D})_T$.

In other words, ROSL+ first recovers $\widehat{D}$ from the left sub-matrix X_L (complexity: $\mathcal{O}(mlr)$), and then solve $\widehat{\alpha}$ by minimizing the ℓ_1-norm of $X_T - \widehat{D_T}\alpha$ (complexity: $\mathcal{O}(nhr)$). Thus, the complexity of ROSL+ is $\mathcal{O}(r(ml + nh))$. When the matrix rank r is much smaller that its size, i.e., $r \ll \min(m, n)$, the sample number can be set as $l = \beta_2 r$ and $h = \beta_3 r$, where β_2 and β_3 are constants larger than 1. In this case, ROSL+ has the linear complexity of the matrix size, i.e., $\mathcal{O}(r^2(m + n))$.

4.4.2 Performance Guarantee of ROSL+

The performance of ROSL+ depends on if the randomly sampled sub-matrix $A_{TL} \in \mathbb{R}^{h\times l}$ can keep the rank-r structure of the full matrix A. In the first step, according to Proposition 2, ROSL+ tends to recover the subspace basis $\widehat{D} = U_L$ from the left sub-matrix X_L, where $A_L = U_L S_L U_L^T$ by SVD. When $\text{rank}(A_{TL}) = \text{rank}(A)$, suppose $A = USV^T$, we can induce U_L is equal to

the rotated veriosn of U, i.e., $\widehat{D} = U_L = U\Omega$. In this second step, when $\text{rank}(A_{TL}) = \text{rank}(A)$, the constraint $D_T\alpha = A_T$ is equivalent to $D\alpha = A$. Given $\widehat{D} = U\Omega$, ROSL+ can recover $\widehat{\alpha} = \Omega^T S V^T$. In this case, ROSL+ tends to recover the low-rank matrix $\widehat{A} = \widehat{D}\widehat{\alpha} = A$ with large probability.

Here, we will give the required sample number l and h such that $\text{rank}(A_{TL}) = \text{rank}(A) = r$ holds with a large probability. Before that, we need define the coherence measure (check [89, 80] for details) on an orthonormal matrix, which indicates its correlation with the canonical basis.

Definition 1 (Coherence) *Let $V = [V_{(1)}^T; ...; V_{(n)}^T] \in \mathbb{R}^{n\times r}$ $(r \leq n)$ be a matrix consisting of r orthonormal columns, where $V_{(i)}$ is its row vector, $1 \leq i \leq n$, the coherence of V is defined as:*

$$\mu(V) \triangleq \frac{n}{r} \max_{1\leq i\leq n} \|\mathbf{P}_V \mathbf{e_i}\|_2^2 = \frac{n}{r} \max_{1\leq i\leq n} \|V_{(i)}\|_2^2, \tag{4.18}$$

where $\mathbf{e_i}$ is i^{th} column of the canonical basis and $\mathbf{P}_V$ denotes the projection on the column space of V. This coherence $\mu(V)$ reaches its lower bound 1 when the magnitude of each entry is $\frac{1}{\sqrt{n}}$, and reaches its upper bound $\frac{n}{r}$ when V is a sub-matrix of the canonical basis.

Proposition 3 *Let $A \in \mathbb{R}^{m\times n}$ be a rank-r matrix ($r \ll \min\{m, n\}$) such that $A = USV^T$ by SVD, where $S \in \mathbb{R}^{r\times r}$, and A_{TL} be a sub-matrix, generated by uniformly sampling l columns and h rows from A without replacement. Given a failure probability δ, if the sampling number $l \geq cr\mu(V)\log(r\mu(V)/\delta)/\epsilon^2$ and $h \geq cr\mu(U)\log(r\mu(U)/\delta)/\epsilon^2$, then, the following relationship,*

$$\text{rank}(A_{TL}) = \text{rank}(A) = r, \tag{4.19}$$

holds with probability at least $1 - \delta$, where $c > 1$ is the over-sampling parameter and $\epsilon \in (0, 1]$ is the error tolerance.

Proposition 3 (proof in Appendix) provides the lower bound on the sampling number for keeping the rank-r structure in A_{TL} with high probability. Since $\log(r\mu(V)/\delta) \leq \log(n/\delta) < \log(n)\log(1/\delta)$, this lower bound is similar to but slightly more general (or smaller) than that of Lemma 6 in [80]. According to Proposition 3, the failure probability δ of $\text{rank}(A_{TL}) = \text{rank}(A)$ exponentially decreases with the increase of l and d.

Table 4.2: Evaluation of ROSL, ROSL+ and the existing low-rank recovery approaches on synthetic low-rank matrices (size: $m \times m$ and rank $r = 10$). The experimental parameters are set up as: (1) λ should be best tuned and identical (if there are multiple) for each method, (2) the dimension of D is initialized as $k = 30$, (3) the stop criterion is $\|X - A^{i+1} - E^{i+1}\|_F / \|X\|_F \leq 10^{-6}$, (4) max iteration number (iter) is set to be 300, and (5) the sample number $l = h = 100$. The Mean of Absolute Error (MAE) between A and $\widehat{A}$ is used to gauge the recovery accuracy. The iterations (rounds of ALM-ADM) and the total running time (seconds) are reported. Note: aEb denotes $a \times 10^b$.

m	RPCA MAE	RPCA time	P-RPCA MAE	P-RPCA time	RP-RPCA MAE	RP-RPCA time	LMaFit MAE	LMaFit time	ROSL MAE	ROSL time	ROSL-Nys1 MAE	ROSL-Nys1 time	ROSL-Nys2 MAE	ROSL-Nys2 time	ROSL+ MAE	ROSL+ time
500	2.8E-6	**2.51**	2.2E-6	**1.44**	0.025	**5.9**	0.53	**6.9**	6.3E-6	**0.78**	2.4	**0.42**	4.8E-5	**0.42**	2.95E-5	**0.31**
1000	1.0E-6	**12.7**	1.1E-6	**5.60**	0.37	**23.7**	0.38	**28.7**	6.1E-6	**2.83**	2.6	**0.89**	5.4E-5	**0.89**	3.1E-5	**0.65**
2000	5.7E-7	**112**	7.6E-7	**24.4**	0.42	**110**	0.18	**116**	2.2E-6	**12.8**	2.3	**1.56**	5.0E-5	**1.56**	3.3E-5	**1.1**
4000	1.2E-6	**981**	5.3E-7	**161**	0.77	**669**	0.034	**442**	9.8E-6	**41.8**	3.0	**3.78**	4.3E-5	**3.77**	2.7E-5	**2.5**
8000	N/A	**N/A**	6.7E-7	**802**	1.62	**3951**	0.005	**1750**	2.2E-6	**214**	2.8	**9.0**	4.6E-5	**8.9**	2.2E-5	**5.6**
Iter	18∼20		18∼20		300		300		16∼17		18∼20		18∼20		18∼20	

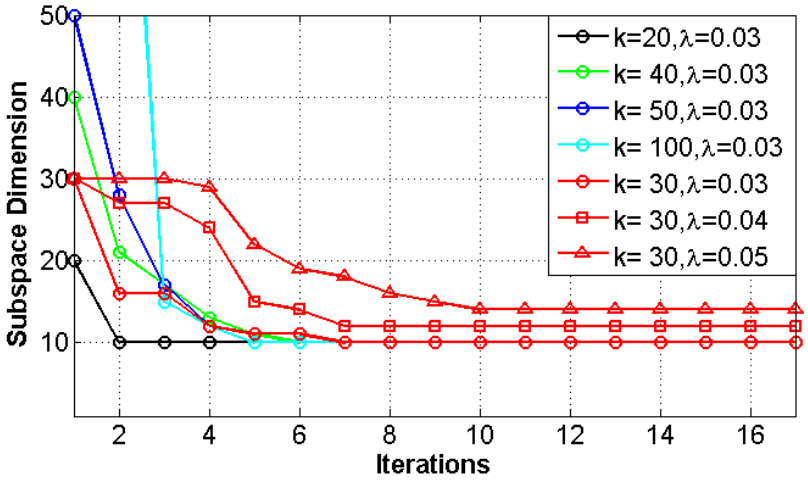

Figure 4.3: Convergence rate of ROSL. At the fixed $\lambda = 0.03$, the recovered subspace dimension always converges to $r = 10$ in less than 7 iterations **regardless** of the initial value of k, which indicates the ROSL solver is robust and very stable. The recovered subspace dimension increases as λ increases from 0.03 to 0.05. MAE $\approx 10^{-6}$ at all cases.

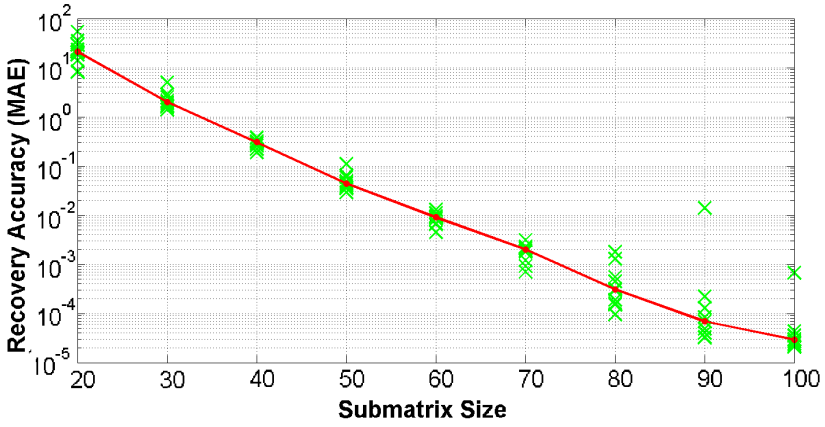

Figure 4.4: Recovery accuracy (MAE) of ROSL+ on synthetic data ($m = 1000$, $r = 10$, $k = 30$). For each l, the recovery errors (MAE) of ROSL+ in 10 different random-sampling trials are shown in green (their median in red). The recovery error (MAE) of ROSL+ decreases exponentially with the increase of l. These tests also indicate that ROSL+ gets the same global solution as RPCA in almost all cases.

4.5 Experimental Results

We present several experiments to evaluate the performance of ROSL and ROSL+, including (1) simulation on a corrupted synthetic low-rank matrix of varying dimension, (2) visual low-rank recovery on real data for background subtraction. Note that, ROSL algorithm is implemented in MATLAB without using any advanced tools unlike some other methods we compare. All the experimental results are executed on an Intel W3530 CPU and 6GB memory. For simplicity, we set the sample number $h = l$ for ROSL+ and other sampling-based methods we tested.

4.5.1 Simulations on Synthetic Data

Similar to [72], a square low-rank matrix $A \in \mathbb{R}^{m \times m}$ is synthesized as a product of a $m \times r$ matrix and a $r \times m$ matrix (r is set to be 10), whose entries obey the normal distribution. Then, the corrupted data X is generated by adding A with a sparse matrix $E \in \mathbb{R}^{m \times m}$ (10% of its entries are nonzero and drawn from the uniform distribution on [-500, 500]).

On this synthetic data, we evaluate the recovery accuracy and efficiency of ROSL, compared with RPCA, RP-RPCA and LMaFit (advanced version of RMF). As shown in Table 4.2, ROSL is much faster than these methods

without compromising the recovery accuracy. The original RPCA using full SVD is computationally costly and is almost infeasible when the matrix size $m = 8000$. Even partial RPCA [70] (P-RPCA) is consistently four times slower than ROSL and also requires a proper way to update κ. Although random projection helps reduce the computation of a single SVD, many iterations of SVD are needed to be conducted on different projected matrices. Thus, the total computation of RP-RPCA is costly and its recovery accuracy is low (Table 4.2). LMaFit seems very promising in fast low-rank recovery, however, it fails to minimize the rank of A and requires the accurate rank estimate. On this synthetic data whose corruption E has dominant magnitude, LMafit converges very slowly at $k = 30$ and ends up with the maximal iterations (Table 4.2).

To evaluate the performance of ROSL+, we apply the generalized Nystrom method (employed in DFC) to ROSL, called ROSL-Nys. Since the performance of ROSL-Nys highly depends on how to recover A_{TL}, we present two different variants of ROSL-Nys, i.e., ROSL-Nys1 recovering A_{TL} independently and ROSL-Nys2 approximating A_{TL} by left sub-matrix of A_T. Actually, DFC also employed another column sampling method. But it requires recovering multiple (i.e., $\frac{n}{l}$) sub-matrices (size:$m \times l$) and thus has quadratic complexity, much slower than ROSL+ (linear complexity). As shown in Table 4.2, RPCA-Nys1 fails to obtain accurate recovery. The reason is that tuning a common weight λ cannot guarantee the optimality of three subproblems—estimating A_L, A_T and A_{TL}. Both the computational complexity and recovery accuracy of ROSL+ are on the same order of that of ROSL-Nys2, and are slightly ($1.5 \sim 2$ times) better that the latter. This better performance is originated from that ROSL+ consists of only one time ROSL and one time linear regression.

In addition, we evaluate the stability and convergence rate of ROSL/ROSL+ on the same synthetic matrix by varying the initial rank k, weight λ or submatrix size l. First, the recovery accuracy and convergence rate of ROSL are insensible to selection of k, as long as $k > r$. As shown in Figure 4.3, $\forall k \in [20, 100]$, the subspace dimension recovered by ROSL at $\lambda = 0.03$ fast converges to the rank $r = 10$ and the high accuracy (MAE $\approx 10^{-6}$) is achieved. Second, ROSL can achieve accurate low-rank recovery at any weight $\lambda \in [0.03, 0.05]$ and the recovered subspace dimension stably increases with λ. Although ROSL recovers the 14-dimension orthonormal subspace

when $\lambda = 0.05$, ROSL still obtains high accurate recovery (MAE$\approx 10^{-6}$). Third, at the fixed sub-matrix size l, the recovery accuracy of ROSL+ is relatively stable in different random sampling trials. As the submatrix size l increases, the recovery error (MAE) of ROSL+ decreases exponentially and reaches as low as 3×10^{-5} when $l = 10r = 100$ (Figure 4.4). This result is quite in line with Proposition 3 that the failure probability δ of rank(A_{TL})=rank(A) exponentially decreases with the increase of l.

4.5.2 Visual Low-Rank Recovery

To compare the recovery accuracy of ROSL/ROSL+ with that of RPCA, we evaluate them on two standard visual data setsYale B face images and the lobby background subtraction video, similar to [54]. From each video, we build an observation matrix X by vectorizing each frame as one column, and respectively recover the low-rank component A from X by SRSL and RPCA.

In the lobby video, both ROSL and ROSL+ exactly recover the same (accurate) foreground objects and background components as RPCA at much faster speeds (ROSL: 10 times, ROSL+: 100 times) as shown in Figure 4.5. In the face image experiments, the non-diffusive component E detected by SRSL is almost the same as that by RPCA (Figure 4.6). Note that, the lobby video is a thin matrix (20480×1060) and the efficiency improvement of ROSL/ROSL+ is expected to be even higher for large-scale square matrices. Such matrices are common in typical applications, e.g., in video summarization (10^5 images of 10^6 pixels) and in face recognition (10^6 images of 10^6 pixels).

4.6 Summary

In this chapter, a Robust Orthonormal Subspace Learning (ROSL) approach is proposed for efficient robust low-rank recovery. This approach accelerates the state-of-the-art method, i.e., RPCA, by replacing the nuclear norm on the low-rank matrix by a light-weight meassure—the group sparsity of its coefficients under orthonormal subspace. This enables using fast sparse coding algorithms to solve the robust low-rank recovery problem at the quadratic complexity of the matrix size. This novel rank measure is proven to be lower-

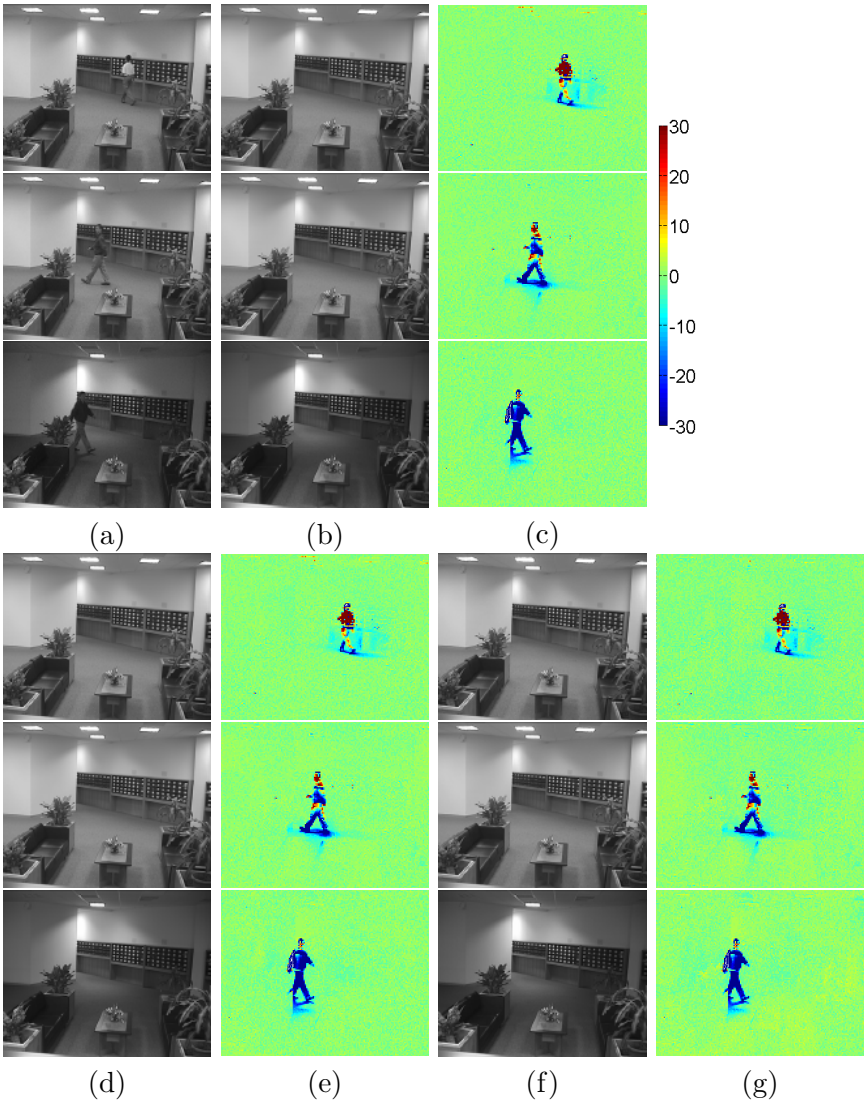

Figure 4.5: Comparison of RPCA, ROSL($k = 10$) and ROSL+($l = 50$) in background modeling on the lobby video (size: 160×128, 1060 frames). (a) Original images. Backgrounds recovered by (b) RPCA, (d) ROSL, and (f) ROSL+. Foregrounds recovered by (c) RPCA, (e) ROSL, and (g) ROSL+. ROSL (time: 34.6 s) and ROSL+ (time: 3.61 s) are significantly ($10\times$, $92\times$) faster than RPCA (time: 334 s) while generating almost identical results.

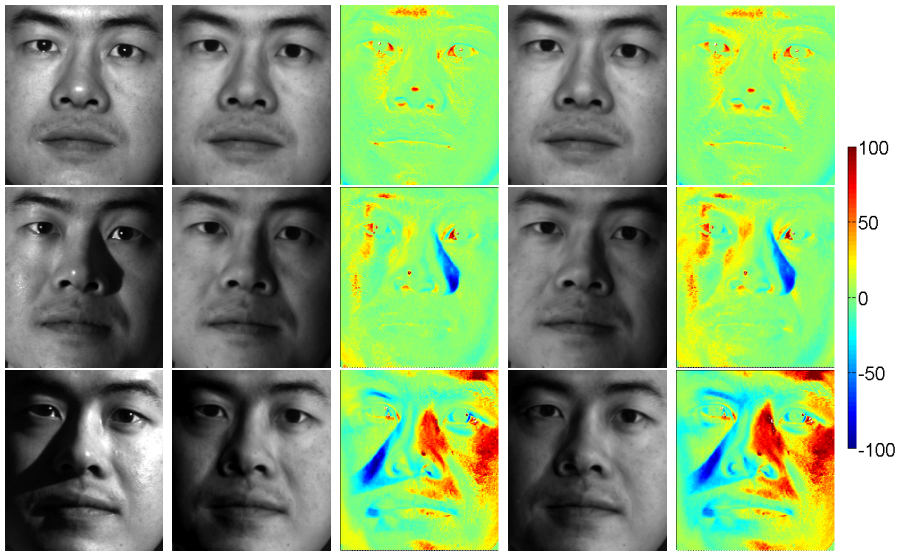

Figure 4.6: Visual evaluation of ROSL and RPCA on face images (168×192, 55 frames) under varying illuminations. There is no significant difference between ROSL and RPCA. (a) Original images, diffusive component recovered by (b) RPCA and (d) by ROSL. Non-diffusive component (shadow/specularity) by (c) RPCA and (e) by ROSL.

bounded by the nuclear norm and thus ROSL has the same global optima as RPCA. In addition, a random sampling algorithm is introduced to further speed up ROSL such that ROSL+ has linear complexity of the matrix size. The low-bound of sampling density is given as a required condition for ROSL+. Experimental results on the synthetic and real data show that ROSL and ROSL+ achieve the state-of-the-art efficiency without compromising the recovery accuracy.

CHAPTER 5

NON-LOCAL COMPRESSIVE SAMPLING (NLCS) VIA IMAGE PATCH CORRELATION

5.1 Introduction

We have witnessed the rapid development of digital image sensors with ever-increasing fidelity and resolution. Conventional digital sensors follow Shannon's Nyquist sampling theorem, which requires that the sampling rate should be above the Nyquist rate, i.e., twice the maximal analog signal frequency. While incurring no loss of information, Nyquist sampling generates a large amount of raw data, which is challenging to acquire, encode and transfer in many applications such as infrared imaging, magnetic resonance imaging (MRI) and wireless sensor networks.

Recently, compressive sensing [23] or compressive sampling (CS) [90], was developed to reduce the sampling rate below the Nyquist rate. Its main idea is that a signal can be decoded from incomplete compressive measurements by seeking its sparsity in some domain. The resulting sampling rate (defined as the ratio of the sample count to the signal size) is roughly proportional to the signal sparsity. Much effort has been made to further reduce the sampling rate of CS by exploring prior knowledge of natural images and videos. The state-of-the-art method in image CS (2DCS) [28, 35, 34] exploits two kinds of prior knowledge of natural images/videos—the piecewise smoothness by total variation (TV) [91] and the sparsity in the 2D wavelet domain. With this prior knowledge, it recovers an image I from its random measurements B as follows:

$$\min_I \mathrm{TV}(I) + \lambda \|\Psi_{2D}(I)\|_1 \quad \text{s. t.} \quad \Phi I = B, \tag{5.1}$$

where Φ is the sampling matrix, Ψ_{2D} denotes the 2D wavelet transform and λ is a regularization constant. However, due to the fact that natural images

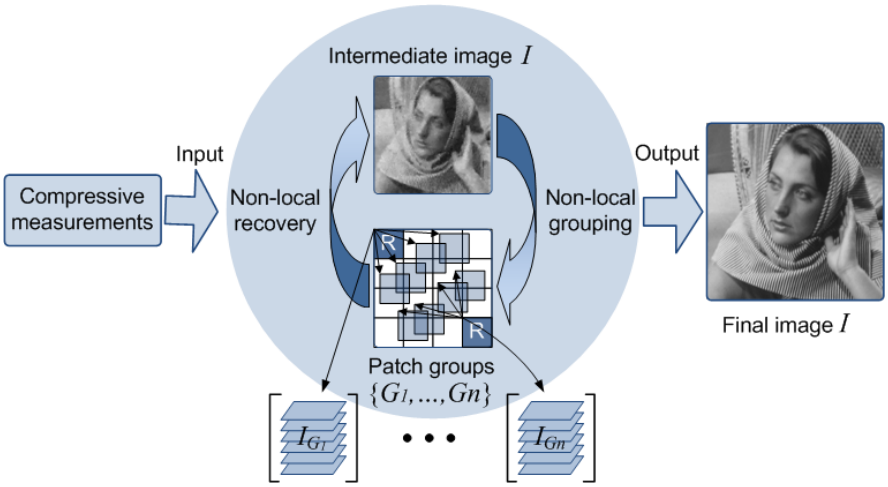

Figure 5.1: Flowchart of the proposed non-local compressive sampling (NLCS). It recovers an image I from the compressive measurements $B = \Phi I$, by iterating between two steps—(1) given an intermediate image I, non-local grouping clusters the patches into multiple groups $\{G_i\}_{i=1}^n$; (2) given the patch grouping information $\{G_i\}_{i=1}^n$, non-local recovery estimates an image I from the measurements B.

are not sufficiently sparse in the wavelet domain, 2DCS still requires a high sampling rate and its recovery tends to blur sharp edges and texture. Thus, image CS remains an idealized concept to some extent.

In this chapter, we attempt to reduce the sampling rate of image CS by exploiting a new type of prior knowledge—patch correlation or self-similarity in natural images. We name this new CS recovery method as non-local compressive sampling (NLCS). It is mainly motivated by the recent advances in the use of temporal correlation in video CS [92] and non-local mean approaches [93, 77, 94] in image restoration. First, 3DCS [92] exploits the temporal correlation (low-rank) of a video by using robust PCA (RPCA) [54], which significantly reduces the sampling rate of video CS. Analogously, the spatial correlation appears to be worth exploring in CS. Second, non-local mean approaches successfully achieve the state-of-the-art performance in image restoration [94] by seeking the correlation of image patches. Since the patch correlation is common in natural images, it should also help reduce the sampling rate in CS.

An intuitive way to seek patch correlation of an image is directly applying RPCA to minimize the rank of all its patches. However, this is infeasible, because patches from a natural image often lies in a high-dimensional sub-

space. Motivated by BM3D [94] in image denoising, we explore the patch correlation of an image by clustering its patches into multiple groups and then impose the correlation prior within each group. This means, using the patch correlation requires some information about grouping the patches. In the applications of image denoising and image compression, it is easy to obtain this grouping information by applying block matching across the image. However, in compressive sensing, the original image is unknown except for its random measurements B. Thus, our NLCS needs to recover both the image and the grouping information about its patches, which is a chicken-and-egg problem. Estimating one component requires and also benefits from the other component. In this chapter, we address this problem in an iterative framework, shown in Figure 5.1, where the unknown image and the patch grouping information are alternatively estimated.

Following are the major contributions of this chapter:

1. An NLCS recovery method that exploits non-local patch correlation and local piecewise smoothness is proposed, which significantly improves the state-of-the-art image CS method (2DCS).

2. Two non-local sparsity measures, non-local wavelet sparsity (NLWS) and non-local joint sparsity (NLJS), are proposed to exploit the patch correlation in NLCS. Compared with NLWS (used in image denoising [94]), NLJS better retains the sharp edges/texture in the recovered images and achieves higher recovery accuracy.

3. An efficient algorithm iterating between non-local grouping and non-local recovery is proposed to solve the NLCS recovery problem, which is shown to have stable convergence behavior in experiments.

5.2 Non-Local Compressive Sampling (NLCS)

5.2.1 Formulation

Besides the piecewise smoothness prior and wavelet sparsity used in 2DCS, our non-local compressive sampling (NLCS) recovery exploits another ubiquitous prior knowledge about natural images—patch correlation or self-similarity.

Let $I \in \mathbb{R}^{M\times N}$ denote a 2D image, and I_x a $d \times d$ image patch at location x (2D coordinate) on I. The patches of image I are divided into n groups $\mathcal{G} = \{G_1, ..., G_n\}$ by non-local grouping based on some similarity measure, where G_i contains the coordinates of the patches belonging to the i-th group. Patches from the i-th group stack into a 3D cube denoted by $I_{G_i} \in \mathbb{R}^{d\times d\times m_i}$, where m_i is the number of patches in group G_i. Based on the grouping information $\mathcal{G}$, we seek patch correlation of image I by minimizing its non-local sparsity (NLS). This non-local sparsity imposes the requirements that (1) image patches repeat themselves across the image and (2) image patches are sparse in some domain. Taking advantage of this non-local sparsity of images, our NLCS aims at recovering a sharp and piecewise smooth image by

$$\min_{I,\mathcal{G}} \mathrm{TV}_{\ell_1}(I) + \lambda \mathrm{NLS}(I, \mathcal{G}) \quad \text{s. t.} \quad \Phi I = B, \tag{5.2}$$

where $\mathrm{NLS}(I, \mathcal{G})$ measures the non-local sparsity of the image based on the patch grouping information $\mathcal{G}$. Here, we employ the ℓ_1-norm based total variation $\mathrm{TV}_{\ell_1}(I) = \|D_1 I\|_1 + \|D_2 I\|_1$, due to its better performance compared with the traditional total variation $\mathrm{TV}_{\ell_1\ell_2}$ [53], where D_1 and D_2 are finite difference operators along horizontal and vertical axes. For computational efficiency, we obtain the random measurements by circulant sampling $\Phi = SC$ [58, 92, 95], where C is a circulant matrix and S is a random subsampling matrix.

At the core of NLCS is the non-local sparsity (NLS) measure that gauges the correlation between patches and the sparsity of patches themselves. In this section, we will present two NLS measures, namely, non-local wavelet sparsity and non-local joint sparsity.

5.2.2 Non-Local Wavelet Sparsity

Many methods have been proposed to obtain the correlation of a signal ensemble, e.g., imposing its low-rank [54] and learning its low-dimensional subspace [78]. In NLCS, we can adapt these methods to impose the correlation of each patch group I_{G_i} (Figure 5.1) that is highly correlated and almost lies in a rank-1 subspace. However, these methods fail to take into account another important prior knowledge—the sparsity of patches themselves.

A good candidate of the non-local sparsity measure is the 3D wavelet

sparsity. It is popularly used to seek patch correlation in image denoising (e.g., BM3D) and is also employed to impose temporal correlation in video CS [50]. The core idea of employing it in NLCS is that, on the 2D wavelet coefficients of each patch in a group $\Psi_{2D}(I_{G_i})$, we compute an additional 1D wavelet transform along the third axis to bring out the non-local patch correlation. We rename it as non-local wavelet sparsity (NLWS). We compute the NLWS of an image I as the sum of the 3D wavelet sparsity of each patch group as follows:

$$\text{NLWS}(I, \mathcal{G}) = \sum_{i=1}^{n} \|\Psi_{3D}(I_{G_i})\|_1, \tag{5.3}$$

where Ψ_{3D} is the 3D wavelet transform.

5.2.3 Non-Local Joint Sparsity

Motivated by the observation that the matched patches in one group are almost identical (up to some sparse errors), we propose another NLS measure—non-local joint sparsity (NLJS). Joint sparsity (JS) is initially proposed in [57] to identify the common component and sparse innovation components in a signal ensemble. Here, we apply the joint sparsity idea to a single image I consisting of non-local patch groups ($\mathcal{G}$) and define the non-local joint sparsity of image I as follows:

$$\text{NLJS}(I, \mathcal{G}) = \sum_{i=1}^{n} \text{JS}(I_{G_i}), \tag{5.4}$$

where $\text{JS}(I_{G_i})$ is defined as follows. For each patch group I_{G_i}, we first conduct 2D wavelet transform on each patch to obtain $\Psi_{2D}(I_{G_i}) \in \mathbb{R}^{d\times d\times m_i}$. Then, we decompose $\Psi_{2D}(I_{G_i})$ into the sum of a replica of the common component $\overline{Z}_i \in \mathbb{R}^{d\times d}$ and the sparse innovation components $\widehat{Z}_i \in \mathbb{R}^{d\times d\times m_i}$. Then, the joint sparsity of I_{G_i} is defined as

$$\text{JS}(I_{G_i}) = \min_{\overline{Z}_i, \widehat{Z}_i} \|\overline{Z}_i\|_1 + \eta\|\widehat{Z}_i\|_1, \quad \text{s. t.} \quad [\overline{Z}_i : ... : \overline{Z}_i] + \widehat{Z}_i = \Psi_{2D}(I_{G_i}), \tag{5.5}$$

where $[\overline{Z}_i : ... : \overline{Z}_i]$ denotes a 3D cube consisting of m_i replicas of $\overline{Z}_i$ and η is a regularization constant that is equal to or larger than 1. Minimizing the first term $\|\overline{Z}_i\|_1$ imposes the wavelet sparsity of the patches themselves, similar to

2DCS, while minimizing the second term $\|\widehat{Z}_i\|_1$ imposes the patch correlation within each group. Therefore, for images that contain abundantly repeating local structures, η can be set larger to emphasize the patch correlation prior. Note that we have an explicit solution to the aforementioned minimization problem. The optimal common component $\overline{Z}_i$ can be obtained by element-wise applying the median filter on $\Psi_{2D}(I_{G_i})$ along the third dimension (when the patch number is even and there are two middle values for each pixel, the one with smaller-magnitude is the output of the median filter).

Comparison of NLWS with NLJS. In sum, the two non-local sparsity measures are both defined in the 2D wavelet domain, but differ in the ways they impose patch correlation. On the 2D wavelet coefficients $\Psi_{2D}(I_{G_i})$, NLWS computes an additional wavelet transform along the third dimension, and sums up the ℓ_1 norm of all 3D wavelet coefficients. Since all the wavelet coefficients (low-frequency and high-frequency) are uniformly penalized, NLWS tends to blur the patches when imposing patch correlation. Compared with NLWS, NLJS makes better use of the prior knowledge that the matched patches in one group are almost identical (up to some sparse errors). NLJS approximates $\Psi_{2D}(I_{G_i})$ by a rank-1 subspace (spanned by $\overline{Z}_i$), and then sums up the minimum ℓ_1 norm of $\overline{Z}_i$ and the approximation error $\widehat{Z}_i$. We can roughly regard $\overline{Z}_i$ as the zero-frequency component and $\widehat{Z}_i$ as the high-frequency component of $\Psi_{2D}(I_{G_i})$. From this point of view, NLJS can heavily penalize the high-frequency components while slightly regularizing the zero-frequency component. Thus, NLJS better retains the sharp edges and texture in the recovered image.

5.3 An Efficient Algorithm for NLCS

Our NLCS algorithm in Eq. (5.2) attempts to recover the underlying image I from its compressive measurements ΦI by minimizing its total variation and non-local sparsity. However, the non-local sparsity is defined based on the patch grouping $\mathcal{G}$, which in turn requires knowledge of the image I. Direct minimization over unknown I and $\mathcal{G}$ is intractable. Instead, we present an iterative algorithm to find an approximate solution, as shown in Figure 5.1. The iterative algorithm starts with an initial estimate I recovered by 2DCS, and then iterates between two steps—(1) non-local grouping that extracts

the patch grouping $\mathcal{G}$ from image I and (2) non-local joint recovery that recovers the image I based on the updated grouping information $\mathcal{G}$.

5.3.1 Non-Local Patch Grouping

We use the same block-matching scheme in BM3D [94] for non-local patch grouping. Given an estimated image I, it first obtains n reference patches, denoted as $I_{x_i^r} \in \mathbb{R}^{d\times d}, 1 \leq i \leq n$, by grid sampling with step size s. Then, for each reference patch $I_{x_i^r}$, it searches in its neighborhood for up to m best matched patches such that each matched patch I_x satisfies $D(I_{x_i^r}, I_x) = \|\Psi_{2D}(I_{x_i^r}) - \Psi_{2D}(I_x)\|_2^2/d^2 \leq \epsilon$, where ϵ is a pre-defined constant. These matched patches form the i^{th} patch group I_{G_i}.

We set the threshold value ϵ such that the popular reference patches will have more (but up to m) matched patches than the rare ones. In this way, the grouping information will help to improve the recovery accuracy of the popular patches without harming that of the rare ones. Thus, we can increase the recovery accuracy of an image consisting of abundant correlated patches, by incorporating this non-local grouping information.

Algorithm 3 Solve non-local joint recovery using inexact ALM-ADM

Require: C, S, B and $P_{ij}, \forall i, j$,
Ensure: I

1: $I^0 = g_1^0 = g_2^0 = b_1^0 = b_2^0 = R^0 = e^0 = \text{zeros}(M, N)$;
   $\overline{Z}_i^0 = \widehat{Z}_{ij}^0 = f_{ij} = \text{zeros}(N_1, N_1)$.
2: **while** I not converged **do**
3: Separate Estimate of Auxiliary Variables χ:
   $\chi^{k+1} \leftarrow \arg\min_\chi \mathcal{L}(I^k, \chi, \rho^k)$.
4: Joint Reconstruction of Image I:
   $(I^{k+1}) \leftarrow \arg\min \mathcal{L}(I, \chi^{k+1}, \rho^k)$.
5: Update of Lagragian Multipliers ρ:
   $b_l^{k+1} \leftarrow b_l^k - \tau\beta_1(g_l^{k+1} - D_l I^{k+1})$.
   $f_{ij}^{k+1} \leftarrow f_{ij}^k - \tau\beta_2(\overline{Z}_i^{k+1} + \widehat{Z}_{ij}^{k+1} - \Psi_{2D}(P_{ij} I^{k+1}))$.
   $e^{k+1} \leftarrow e^k - \tau\beta_3(R^{k+1} - CI^{k+1})$.
6: $k \leftarrow k + 1$.
7: **end while**

5.3.2 Non-Local Joint Recovery

In this subsection, we present an efficient algorithm for the non-local recovery using non-local joint sparsity (NLJS). It is straightforward to extend it to solve the recovery problem using non-local wavelet sparsity (NLWS).

We denote the j^{th} patch in the i^{th} group as $I_{G_{ij}}$ and its extraction matrix as $P_{ij} \in \mathbb{R}^{d^2 \times MN}$, i.e., a binary matrix each row of which has one nonzero entry "1". Thus, we obtain $I_{G_{ij}} = P_{ij} I$, where I and $I_{G_{ij}}$ are vectorized, for simplicity of notation. For each patch $I_{G_{ij}}$, there is a common component $\overline{Z}_i$ and an innovation component $\widehat{Z}_{ij}$ such that $\overline{Z}_i + \widehat{Z}_{ij} = \Psi_{2D}(P_{ij} I)$. Accordingly, for the patch group I_{G_i}, the 3D cube of innovation components $\widehat{Z}_i = [\widehat{Z}_{i1} : ... : \widehat{Z}_{im_i}]$. Thus, the non-local recovery problem is formulated as follows:

$$\begin{aligned} &\min_{I, \overline{Z}_i, \widehat{Z}_{ij}} \sum_{l=1}^{2} \|D_l I\|_1 + \lambda \sum_{i=1}^{n} (\|\overline{Z}_i\|_1 + \eta \sum_{j=1}^{m_i} \|\widehat{Z}_{ij}\|_1), \\ &\quad \text{s. t.} \quad SCI = B, \overline{Z}_i + \widehat{Z}_{ij} = \Psi_{2D}(P_{ij} I), \forall i, j. \end{aligned} \tag{5.6}$$

It is very difficiult to directly solve this constrained optimization problem consisting of multiple non-differentiable sparsity-inducing terms (ℓ_1 norm). So, we employ the augmented Lagrangian method-alternating direction method (ALM-ADM), also called the alternating direction method of multipliers (ADMM) in [61], to divide this complicated problem into simpler sub-problems and addresses them iteratively. This ALM-ADM algorithm has been widely used in compressive sensing [96]. By adding a set of auxiliary variables $\chi \triangleq \{g_1, g_2, \overline{Z}_i, \widehat{Z}_i, R\}$, the non-local recovery problem can be reformulated as

$$\begin{aligned} &\min_{I, \chi} \sum_{l=1}^{2} \|g_l\|_1 + \lambda \sum_{i=1}^{n} (\|\overline{Z}_i\|_1 + \eta \sum_{j=1}^{m_i} \|\widehat{Z}_{ij}\|_1) \quad \text{s. t.} \\ &\begin{cases} R = CI \\ SR = B \end{cases}, \ g_l = D_l I, \overline{Z}_i + \widehat{Z}_{ij} = \Psi_{2D}(P_{ij} I), \forall i, j, l. \end{aligned} \tag{5.7}$$

This objective function given has the desirable property that it is separable in two groups of variables— the image I and its auxiliary variables $\chi = \{g_1, g_2, R, \overline{Z}_i, \widehat{Z}_i\}$. Thus, this function can be minimized over one group of variables by fixing the other group. Let $\rho \triangleq \{b_1, b_2, f_{ij}, e\}$ be a set of La-

grangian multipliers, we can write the Lagrangian function of this equality-constrained problem as follows.

$$\begin{aligned}\mathcal{L}(I,\chi,\rho) = &\sum_{l=1}^{2}\|g_l\|_1 + \lambda\sum_{i=1}^{n}(\|\overline{Z}_i\|_1 + \eta\sum_{j=1}^{m_i}\|\widehat{Z}_{ij}\|_1)\\ &+\frac{\beta_2}{2}\sum_{i,j}\|\Psi_{2D}(P_{ij}I) - \overline{Z}_i - \widehat{Z}_{ij} + \frac{f_{ij}}{\beta_2}\|^2_{2,W_{ij}}\\ +\frac{\beta_1}{2}\sum_{l=1}^{2}\|D_lI - g_l + \frac{b_l}{\beta_1}\|_2^2 &+ \frac{\beta_3}{2}\|CI - R + \frac{e}{\beta_3}\|_2^2, \end{aligned} \tag{5.8}$$

where $SR = B$, β_1, β_2 and β_3 are large constant (e.g., 100), and P_{ij}^T is the transpose matrix of P_{ij}. We will explain the weighted ℓ_2 norm $\|\cdot\|^2_{2,W_{ij}} = (\cdot)^T W_{ij}(\cdot)$ and its weight (diagonal) matrix $W_{ij} \in \mathbb{R}^{d^2\times d^2}$ in the section Joint Reconstruction of Image I.

As shown in Algorithm 1, after just one round of alternatively minimizing the Lagrangian function $\mathcal{L}(I,\chi,\rho)$ with respect to I and χ, the multiplier ρ is updated immediately with a step length τ. Thus, the ALM-ADM algorithm has three iterative steps—(1) separate estimate of auxiliary variables χ, (2) joint reconstruction of image I and (3) update of Lagrangian multipliers ρ. With fixed Lagrangian multpliers ρ^k, we only update the image I and its auxiliary variables χ in one round of iteration. Therefore, this algorithm is also called inexact ALM-ADM [70, 96]. According to the theoretical analysis in [62], the inexact ALM-ADM is guaranteed to converge at $\tau \in (0, \frac{1+\sqrt{5}}{2})$, under certain technical assumptions.

Separate Estimate of Auxiliary Variables

In this subsection, we discuss how to estimate the auxiliary variables χ from a given image I by minimizing their sparsity-inducing ℓ_1-norm. Given a typical ℓ_1-norm minimization problem $\min_a \|a\|_1 + \frac{\beta}{2}\|a-b\|_2^2$, it has a closed-form solution $\hat{a} = \mathbb{S}_{\frac{1}{\beta}}(b)$, where $\mathbb{S}_{\frac{1}{\beta}}(b)$ is the soft thresholding function defined as $\max\{\text{abs}(b) - \frac{1}{\beta}, 0\}.*\text{sign}(b)$. Accordingly, we respectively update the partial gradients g_1 and g_2, the common patch $\overline{Z}_i$ and the innovation

component $\widehat{Z}_i$ as follows:

$$g_l^{k+1} = \mathbb{S}_{\frac{1}{\beta_1}}(D_l I^k + \frac{b_l^k}{\beta_1}). \tag{5.9}$$

$$\overline{Z}_i^{k+1} = \mathbb{S}_{\frac{1}{\beta_2}}(\frac{1}{m_i}\sum_{j=1}^{m_i}\Psi_{2D}(P_{ij}I^k) - \widehat{Z}_{ij}^k + \frac{f_{ij}^k}{\beta_2}). \tag{5.10}$$

$$\widehat{Z}_{ij}^{k+1} = \mathbb{S}_{\frac{1}{\beta_2}}(\Psi_{2D}(P_{ij}I^k) - \overline{Z}_i^{k+1} + \frac{f_{ij}^k}{\beta_2}). \tag{5.11}$$

Theoretically, to guarantee the convergence of the NLCS algorithm, we need to iteratively update the pair $(\overline{Z}_i, \widehat{Z}_i)$ until convergence. In practice, for computational efficiency, we can apply only one round of updating $(\overline{Z}_{i,i})$, which is shown to have stable convergence behavior in experimental results.

As for the circulant sample R, we first obtain it by applying circulant sampling on the image I^k and then set its subsamples at locations X (decided by B and its subsampling matrix S) as the measurements B.

$$R^{k+1} = CI^{k+1} - \frac{e^{k+1}}{\beta_3}. \tag{5.12}$$

$$R^{k+1}[X] = B. \tag{5.13}$$

Joint Reconstruction of Image I

In this section, we discuss the joint reconstruction of the image I from its auxiliary variables $\chi = \{g_1, g_2, R, \overline{Z}_i, \widehat{Z}_i, 1 \le i \le n\}$.

After the first step, we have a set of patch estimates $\Psi_{2D}(I_{G_{ij}}) = \overline{Z}_i + \widehat{Z}_{ij}$, which constitue an over-complete and spatially non-uniform representation of the image I. The conventional way to recover the image I is aggregating all the patch estimates using a weighted average. Following this aggregation method, we impose a weighted ℓ_2 norm regularization $\|(P_{ij}I) - \overline{Z}_i - \widehat{Z}_{ij} + \frac{f_{ij}}{\beta_2}\|_{2,W_{ij}}^2$ in Eq. (5.8), where $\|\cdot\|_{2,W_{ij}}^2 = (\cdot)^T W_{ij}(\cdot)$. The weight W_{ij} is defined to yield larger regularization weight on the rare patches and smaller weight on the popular ones. Specifically, for each pixel in the patch $I_{G_{ij}} = P_{ij}I$, we set its regularization weight as the inverse of its sampling frequency over all the patchs $\{I_{G_{ij}}\}_{1\le i\le n, 1\le j\le m_i}$, i.e., $W_{ij} = P_{ij}(\sum_{i,j} P_{ij}^T P_{ij})^{-1} P_{ij}^T$.

By setting the derivative of the Lagrangian function $\mathcal{L}(I, \chi, \rho)$ with respect

to I to be zero, we obtain the following condition on I.

$$\beta_1 \sum_{l=1}^{2} D_l^T (D_l I - g_l + \frac{b_l}{\beta_1}) + \beta_3 C^T (CI - R + \frac{e}{\beta_3}) + \beta_2 (I - \sum_{i,j} \frac{P_{ij}^T \Psi_{2D}^{-1} (\overline{Z}_i + \widehat{Z}_{ij} - \frac{f_{ij}^k}{\beta_2})}{\sum_{i,j} P_{ij}^T P_{ij}}) = 0. \quad (5.14)$$

$$\Gamma I = Y, \quad (5.15)$$

where,

$$\begin{aligned} \Gamma &= \beta_1 \sum_{l=1}^{2} D_l^T D_l + \beta_2 + \beta_3 C^T C \\ Y &= \beta_1 \sum_{l=1}^{2} D_l^T (g_l - \frac{b_l}{\beta_1}) + \beta_2 \sum_{i,j} \frac{P_{ij}^T \Psi_{2D}^{-1} (\overline{Z}_i + \widehat{Z}_{ij} - \frac{f_{ij}^k}{\beta_2})}{\sum_{i,j} P_{ij}^T P_{ij}} \\ &\quad + \beta_3 C^T (R - \frac{e}{\beta_3}). \end{aligned} \quad (5.16)$$

As mentioned previously, D_1 and D_2 are horizontal and vertical finite difference operators. Also, C is a circulant matrix with its first row as a random vector. Thus, the three multipliers on I, i.e., $D_1^T D_1, D_2^T D_2$ and $C^T C$, are circulant matrices and multiplying each of them with I is equivalent to some convolution on I. Thus, the image I^{k+1} can be efficiently recovered by using Fast Fourier Transformation (FFT).

5.4 Experimental Results

In this section, experimental results are presented to evaluate the performance of the proposed NLCS using both NLWS and NLJS, compared with the state-of-the-art 2DCS in image CS. For comprehensive comparison, we select eight test images, including four common test images (Barbara, Cameraman, Lena and House), two man-made structure images (Building and TrainStation) and two medical images (Bone and Brain), as shown in Figure 5.2. For computational efficiency, we employ circulant sampling on these images and obtain the sampled data $B = SCI$ at different sampling rates. NLCS using NLWS, NLCS using NLJS and the previous 2DCS are respec-

Figure 5.2: Test Images. From left to right, and from top to bottom: Barbara, Cameraman, Lena, House, Building, TrainStation, Bone and Brain. The size of most images is 256×256, except Building (480×480) and TrainStation(512×512),

tively applied to recover the images from their sampled data B. Peak signal-to-noise ratio (PSNR) is used to gauge the recovery accuracy.

In 2DCS (Eq. (5.1)), we empirically set the weight parameter for 2D wavelet sparsity as $\lambda = 0.66$, which is roughly the optimal value for all eight images. Then, our NLCS starts with the initialization image recovered by 2DCS at $\lambda = 0.66$ and iterates between non-local patch grouping and non-local joint recovery. In non-local grouping, we set the patch size $d = 8$, the step size $s = 4$ and the maximal group size $m = 8$. In non-local recovery, we empirically set the same parameters for both sparsity measures NLWS and NLJS: the NLS weight $\lambda = 2$ in Eq. (5.2), the over-regularization parameter $\beta_1 = \beta_2 = \beta_3 = 100$ in Eq. (5.8), and $\tau = 1.618$ in Algorithm 3. To recover the groups of highly correlated patches for NLJS, we set the weight on the sparsity of innovation components as $\eta = 10$ in Eq. (5.5).

5.4.1 Quantative Evaluation

In our NLCS algorithm, there is no theoretical guarantee that our algorithm can obtain global optimum by iterating between non-local grouping and non-local recovery. In Figure 5.3, we plot the curves of recovery accuracy of NLCS using NLWS and NLJS with respect to the number of iterations at sampling

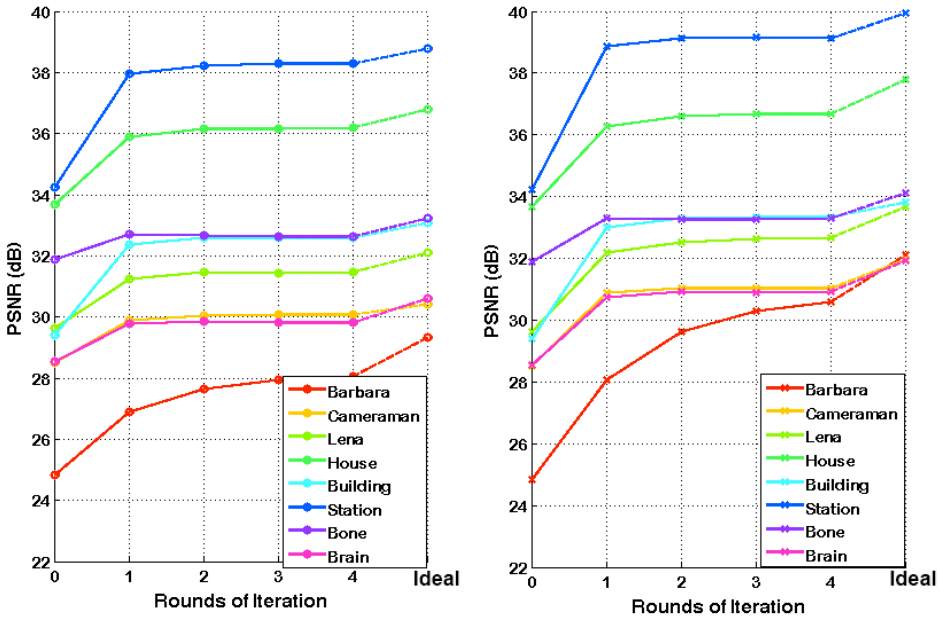

Figure 5.3: Convergence behavior of the proposed NLCS—the variation of recovery accuracy with the iteration number (up to 4). (a) NLCS using NLWS and (b) NLCS using NLJS. We use the dotted line to connect the NLCS recovery at iteration 4 to the ideal case where the grouping information is extracted from the original images.

rate of 20% for the eight test images. Note that the recovery results at iteration zero are those from 2DCS. As shown, NLCS consistently improves the the recovery accuracy and typically converges in about four iterations. To further evaluate the effectiveness of our NLCS, we also list the results of its ideal version where the grouping information is extracted exactly from the original image as references. After reaching its stable recovery accuracy, our NLCS using NLJS is only about 1 dB lower than the ideal cases, indicating that the NLCS is effective in recovering both the image and its non-local grouping information. On the images with many repeating structures (e.g., Barbara), NLCS has better performance and also takes more iterations to converge. On these eight images at sampling rate 10%, the final recovery accuracy of NLCS with NLWS is on average 2.56 dB higher than that of 2DCS, while the final accuracy of NLCS with NLJS is on average 3.80 dB higher than 2DCS. These significant improvement margins demonstrate the effectiveness of the non-local sparsity prior for image CS. Compared with NLWS, our NLJS is more effective as it models the patch group as a rank-1 subspace up to some sparse errors.

For complete comparison, NLCS with NLWS/NLJS and 2DCS are evaluated on the eight images at varying sampling rate ($10\%, 20\%$ and 30%), as shown in Table 5.1. NLCS using NLJS consistently outperforms NLCS using NLWS and both significantly improves over 2DCS at all sampling rates. As expected, NLCS using NLJS achieve larger improvements in terms of recovery accuracy on images that contain sharp edges (e.g., Building and TrainStation), and images with repeating structures (e.g. Barbara). On Barbara, the improvement is even as large as 6.81 dB over 2DCS at sampling rate 30%. On TrainStation, NLCS using NLJS can improve the recovery accuracy up to 36.07 dB at the low sampling rate of only 10%, suggesting that our new algorithm is much more practical compared with 2DCS.

5.4.2 Visual Quality Evaluation

To further compare our NLCS with 2DCS, we present their visual recovery results on some typical images. As shown in Figure 5.4 (note that images are better viewed in PDF), despite as the-state-of-the-art in image CS, 2DCS recovers the Barbara image with texture and edges (or boundaries) blurred.

Table 5.1: Evaluation of the proposed NLCS using NLWS, NLJS with 2DCS in terms of PNSR (dB) at varying sampling rate. We run NLCS using NLWS and NLJS in four rounds of iterations and compare them with 2DCS (the improvement over 2DCS is highlighted as "gain")and their ideal case where the grouping information is known. Note that images are numbered as follows: 1 Barbara, 2 Cameraman, 3 Lena, 4 House, 5 Building, 6 Train Station, 7 Bone and 8 Brain.

Image	Rate	2DCS	NLWS						NLJS					
			round1	round2	round3	round4	gain	ideal	round1	round2	round3	round4	gain	ideal
1	10 %	22.73	23.78	24.11	24.24	24.29	**1.56**	25.85	24.28	25.07	25.48	25.70	**2.97**	28.60
	20 %	24.85	26.91	27.65	27.94	28.06	**3.21**	29.34	28.07	29.63	30.31	30.60	**5.75**	32.12
	30 %	27.01	30.17	31.12	31.37	31.43	**4.42**	32.23	31.69	33.35	33.76	33.83	**6.81**	34.35
2	10 %	24.70	25.97	26.26	26.30	26.31	**1.61**	27.16	26.89	27.44	27.62	27.67	**2.97**	29.01
	20 %	28.52	29.89	30.05	30.08	30.10	**1.58**	30.42	30.88	31.04	31.04	31.02	**2.50**	31.98
	30 %	31.46	32.65	32.75	32.81	32.80	**1.34**	32.99	33.61	33.78	33.75	33.73	**2.27**	34.48
3	10 %	26.24	27.55	27.81	27.80	27.85	**1.61**	28.68	28.37	28.80	29.90	28.92	**2.68**	30.40
	20 %	29.63	31.23	31.46	31.45	31.48	**1.85**	32.12	32.17	32.54	32.64	32.67	**3.03**	33.67
	30 %	32.42	34.23	34.38	34.40	34.38	**1.96**	34.85	35.09	35.37	35.40	35.41	**2.99**	36.12
4	10 %	30.39	32.84	33.19	33.30	33.31	**2.92**	34.08	33.74	34.24	34.33	34.37	**3.98**	35.20
	20 %	33.69	35.91	36.14	36.17	36.19	**2.50**	36.78	36.28	36.59	36.66	36.69	**3.00**	37.80
	30 %	35.81	37.88	38.18	38.24	38.26	**2.45**	38.82	38.18	38.64	38.83	38.92	**3.11**	39.86
5	10 %	24.78	28.19	28.95	28.97	28.96	**4.18**	29.88	28.89	29.79	29.95	30.00	**5.22**	31.27
	20 %	29.39	32.37	32.59	32.61	32.60	**3.21**	33.08	33.00	33.31	33.35	33.35	**3.96**	33.83
	30 %	32.59	35.11	31.25	35.27	35.28	**2.69**	35.56	35.69	35.95	35.98	36.01	**3.42**	36.65
6	10 %	29.33	33.51	34.20	34.34	34.35	**5.02**	35.27	34.97	35.91	36.07	36.07	**6.74**	36.86
	20 %	34.24	37.96	38.23	38.30	38.31	**4.07**	38.77	38.86	39.14	39.15	39.14	**4.90**	39.94
	30 %	37.36	40.40	40.49	40.50	40.50	**3.14**	40.92	41.03	41.17	41.19	41.19	**3.83**	41.80
7	10 %	27.37	29.07	29.26	29.27	29.25	**1.88**	30.19	30.00	30.24	30.24	30.26	**2.89**	31.58
	20 %	31.88	32.71	32.68	32.65	32.63	**0.75**	33.24	33.31	33.27	33.28	33.30	**1.42**	34.10
	30 %	34.61	35.11	35.10	35.06	35.06	**0.45**	35.43	35.58	35.57	35.59	35.59	**0.98**	36.02
8	10 %	24.14	25.51	25.77	25.82	25.82	**1.68**	26.97	26.61	27.02	27.07	27.08	**2.94**	28.93
	20 %	28.54	29.77	29.84	29.83	29.83	**1.29**	30.60	30.75	30.91	30.90	30.91	**2.37**	31.94
	30 %	31.87	32.63	32.65	32.64	32.60	**0.73**	33.06	33.32	33.36	33.37	33.37	**1.50**	34.05

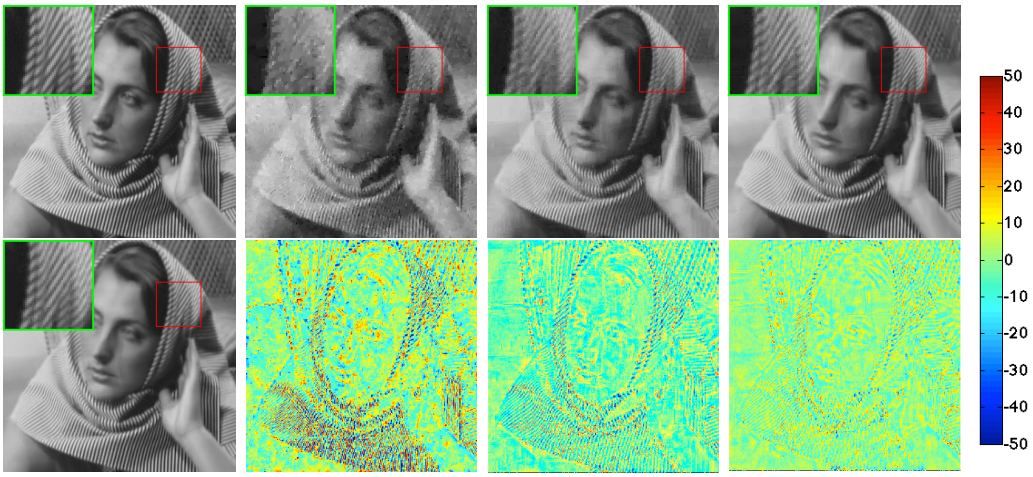

(a) (b) (c) (d)

Figure 5.4: Visual recovery of the proposed NLCS using NLWS and NLJS, in comparision with 2DCS on Barbara at 20% sampling rate. Top: (a) original image, recovered images by (b) 2DCS (PSNR: 24.85 dB), (c) NLWS (PSNR: 28.06 dB), and (d) NLJS (PSNR: 30.60 dB). Bottom: (a) image recovered by the ideal version of NLJS (PSNR: 32.12 dB), the error maps (with the color map on the left) of (b) 2DCS, (c) NLWS and (d) NLJS. **Note**: regions in green are zoomed-in versions of regions in red, and images are better viewed in PDF.

By adding the regularization on the non-local patch correlation, both NLCS using NLJS and NLWS can recover the Barbara image with correct texture and sharp edges. In the zoomed-in regions, we can see NLJS is superior to NLWS in recovering local details. The error maps of visual recovery also show that NLJS is better than NLWS and both significantly outperform 2DCS. In addition to the Barbara image that is full of repeating structures, we also show the visual recovery results on the man-made structure image TrainStation, the classical Cameraman image and the medical image Brain in Figure 5.5. On all these images, 2DCS always fails to recover details well, while the results from our NLCS hold much better fidelity to the ground truth and NLJS is always superior to NLWS as the non-local sparsity prior (note that images are better viewed in zoomed PDF).

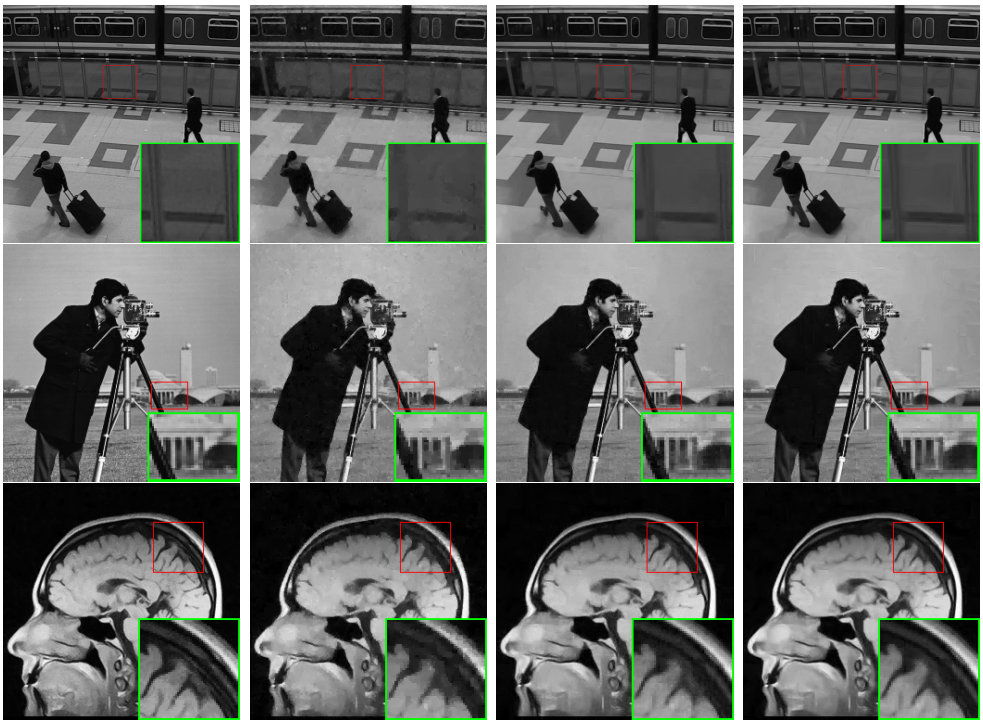

(a) (b) (c) (d)

Figure 5.5: Visual recovery of NLCS using NLWS and NLJS, in comparison with 2DCS on TrainStation (sampling rate: 10%), Cameraman (sampling rate: 20%) and Brain (sampling rate: 20%). (a) Original images, and images recovered by (b) 2DCS, (c) NLWS, and (d) NLJS. **Note**: regions in green are zoomed-in versions of regions in red, and images are better viewed in zoomed PDF.

5.5 Summary

In this chapter, we have proposed a non-local compressive sampling (NLCS) recovery method that exploits the non-local patch correlation and the local piecewise smoothness. To seek the patch correlation, we propose two non-local sparsity measures—non-local wavelet sparsity (NLWS) and non-local joint sparsity (NLJS). An efficient algorithm consisting of two iterative steps, non-local grouping and non-local recovery, is developed to solve the NLCS recovery problem. Extensive experiments show that our proposed NLJS can significantly improve the state-of-the-art image compressive sampling method, and NLJS is consistently better than NLWS as the non-local sparsity prior in recovering sharp edges and fine texture.

CHAPTER 6

CONCLUSIONS

In this dissertation, we studied advanced imaging via multiplexed sensing and compressive sensing, by exploring three unconventional object-to-image mapping models, such as one-to-multiple (OTM) divergent mapping, multiple-to-one (MTO) convergent mapping and multiple-to-multiple (MTM) random mapping. Multiplexed sensing and compressive sensing improve the conventional one-to-one (OTO) cameras from two opposite directions. The former attempts to acquire more information from the outside scene by OTM sampling, which trades the sensor resolution for multi-modality acquisition, while the latter aims at reducing the required sampling rate by MTO low-resolution sampling and MTM random sampling. The specific challenges and the progress we made in these two novel imaging systems is summarized as follows.

Multiplexed Sensing. Multiplexed imaging often involves manipulating the incoming light beam on the aperture, which is quite challenging, due to the fact that the aperture is located inside the lens housing. First, we proposed a multiplexed imaging system that allows accessing and dynamically manipulating the lens aperture for many computational imaging applications. Specifically, a rear-attached relay system (lens) is mounted behind the imaging lens to reposition the aperture plane outside the imaging lens, where it is quite easy to control the transmission, position and orientation of the aperture. We physically implemented this multiplexed imaging system and showed its advantageous applications in HDR imaging and multi-focus imaging. Admittedly, CIS_RJRS requires a high-quality large-aperture joint relay lens, which can be coupled with ordinary imaging lenses. However, this kind of relay lens is much easier to design than a high-quality imaging lens with external aperture. In the future, we will apply our multiplexed imaging system for a wider range of multiplexed imaging applications, such as panoramic imaging, coded aperture imaging and light field photography.

Compressive Sensing. Second, we proposed a hybrid compressive sensing (HCS) camera for image acquisition. Motivated by the fact that natural images are dominated by the low-frequency components, this hybrid compressive sensing camera further reduces the required sampling rate by combining the traditoinal MTM random sampling with the MTO low-resolution sampling. In addiion, we proposed a new total-variation measure TVL1 for sparse decoding, which enforces the sparsity and the directional continuity in the partial gradient domain. Theoretical and experimental results show that this new TVL1 requires lower sampling rate than the previous TV measure TVL1L2 in compressive sensing. Recently, we have seen that TVL1 is widely used in compressive sensing.

Third, we proposed a three-dimensional compressive sensing (3DCS) camera, which can reduce the required the sampling rate for video acquisition to a practical level (i.e., 10%). The core idea of 3DCS is a three-dimensional sparsity measure (3DSM) with its efficient algorithm, which decodes a video from incomplete random samples by exploiting its 3D piecewise smoothness and temporal low-rank property. Another idea in 3DCS is a video circulant sampling method, which further reduces the sampling rate and is easy to implement. Finally, a promising design of the 3DCS camera using video circulant sampling is presented and a new random lens is presented to simplify the traditional implementation of random convolution i.e., 4D correlator in Fourier optics. This random lens has much higher light-gathering power and higher imaging quality than other simple implementations, such as coded aperture, random pinhole array and random mirror array. In the future, we will try to build a 3DCS camera for the real computational imaging application.

Fourth, we proposed an efficient low-rank recovery approach, called robust orthonormal subspace learning (ROSL), which can be used to impose the low-rank prior knowledge in compressive sensing and other RPCA applications. Compared with RPCA using nuclear norm, ROSL presents a novel rank measure that imposes the group sparsity under orthonormal subspace, which enables to recover a low-rank matrix by fast sparse coding. This rank measure is proven to be lower-bounded by the nuclear norm and thus ROSL has the same global optima as RPCA. In addition, an efficient algorithm (alternating direction method+block coordinate descent) is developed to solve ROSL at the quadratic complexity and a random sampling technique is introduced

to further accelerate ROSL to the linear complexity. Extensive evaluations demonstrate that ROSL and ROSL+ achieve the state-of-the-art efficiency in low-rank recovery without compromising the accuracy.

Fifth, we proposed a non-local compressive sensing (NLCS) camera, which make is possible to recover an image at the sampling rate as low as 10%. Motivated by the non-local mean approaches in image restoration, a non-local compressive sensing (NLCS) recovery method is proposed, which further reduces the sampling rate by exploiting the non-local patch correlation and the local piecewise smoothness in natural images. Two non-local sparsity measures, i.e., nonlocal wavelet sparsity (NLWS) and non-local joint sparsity (NLJS), are proposed to obtain patch correlation in NLCS. In addition, an efficient iterative algorithm is developed to solve the NLCS recovery problem, which is shown to have stable convergence behavior in experiments. The experimental results show that our NLCS significantly improves the state of the art in image CS and that non-local joint sparsity is better than non-local wavelet sparsity in terms of recovery accuracy. It is worth exploring the application of NLJS in image restoration and its improvement over BM3D using NLWS.

APPENDIX A

DETAILED PROOF OF PROPOSITION 3 IN CHAPTER 4

In this appendix, we prove Proposition 3 in Chapter 4 from two different angles of view—large matrix approximation [97, 98] and compressive sensing [26]. Although the first proof follows the same way as that of Lemma 6 in [80], we want to present it here, since Proposition 3 gives a slightly more general bound (requiring smaller sampling number) on sampling density than Lemma 6 in [80]. By presenting it with the second proof using the fundamental theory in compressive sensing, we can also show the connection between large matrix approximation and compressive sensing. In addition, we present a simple and interesting verification of Proposition 3 in a special case.

In order to prove Proposition 3, we need to prove its simpler version—Lemma 3, which gives the required sample number such that the column sub-matrix has the same rank as the full matrix.

Lemma 3 (A simpler version of Proposition 3) *Let $A \in \mathbb{R}^{m\times n}$ be a rank-r matrix ($r \ll \min\{m,n\}$), whose SVD is denoted as $A = USV^T$, and A_l be a sub-matrix, generated by uniformly sampling l columns from A without replacement. Given a failure probability δ, if the sampling number $l \geq cr\mu(V)\log(r\mu(V)/\delta)/\epsilon^2$, then, the following relationship,*

$$\operatorname{rank}(A_l) = \operatorname{rank}(A) = r, \tag{A.1}$$

holds with probability at least $1-\delta$, where c is the oversampling parameter and $\epsilon \in (0,1]$ is the error tolerance.

Let $A_{(h)}$ be a sub-matrix generated by uniformly sampling h rows from A. Suppose Lemma 3 holds, we can easily induce that $\operatorname{rank}(A_{(h)}) = \operatorname{rank}(A) = r$ holds with probability at least $1-\delta$, if $h \geq cr\mu(U)\log(r\mu(U)/\delta)/\epsilon^2$. If $\operatorname{rank}(A_l) = \operatorname{rank}(A_{(h)}) = \operatorname{rank}(A) = r$, the intersection of A_l and $A_{(h)}$,

i.e., A_{LU}, should have the same rank as A. Thus, Proposition 3 follows immediately Lemma 3.

Since uniform sampling without replacement has higher probability to obtain A_l such that its rank is the same as A, than that with replacement. Thus, if the latter is proven to satisfy Lemma 3, the former should also satisfy Lemma 3. Thus, for simplicity of analysis, we will use uniform sampling with replacement in the following proof for Lemma 3.

A.1 One Proof of Lemma 3

For simplicity of notation, we design a binary matrix $\Upsilon \in \mathbb{R}^{n\times l}$ to denote the uniform sampling. For each column $j = \{1, ..., l\}$, Υ has only one non-zero entry, which can appear at any row with equal probability, i.e., for $i = \{1, ..., n\}$, $\Upsilon_{i,j} = 1$ with probability $P_i = \frac{1}{n}$. Thus, the column submatrix A_l can be denoted as $A_l = A\Upsilon$.

Suppose $A = USV^T$ by truncated SVD, where $S \in \mathbb{R}^{r\times r}$, the randomly sampled submatrix $A_l = USV_l^T$, where $V_l^T = V^T\Upsilon$ corresponds to a submatrix of V^T. Since $\text{rank}(A) = \text{rank}(V) = r$ and $\text{rank}(A_l) = \text{rank}(V_l)$, the relationship $\text{rank}(A_l) = \text{rank}(A)$ in Lemma 3 holds, if we can prove $\text{rank}(V_l) = \text{rank}(V) = r$.

Lemma 4 (Section 3.4.3 of [97]) *Given $B = [B_1|...|B_n] \in \mathbb{R}^{k\times n}$ and $C = [C_1|...|C_n] \in \mathbb{R}^{k\times n}$ be two rank-r matrices ($r \le k \le n$), define a column sampling probabilities P_i ($1 \le i \le n$) satisfying*

$$P_i \ge \frac{\beta}{Z}\|B_i\|_2\|C_i\|_2, \quad \textit{and} \quad \sum_{i=1}^{n} P_i = 1, \tag{A.2}$$

where $Z = \sum_{i=1}^{n} \|B_i\|_2\|C_i\|_2$ and $\beta \in (0, 1]$ is a scale parameter. Then, let generate a sub-matrix $\hat{B} = [B_{i_1}|...|B_{i_l}]$ from B in l column-sampling trials, in which B_{i_j} ($i_j \in \{1, ..., n\}$) is chose as the j^{th} column of $\hat{B}$ with the probability of P_{i_j}. Following the same l trials, $\hat{C} = [C_{i_1}|...|C_{i_l}]$ is generated from C.

Thus, BC^T can be approximated by

$$\frac{1}{l}\sum_{j=1}^{l}\frac{B_{i_j}C_{i_j}^T}{P_{i_j}}. \tag{A.3}$$

Let define a diagonal matrix $\Lambda \in \mathbb{R}^{l\times l}$ as $\Lambda = \mathrm{diag}(\frac{1}{\sqrt{lP_{i_j}}})_{1\le j\le l}$. For any $\epsilon \in (0,1]$ and $\delta \in (0,1]$, if the sample number $l \ge cr\log(\frac{r}{\beta\delta})/(\epsilon^2\beta)$, the following holds with probability at least $1-\delta$

$$\|BC^T - \hat{B}\Lambda\Lambda\hat{C}^T\|_2 \le \frac{\epsilon}{2}\|B\|_2\|C\|_2. \tag{A.4}$$

By adapting Lemma 4 to the special case where $B = C = V^T$ and their uniformly sampled sub-matrices $\hat{B} = \hat{C} = V_l^T = V^T\Upsilon$, we will induce the required sample number l such that $\mathrm{rank}(V_l) = \mathrm{rank}(V) = r$. as stated in Lemma 5.

Lemma 5 *Suppose error tolerance $\epsilon \in (0,1]$ and failure probability $\delta \in (0,1]$, the sub-matrix V_l is generated by uniformly sampling l columns of V_l^T, denoted as $V_l^T = V^T\Upsilon$. If $l \ge cr\mu(V)\log(\frac{r\mu(V)}{\delta})/\epsilon^2$, the following relations hold with probability at least $1-\delta$*

$$\|V^TV - V_l^T\Lambda\Lambda V_l\|_2 \le \frac{\epsilon}{2}\|V^T\|_2^2 \tag{A.5}$$

$$\mathrm{rank}(V_l) = \mathrm{rank}(V) = r. \tag{A.6}$$

Proof of Lemma 5. According to Lemma, we set B and C as $B = C = V^T \in \mathbb{R}^{r\times n}$ and thus their column sub-matrices $\hat{B} = \hat{C} = V_l^T$, where $V^TV = I$ and $V_l^T = V^T\Upsilon$. Due to the uniform sampling Υ, the sampling probability $P_i = \frac{1}{n}$, which satisfies

$$P_i = \frac{1}{n} \ge \frac{\beta}{Z}\|(V^T)_i\|_2^2, \tag{A.7}$$

where $(V^T)_i$ is the i^{th} column of V^T and $Z = \sum_{i=1}^{n}\|(V^T)_i\|_2^2$. Since $V^T \in \mathbb{R}^{r\times n}$ consists of orthonormal row vectors, we can get $Z = r$. Then, the constraint in Eq. (A.7) is equivalent to $\beta \le \frac{r}{n\max_{i=1}^{n}\|(V^T)_i\|_2^2}$. Let set β as its

largest possible value $\beta = \frac{r}{n \max_{i=1}^{n} \|(V^T)_i\|_2^2}$, which equals to $1/\mu(V)$. Thus, according to Lemma 4, if $l \geq cr\mu(V)\log(\frac{r\mu(V)}{\delta})/\epsilon^2$, $\|V^TV - V_l^T\Lambda\Lambda V_l\|_2 \leq \frac{\epsilon}{2}\|V^T\|_2^2$ will hold with probability at least $1-\delta$. At this case, for all $i \in \{1, ..., r\}$, the i^{th} singular value of V_l^T, denoted as $\sigma_i(V_l^T)$, should satisfy,

$$
\begin{aligned}
|1 - \sigma_i(V_l^T)| &= |\sigma_i(V^TV) - \sigma_i(V_l^T\Lambda\Lambda V_l)|, && \text{(A.8)}\\
&\leq \|V^TV - V_l^T\Lambda\Lambda V_l\|_2 && \text{(A.9)}\\
&\leq \frac{\epsilon}{2}\|V^T\|_2^2 && \text{(A.10)}\\
&= \frac{\epsilon}{2}. && \text{(A.11)}
\end{aligned}
$$

Since the error tolerance $\epsilon \in (0, 1]$, we can conclude that $\sigma_i(V_l^T) > 0$ for all $i \in \{1, ..., r\}$. Thus, $\text{rank}(V_l^T) = \text{rank}(V) = r$ follows $\|V^TV - V_l^T\Lambda\Lambda V_l\|_2 \leq \frac{\epsilon}{2}\|V^T\|_2^2$. For the details of the inequality in Eq. (A.9), we refer readers to the proof of Lemma 4 in [98].

From Lemma 5 to Lemma 3/Proposition 3. Since $A = USV^T$, $A_l = USV_l^T$ and $\text{rank}(A) = \text{rank}(V) = r$, we can induce that $\text{rank}(A_l) = \text{rank}(V_l) = r = \text{rank}(A)$ holds, if $\text{rank}(V_l^T) = \text{rank}(V) = r$. In other words, Lemma 3 and Proposition 3 follow immediately from Lemma 5, which is well proven above. Thus, Lemma 3 and Proposition 3 hold.

A.2 Another Proof of Lemma 3

Theorem 2 (Theorem 1.2 in [26]) *Let $V^T \in \mathbb{R}^{r\times n}$ be a rank-r matrix consisting of r orthonormal rows ($V^TV = I$), and $V_l^T \in \mathbb{R}^{r\times l}$ be a sub-matrix generated from V^T by uniform sampling. If the sample number $l \geq r\mu(V)\max(c_1\log(r), c_2\log(3/\delta))$, then, the following inequality*

$$\|I - \frac{n}{l}V_l^TV_l\|_2 < \frac{1}{2}, \tag{A.12}$$

holds with probability at least $1-\delta$, where c_1 and c_2 are positive constant, and $\mu(V)$ is the coherence of V^T (note: the coherence defined here is difference from that in [26]).

Lemma 6 (Extension of Theorem 1.2 in [26]) *Let $V^T \in \mathbb{R}^{r\times n}$ be a rank-*

r matrix consisting of r orthonormal rows ($V^TV = I$), and $V_l^T \in \mathbb{R}^{r\times l}$ be a sub-matrix generated from V^T by uniform sampling. If the sample number $l \geq cr\mu(V)\log(r/\delta)$, the following inequalities,

$$\|V^TV - V_l^T\Lambda\Lambda V_l\|_2 < \frac{1}{2}, \tag{A.13}$$

$$\text{rank}(V_l) = \text{rank}(V) = r, \tag{A.14}$$

hold with probability at least $1-\delta$, where c is an oversampling parameter and Λ is a diagonal matrix whose diagonal entries are identical, equal to $\sqrt{\frac{n}{l}}$.

Proof of Lemma 6. Due to uniform sampling, the probability of choosing any column from V^T is identical, i.e., $P_i = \frac{1}{n}$, $1 \leq i \leq n$. Thus, all the diagonal entries of the scale matrix Λ are equal to $\sqrt{\frac{1}{lP_i}} = \sqrt{\frac{n}{l}}$. Thus, $\|I - \frac{n}{l}V_l^TV_l\|_2 < \frac{1}{2}$ in Theorem 2 is equivalent to the first inequality $\|V^TV - V_l^T\Lambda\Lambda V_l\|_2 < \frac{1}{2}$.

Let us define a constant $c \geq \max(c_1, c_2)$, we can induce

$$\begin{aligned} r\mu(V)\max(c_1\log(r), c_2\log(3/\delta)) &\leq cr\mu(V)\max(\log(r), \log(3/\delta)) && \text{(A.15)}\\ &\leq cr\mu(V)(\log(r) + \log(3/\delta)) && \text{(A.16)}\\ &= cr\mu(V)\log(3r/\delta). && \text{(A.17)} \end{aligned}$$

Since the failure probability δ is a small value and the rank r is often much large than 3, $\log(3r/\delta) = \log(3) + \log(r/\delta)$ is very close to $\log(r/\delta)$. So, $r\mu(V)\log(3r/\delta)$ is on the same order of $r\mu(V)\log(r/\delta)$. By dropping the additive constant $\log(3)$, we can simplify the required sample number in Theorem 2 as $l \geq cr\mu(V)\log(r/\delta)$ in Lemma 6.

Thus, the first inequality $\|V^TV - V_l^T\Lambda\Lambda V_l\|_2 < \frac{1}{2}$ holds with probability at least $1-\delta$, if $l \geq cr\mu(V)\log(r/\delta)$. From the first inequality, we can easily induce $\text{rank}(V_l) = \text{rank}(V) = r$, similar to the proof of Lemma 5.

From Lemma 6 to Lemma 3/Proposition 3. Here, we can prove Lemma 3/Proposition 3 by using Lemma 6, rather than Lemma 5. By considering $\text{rank}(A) = \text{rank}(V) = r$ and $\text{rank}(A_l) = \text{rank}(V_l)$, we can conclude that $\text{rank}(A_l) = r = \text{rank}(A)$ and $\text{rank}(V_l) = \text{rank}(V)$ hold with probability at least $1-\delta$, if $l \geq cr\mu(V)\log(r/\delta)$ (Lemma 5). Since the coherence $\mu(V) \geq 1$ and error tolerance $\epsilon \in (0, 1]$, $l \geq cr\mu(V)\log(r/\delta)$ follows $l \geq cr\mu(V)\log(r\mu(V)/\delta)/\epsilon^2$ (the condition in Lemma 3). Thus, Lemma 3

and Proposition 3 holds.

A.3 A Special Case of Lemma 3

At the end, let us verify Proposition 3, or exactly Lemma 3, in a special case. Let us define a binary rank-r matrix $A \in \mathbb{R}^{r\times n}$, where n is a multiple of k, such that $\{A_{i,j}\}_{1\le i\le r, 1\le j\le n}$ satisfies

$$A_{i,j} = \begin{cases} \sqrt{\frac{r}{n}} & \text{if } (i-1)\frac{n}{r}+1 \le j \le i\frac{n}{r} \\ 0 & \text{otherwise} \end{cases} . \tag{A.18}$$

From this structured binary matrix A, we generate its column sub-matrix $A_l \in \mathbb{R}^{r\times l}$ $(l > r)$ by uniform sampling with replacement. In this special case, it is easy to calculate the failure probability δ of $\text{rank}(A_l) = \text{rank}(A)$ as $\delta < r(1-\frac{1}{r})^l$. Given $l > r \gg 1$, $(1-\frac{1}{r})^l$ can be approximated by $\frac{1}{\exp(l/r)}$. Accordingly, $l \ge r\log(r/\delta)$ when $l > r \gg 1$. In other words, $\text{rank}(A_l) = \text{rank}(A)$ holds with probability at least $1-\delta$, if the sample number satisfies $l \ge cr\log(r/\delta)$ and r is a large number, where $c > 1$ is an oversampling parameter. Suppose $A = USV^T$ by SVD, the coherence $\mu(V) = 1$. By setting the error tolerance $\epsilon = 1$, Lemma 3 is well verified in this special case.

REFERENCES

[1] P. Green, W. Sun, W. Matusik, and F. Durand, "Multi-aperture photography," *ACM Transactions on Graphics (TOG) - Proceedings of ACM SIGGRAPH*, vol. 26, no. 3, pp. 681–687, 2007.

[2] A. Veeraraghavan, R. Raskar, A. Agrawal, A. Mohan, and J. Tumblin, "Dappled photography: Mask enhanced cameras for heterodyned light fields and coded aperture refocusing," *ACM Transactions on Graphics (TOG) - Proceedings of ACM SIGGRAPH*, 2007.

[3] C.-K. Liang, T.-H. Lin, B.-Y. Wong, C. Liu, and H. Chen, "Programmable aperture photography: Multiplexed light field acquisition," *ACM Transactions on Graphics (TOG) - Proceedings of ACM SIGGRAPH*, vol. 27, no. 3, pp. 55:1–55:10, 2008.

[4] A. Levin, R. Fergus, F. Durand, and W. T. Freeman, "Image and depth from a conventional camera with a coded aperture," *ACM Transactions on Graphics (TOG) - Proceedings of ACM SIGGRAPH*, vol. 26, no. 3, 2007.

[5] R. P. Harvey, "Optical beam splitter and electronic high speed camera incorporating such a beam splitter," U. S. Patent 5,734,507, March, 1998.

[6] M. Aggarwal and N. Ahuja, "Split aperture imaging for high dynamic range," in *Proceedings of International Conference on Computer Vision (ICCV)*, vol. 2, 2001, pp. 10–17.

[7] E. H. Adelson and J. Y. A. Wang, "Single lens stereo with plenoptic camera," *IEEE Transactions on Pattern Analysis and Machine Intelligence (TPAMI)*, vol. 14, no. 2, pp. 99–106, 1992.

[8] T. Georgiev, K. C. Zheng, B. Curless, D. Salesin, S. Nayar, and C. Intwala, "Spatio-angular resolution tradeoffs in integral photography," pp. 263–272, 2006.

[9] R. Ng, M. Levoy, M. Bredif, G. Duval, M. Horowitz, and P. Hanrahan, "Light field photography with a hand-held plenoptic camera," Stanford University, Tech. Rep. CSTR 2005-02, 2005.

[10] C. Gao, N. Ahuaj, and H. Hua, "Active aperture control and sensor modulation for flexible imaging," in *Proceedings of IEEE Conference on Computer Vision and Pattern Recognition (CVPR)*, 2007, pp. 1–8.

[11] S. K. Nayar, "Catadioptric omnidirectional camera," in *Proceedings of IEEE Conference on Computer Vision and Pattern Recognition (CVPR)*, 1997, pp. 482–488.

[12] A. Zomet and S. Nayar, "Lensless imaging with a controllable aperture," in *Proceedings of IEEE Conference on Computer Vision and Pattern Recognition (CVPR)*, 2006, pp. 339–346.

[13] S. K. Nayar and T. Mitsunaga, "High dynamic range imaging: Spatially varying pixel exposures," in *Proceedings of IEEE Conference on Computer Vision and Pattern Recognition (CVPR)*, vol. 1, 2000, pp. 472–479.

[14] S. Nayar and V. Branzoi, "Adaptive dynamic range imaging: Optical control of pixel exposures over space and time," in *Proceedings of International Conference on Computer Vision (ICCV)*, vol. 2, 2003, pp. 1168–1175.

[15] S. Nayar, V. Branzoi, and T. Boult, "Programmable imaging using a digital micromirror array," in *Proceedings of IEEE Conference on Computer Vision and Pattern Recognition (CVPR)*, 2004, pp. 436–443.

[16] M. Aggarwal and N. Ahuja, "High dynamic range panoramic imaging," in *Proceedings of International Conference on Computer Vision (ICCV)*, vol. 1, 2001, pp. 2–9.

[17] W. J. Smith, *Modern Optical Engineering*, 3rd ed. McGraw-Hill, 2000.

[18] H. Mannami, R. Sagawa, Y. Mukaigawa, T. Echigo, and Y. Yagi, "High dynamic range camera using reflective liquid crystal," in *Proceedings of International Conference on Computer Vision (ICCV)*, vol. 14, no. 21, 2007, pp. 1–8.

[19] S. Hiura and T. Matsuyama, "Depth measurement by the multi-focus camera," in *Proceedings of IEEE Conference on Computer Vision and Pattern Recognition (CVPR)*, 1998, pp. 953–959.

[20] "Camera calibration toolbox for matlab," 2002, http://www.vision.caltech.edu/bouguetj/calib_doc.

[21] R. Fattal, D. Lischinski, and M. Werman, "Gradient domain high dynamic range compression," *ACM Transactions on Graphics (TOG) - Proceedings of ACM SIGGRAPH*, pp. 249–256, 2002.

[22] A. Skodras, C. Christopoulos, and T. Ebrahimi, "The jpeg2000 still image compression standard," *IEEE Signal Processing Magagine*, vol. 18, pp. 36–58, 2001.

[23] D. Donoho, "Compressed sensing," *IEEE Transaction on Information Theory*, vol. 52, no. 4, 2006.

[24] J. Romberg, "Variational methods for compressive sampling," in *Proceedings of SPIE*, vol. 6498, 2007, pp. 64 980J–2–5.

[25] J. Romberg, "Imaging via compressive sampling," *Communications on Pure and Applied Mathematics*, pp. 14–20, 2008.

[26] E. Candes and J. Romberg, "Sparsity and incoherence in compressive sampling," *Inverse Problems*, vol. 23, no. 3, pp. 969–986, 2007.

[27] D. Takhar, J. N. Laska, M. B. Wakin, M. F. Duarte, D. Baron, S. Sarvotham, K. F. Kelly, and R. G. Baraniuk, "A new compressive imaging camera architecture using optical-domain compression," in *Proceedings of Computational Imaging IV at SPIE Electronic Imaging*, vol. 6065, 2006, pp. 43–52.

[28] M. F. Duarte, M. A. Davenport, D. Takhar, J. N. Laska, T. Sun, K. F. Kelly, and R. G. Baraniuk, "Single-pixel imaging via compressive sampling," *IEEE Signal Processing Magazine*, vol. 25, no. 2, pp. 83–91, 2008.

[29] B. K. Natarajan, "Sparse approximate solutions to linear systems," *SIAM Journal on Computing*, vol. 24, pp. 227–234, 1995.

[30] E. Candes and T. Tao, "Near-optimal signal recovery from random projections and universal encoding strategies?" *IEEE Transactions on Information Theory*, vol. 52, no. 12, pp. 5406–5245, 2006.

[31] E. Candes and T. Tao, "Decoding by linear programming," *IEEE Transactions on Information Theory*, vol. 51, pp. 4203–4215, 2005.

[32] L. He, T.-C. Chang, S. Osher, T. Fang, and P. Speier, "MR image reconstruction by using the iterative refinement method and nonlinear inverse scale space methods," University of California, Los Angeles (UCLA), Tech. Rep. CAM 06-35, 2006.

[33] L. Rudin, S. Osher, and E. Fatemi, "Nonlinear total variation based noise removal algorithms," *Physica D Nonlinear Phenomena*, vol. 60, no. 1, pp. 259–268, 1992.

[34] S. Ma, W. Yin, Y. Zhang, and A. Chakraborty, "An efficient algorithm for compressed MR imaging using total variation and wavelets," in *Proceedings of IEEE Conference on Computer Vision and Pattern Recognition (CVPR)*, 2008.

[35] M. Lustig, D. Donoho, J. Santos, and J. Pauly, "Compressed sensing MRI," *IEEE Signal Processing Magazine*, 2007.

[36] J. Yang, Y. Zhang, and W. Yin, "A fast alternating direction method for TVL1-L2 signal reconstruction from partial Fourier data," *IEEE Journal of Selected Topics in Signal Processing*, 2008.

[37] R. Maleh, A. C. Gilbert, and M. J. Strauss, "Sparse gradient image reconstruction done faster," in *Proceedings of International Conference on Image Processing (ICIP)*, vol. 2, 2007, pp. 77–80.

[38] E. Candes, J. Romberg, and T. Tao, "Stable signal recovery from incomplete and inaccurate measurements," *Communications on Pure and Applied Mathematics*, vol. 59, no. 8, pp. 1208–1223, 2006.

[39] L. Gan, T. Do, and T. Tran, "Fast compressive imaging using scrambled block Hadamard ensemble," in *Proceedings of European Signal Processing Conference*, 2008.

[40] R. Coifman, F. Geshwind, and Y. Meyer, "Noiselets," *Applied and Computational Harmonic Analysis*, vol. 10, pp. 27–44, 2001.

[41] J. A. Tropp and A. C. Gilbert, "Signal recovery from partial information via orthogonal matching pursuit," *IEEE Transactions on Information Theory*, vol. 53, pp. 4655–4666, 2007.

[42] S. Chen and D. Donoho, "Atomic decomposition by basic pursuit," *SIAM Journal on Scientific Computing (SISC)*, vol. 20, pp. 33–61, 1998.

[43] "Sparselab," available at http://sparselab.stanford.edu.

[44] "L1-magic," available at http://www.acm.caltech.edu/l1magic.

[45] M. A. Saunders, "PDCO: Primal-dual interior-point method for convex objectives," available at http://www.stanford.edu/group/SOL/software/pdco.html, 2002.

[46] W. Yin, S. P. Morgan, J. Yang, and Y. Zhang, "Practical compressive sensing with Toeplitz and circulant matrices," Rice University, Tech. Rep. CAAM TR10-01, 2010.

[47] V. Stankovic, L. Stankovic, and S. Cheng, "Compressive video sampling," in *Proceedings of European Conference on Computer Vision (ECCV)*, 2008.

[48] J. Zheng and E. L. Jacobs, "Video compressive sensing using spatial domain sparsity," *SPIE Optical Engineering*, vol. 48, no. 8, 2009.

[49] L. Kang and C. Lu, "Distributed compressive video sensing," in *Proceedings of International Conference on Acoustics, Speech, and Signal Processing (ICASSP)*, 2009.

[50] M. Wakin, J. Laska, M. Duarte, D. Baron, S. Sarvotham, D. Takhar, K. Kelly, and R. Baraniuk, "Compressive imaging for video representation and coding," in *Proceedings of Picture Coding Symposium*, 2006.

[51] R. Marcia and R. Willett, "Compressive coded aperture video reconstruction," in *Proceedings of European Signal Processing Conference*, 2008.

[52] C. Eckart and G. Young, "The approximation of one matrix by another of lower rank," *Psychometrika*, vol. 1, no. 3, pp. 211–218, 1936.

[53] X. Shu and N. Ahuja, "Hybrid compressive sampling via a new total variation TVL1," in *Proceedings of European Conference on Computer Vision (ECCV)*, 2010.

[54] E. Candes, X. Li, Y. Ma, and J. Wright, "Robust principal component analysis?" *Journal of the ACM*, vol. 58, no. 3, article 11, 2011.

[55] A. L. Chistov and D. Y. Grigoriev, "Complexity of quantifier elimination in the theory of algebraically closed fields," *Mathematical Foundations of Computer Science*, vol. 176, pp. 17–31, 1984.

[56] E. Candes and B. Recht, "Exact matrix completion via convex optimization," *Foundations of Computational Mathematics*, vol. 9, no. 6, pp. 717–772, 2009.

[57] D. Baron, M. B. Wakin, M. F. Duarte, S. Sarvotham, and R. G. Baraniuk, "Distributed compressed sensing," *arXiv preprint arXiv:0901.3403*, 2009.

[58] J. Romberg, "Compressive sensing by random convolution," *SIAM Journal on Imaging Science*, vol. 2, no. 4, pp. 1098–1128, 2009.

[59] E. E. Fenimore and T. M. Cannon, "Coded aperture imaging with uniformly redundant arrays," *Applied Optics*, vol. 17, pp. 337–347, 1978.

[60] R. Fergus, A. Torralba, and W. T. Freeman, "Random lens imaging," Massachusetts Institute of Technology (MIT), Tech. Rep. CSAIL TR 2006-058, 2006.

[61] S. Boyd, N. Parikh, E. Chu, B. Peleato, and J. Eckstein, "Distributed optimization and statistical learning via the alternating direction method of multipliers," *Foundations and Trends in Machine Learning*, vol. 3, no. 1, p. 1122, 2011.

[62] R. Glowinski, *Numerical Methods for Nonlinear Variational Problems*. Springer-Verlag, 1984.

[63] J. Cai, E. Candes, and Z. Shen, "A singular value thresholding algorithm for matrix completion," *SIAM Journal on Optimization*, vol. 20, pp. 1956–1982, 2010.

[64] M. K. Ng, R. H. Chan, and W. C. Tang, "A fast algorithm for deblurring models with Neumann boundary conditions," *SIAM Journal on Scientific Computing*, vol. 21, no. 3, pp. 851–866, 2000.

[65] Y. Peng, A. Ganesh, J. Wright, and Y. Ma, "RASL: Robust alignment by sparse and low-rank decomposition for linearly correlated images," in *Proceedings of IEEE Conference on Computer Vision and Pattern Recognition (CVPR)*, 2010.

[66] L. Li, W. Huang, I. Gu, and Q. Tian, "Statistical modeling of complex backgrounds for foreground object detection," *SIAM Journal on Scientific Computing*, vol. 13, no. 11, 2004.

[67] X. Yuan and J. Yang, "Sparse and low-rank matrix decomposition via alternating direction methods," *preprint*, 2009.

[68] B. Recht, M. Fazel, and P. Parrilo, "Guaranteed minimum-rank solutions of linear matrix equations via nuclear norm minimization," *Arxiv preprint:0706.4138*, 2007.

[69] R. Tomioka, T. Suzuki, M. Sugiyama, and H. Kashima, "A fast augmented Lagrangian algorithm for learning low-rank matrices," in *Proceedings of International Conference on Machine Learning (ICML)*, 2010.

[70] Z. Lin, M. Chen, and Y. Ma, "The augmented lagrange multiplier method for exact recovery of corrupted low-rank matrices," University of Illinois at Urbana-Champaign (UIUC), Tech. Rep. UILU-ENG-09-2214, 2010.

[71] T. Zhou and D. Tao, "GoDec: Randomized low-rank and sparse matrix decomposition in noisy case," in *Proceedings of International Conference on Machine Learning (ICML)*, 2011.

[72] Y. Mu, J. Dong, X. Yuan, and S. Yan, "Accelerated low-rank visual recovery by random projection," in *Proceedings of IEEE International Conference on Computer Vision and Pattern Recognition (CVPR)*, 2011.

[73] Q. Ke and T. Kanade, "Robust L1 norm factorization in the presence of outliers and missing data by alternative convex programming," in *Proceedings of IEEE International Conference on Computer Vision and Pattern Recognition (CVPR)*, vol. 1, 2005, pp. 739–746.

[74] Y. Shen, Z. Wen, and Y. Zhang, "Augmented Lagrangian alternating direction method for matrix separation based on low-rank factorization," Rice University, Tech. Rep. CAAM TR11-02, 2011.

[75] B. Turlach, W. Venables, and S. Wright, "Simultaneous variable selction," *Technometrics*, vol. 47, pp. 349–363, 2005.

[76] M. Yuan and Y. Lin, "Model selection and estimation in regression with grouped variables," *Journal of the Royal Statistical Society: Series B*, vol. 68, pp. 49–67, 2006.

[77] J. Mairal, F. Bach, J. Ponce, G. Sapiro, and A. Zisserman, "Non-local sparse models for image restoration," in *Proceedings of International Conference on Computer Vision (ICCV)*, 2009.

[78] S. Bengio, F. Pereira, Y. Singer, and D. Strelow, "Group sparse coding," in *Proceedings of Advances in Neural Information Processing Systems (NIPS)*, vol. 22, 2009, pp. 82–89.

[79] J. Huang, T. Zhang, and D. Metaxas, "Learning with structured sparsity," in *Proceedings of International Conference on Machine Learning (ICML)*, 2009.

[80] L. Mackey, A. Talwakar, and M. Jordan, "Divide-and-conquer matrix factorization," in *Proceedings of Advances in Neural Information Processing Systems (NIPS)*, 2011.

[81] C. Williams and M. Seeger, "Using the Nystrom method to speed up the kernel machines," in *Proceedings of Advances in Neural Information Processing Systems (NIPS)*, 2000.

[82] S. Kumar, M. Mohri, and A. Talwalkar, "On sampling-based approximate spectral decomposition," in *Proceedings of International Conference on Machine Learning (ICML)*, 2009.

[83] A. Talwalkar and A. Rostamizadeh, "Matrix coherence and the Nystrom method," in *Proceedings of the Twenty-Sixth Conference Annual Conference on Uncertainty in Artificial Intelligence (UAI-10)*, 2010.

[84] M. Fazel, H. Hindi, and S. Boyd, "A rank minimization heuristic with application to minimum order system approximation," in *Proceedings of American Control Conference*, vol. 42, no. 165, 2001, pp. 115–142.

[85] N. Srebro, J. Rennie, and T. Jaakkola, "Maximum-margin matrix factorization," in *Proceedings of Advances in Neural Information Processing Systems (NIPS)*, vol. 17, 2005, pp. 1329–1336.

[86] D. Bertsekas, Ed., *Constrained Optimization and Lagrange Multiplier Method*. Academic Press, 1982.

[87] M. Aharon, M. Elad, and A. Bruckstein, "K-SVD: An algorithm for designing overcomplete dictionaries for sparse representation," *IEEE Transactions on Signal Processing*, vol. 54, no. 11, pp. 4311–4322, 2006.

[88] K. Gregor and Y. LeCun, "Learning fast approximations of sparse coding," in *Proceedings of International Conference on Machine Learning (ICML)*, 2010.

[89] B. Recht, "A simpler approach to matrix completion," 2009, arXiv:0910.0651v2[CS.IT].

[90] E. Candes, "An introduction to compressive sampling," *IEEE Signal Processing Magazine*, pp. 221–230, 2008.

[91] L. Rudin and S. Osher, "Total variation based image restoration with free local constraints," in *Proceedings of International Conference on Image Processing (ICIP)*, 1994.

[92] X. Shu and N. Ahuja, "Imaging via three-dimensional compressive sampling (3dcs)," in *Proceedings of International Conference on Computer Vision (ICCV)*, 2011.

[93] A. Buades, B. Coll, and J. M. Morel, "A non-local algorithm for image denoising," in *Proceedings of IEEE Conference on Computer Vision and Pattern Recognition (CVPR)*, vol. 2, 2005, pp. 60–65.

[94] K. Dabov, A. Foi, V. Katkovnik, and K. Egiazarian, "Image denoising by sparse 3D transform-domain collaborative filtering," *IEEE Transaction on Image Processing*, vol. 16, no. 8, pp. 2080–2095, 2007.

[95] M. Wakin, J. Laska, M. Duarte, D. B. S. Sarvotham, D. Takhar, K. F. Kelly, and R. G. Baraniuk, "An architecture for compressive imaging," in *Proceedings of International Conference on Image Processing (ICIP)*, 2006, pp. 1273–1276.

[96] J. Yang and Y. Zhang, "Alternating direction algorithms for l1-problems in compressive sensing," Rice University, Tech. Rep. CAAM TR09-37, 2009.

[97] D. Hsu, S. M. Kakade, and T. Zhang, "Dimension-free tail inequalities for sums of random matrices," 2011, arXiv:1104.1672v3[math.PR].

[98] P. Drineas, M. Mahoney, and S. Muthukrishnan, "Relative-error CUR matrix decomposition," *SIAM Journal on Matrix Analysis and Applications*, vol. 30, pp. 844–881, 2008.